ABSTRACT

Title of Dissertation: AN EVALUATION OF METHODS FOR MEASURING PHYTOPLANKTON AND ECOSYSTEM STATUS IN THE CHUKCHI SEA

Aimee Renee Neeley, Doctor of Philosophy, 2020

Dissertation directed by: Dr. Lora A. Harris, Department of Marine Estuarine Environmental Science

This dissertation represents a three-pronged approach for evaluating ecosystem-level changes in the Chukchi Sea: 1) evaluation of uncertainties in field measurements of absorption 2) direct measurements of phytoplankton taxonomy and the community's interaction with the environment and 3) apply existing and new remote sensing tools to measure ecosystem-level changes over large spatio-temporal scales. The first and final chapters provide context for the dissertation and conclusions. The second chapter quantifies the magnitude of uncertainty within multiple methods for measuring particle absorption. The light field exiting the surface ocean is measured by satellite instruments as ocean color and is impacted by water column absorption. Biogeochemically-relevant products, such as phytoplankton and particle absorption are derived from the light field using algorithms. Therefore, accurate measurements of absorption are critical to algorithm development and validation. I employed a multi-method approach to estimate the precision of measuring optical density of particles on a filter pad using two common spectrophotometric methods, and assessed the uncertainty of the computational techniques for estimating a_p. The uncertainty ranged from 7.48%-119%. Values of a_p at 555 nm and 670 nm exhibited the highest values of uncertainty. Poor performance of modeled a_p compared to measured a_p suggests the uncertainties are propagated into bio-optical algorithms.

The third chapter investigates the consequences of earlier seasonal sea ice retreat and a longer sea-ice-free season on phytoplankton community composition. The timing of sea ice retreat, light availability and sea surface stratification largely control the phytoplankton community composition in the Chukchi Sea. This region is

experiencing a significant warming trend, decrease in sea ice cover, and a documented decline in annual sea ice persistence and thickness over the past several decades. I applied multivariate statistical techniques to elucidate the mechanisms that relate environmental variables to phytoplankton community composition in the Chukchi Sea using data collected during a single field campaign in the summer of 2011. Three phytoplankton groups emerged that were correlated with sea ice, sea surface temperature, nutrients, salinity and light.

The fourth chapter evaluates a new remote sensing tool for its utility to trace trends in ocean color over the summer months, 2003-2018, in the Chukchi Sea. The apparent visible wavelength reduces an ocean color spectrum to one number that represents the apparent color of the water. Median trend analysis of apparent visible wavelength and Chlorophyll *a* indicated that an ecosystem-level change in phytoplankton and nonalgal particles has occurred, correlated with the loss of sea ice.

AN EVALUATION OF METHODS FOR MEASURING PHYTOPLANKTON AND THE ECOSYSTEM STATUS IN THE CHUKCHI SEA

by

Aimee Renee Neeley

Dissertation submitted to the Faculty of the Graduate School of the
University of Maryland, College Park, in partial fulfillment
of the requirements for the degree of
Doctor of Philosophy
2020

Advisory Committee:
Dr. Lora A. Harris, Chair
Dr. Raleigh Hood
Dr. Michael Wilberg
Dr. Jacqueline Grebmeier
Dr. Karen Frey

Preface

The following dissertation represents my passion for the Arctic. I first visited the Arctic on the Sir Wilfred Laurier, traveling from Dutch Harbor Alaska to Barrow, Alaska in 2002. I had never been on a ship before and let's just say I was quite spoiled. However, I was seasick for the first day or so on the calmest water you can imagine, which, in looking back, is slightly embarrassing. But this trip really inspired my passion for field work and the Arctic. In my years during and after my master's program, I have visited the Arctic one other time and the Antarctic three times, some of the most beautiful places I have ever seen. As such, I dedicated my PhD to studying the Arctic.

In this dissertation I evaluate the utility of remote sensing and statistical tools to measure phytoplankton community structure and ecosystem status in the Chukchi Sea. With the continued warming and loss of sea ice in the Arctic we expect to observe, and are observing, shifts in ecosystem dynamics. Animals are moving from one part of the Chukchi Sea or Bearing Sea to another to find more favorable conditions or to find another source of food. Phytoplankton blooms are occurring earlier in the season and the observation of a secondary fall bloom all indicate that the 'status quo' of the Arctic seasonal pattern may no longer exist. Therefore, we must utilize all available tools, especially remote sensing, to understand the changes and their future repercussions, which we demonstrate in this dissertation.

Foreword

Contained within this dissertation are three research chapters. Chapter 1 provides introductory material to set the stage for Chapters 2-4. I have published Chapters 2 and 3 in peer-reviewed journals as first author with one or two of my committee members as co-authors. Chapter 4 represents a collaboration with a committee member and a colleague that will be submitted for publication after completion and defense of this dissertation. Chapter 5 represents concluding comments on the entirety of this dissertation. Citations for the two published papers are listed below.

Neeley, A. R., Freeman, S. A., & Harris, L. A. (2015). Multi-method approach to quantify uncertainties in the measurements of light absorption by particles. *Optics Express*, *23*(24), 31043-31058.

Neeley, A. R., Harris, L. A., & Frey, K. E. (2018). Unraveling Phytoplankton Community Dynamics in the Northern Chukchi Sea Under Sea□Ice□Covered and Sea□Ice□Free Conditions. *Geophysical Research Letters*, *45*(15), 7663-7671.

Dedication

This dissertation is dedicated to my grandmother, Chloann Dufford, who unfortunately passed away in October 2018 and didn't get to see me complete this big step of my life. She was my biggest cheerleader, and I always made sure she was proud of me. She would share my travels with her friends at church and everyone knew me as the oceanographer at NASA, even though they didn't know me personally. I don't believe I would be here today without her prayers.

Acknowledgements

I would like to acknowledge my advisor and committee members for all of their support through this process. I would like to also thank Dr. Karen Frey for her sea ice expertise that was valuable for Chapters 3 and 4. This work was supported by funding from the Ocean Biology and Biogeochemistry program of the National Aeronautics and Space Administration (NNG11HP11C). Appreciation is extended to all of the participants in the 2014 Absorption Workshop for their expertise and advice, in particular Collin Roesler, Rick Reynolds and Eurico D'Sa for their feedback on Chapter 2. I also acknowledge NASA support for the GSFC OBB Field Support Group who participated in the ICESCAPE campaigns. I extend appreciation to the scientists and crew of the U.S. Coast Guard Cutter Healy and to chief scientist Kevin Arrigo from Stanford University. I also extend my gratitude to Ivona Cetinić (NASA, USRA), Carlos Del Castillo (NASA), Jeremy Werdell and Ryan Vandermeulen for advice and input for Chapters 2-4. We acknowledge Sam Laney from WHOI who provided the phytoplankton taxonomic data, the Scripps Institute of Oceanography (SIO) ODF group for collecting and processing CTD and nutrient data, Dr. Rick Reynolds from SIO who provided the filter pad absorption data, Dr. Atsushi Matsuoka who provided the aCDOM data and Dr. Greg Mitchell from SIO who provided radiometry data. I also extend a big thank you to my management at NASA who was very patient and supportive of me throughout this process.

Table of Contents

List of Tables

List of Figures

$R_{rs}(412)$ and $R_{rs}(443)$ and a significant increase in $R_{rs}(555)$ and $R_{rs}(667)$ over the 16-year study period. f) Location 7 monthly Chl*a* in units of mg/m^3 for June-September, 2003-2018.

Figure A2.7. Integral-normalized $R_{rs}(\lambda)$ in plots in units of nm^{-1} for Location 9 in a) June b) July c) August and d) September. Line colors represent year of observation. e) Regression analysis plot of select $R_{rs}(\lambda)$ channels showing a significant decrease in $R_{rs}(412)$ and $R_{rs}(443)$ and a significant increase in $R_{rs}(555)$ and $R_{rs}(667)$ over the 16-year study period. f) Location 9 monthly Chl*a* in units of mg/m^3 for June-September, 2003-2018.

Figure A2.8. Integral-normalized $R_{rs}(\lambda)$ in plots in units of nm^{-1} for Location 10 in a) June b) July c) August and d) September. Line colors represent year of observation. e) Regression analysis plot of select $R_{rs}(\lambda)$ channels showing a significant decrease in $R_{rs}(412)$ and $R_{rs}(443)$ and a significant increase in $R_{rs}(555)$ and $R_{rs}(667)$ over the 16-year study period. f) Location 10 monthly Chl*a* in units of mg/m^3 for June-September, 2003-2018.

Figure A2.9. Integral-normalized $R_{rs}(\lambda)$ in plots in units of nm^{-1} for Location 11 in a) June b) July c) August and d) September. Line colors represent year of observation. e) Regression analysis plot of select $R_{rs}(\lambda)$ channels showing a significant decrease in $R_{rs}(412)$ and $R_{rs}(443)$ and a significant increase in $R_{rs}(555)$ and $R_{rs}(667)$ over the 16-year study period. f) Location 11 monthly Chl*a* in units of mg/m^3 for June-September, 2003-2018.

Figure A2.10. Integral-normalized $R_{rs}(\lambda)$ in plots in units of nm^{-1} for Location 13 in a) June b) July c) August and d) September. Line colors represent year of observation. e) Regression analysis plot of select $R_{rs}(\lambda)$ channels showing a significant decrease in $R_{rs}(412)$ and $R_{rs}(443)$ and a significant increase in $R_{rs}(555)$ and $R_{rs}(667)$ over the 16-year study period. f) Location 13 monthly Chl*a* in units of mg/m^3 for June-September, 2003-2018.

Figure A2.11. Integral-normalized $R_{rs}(\lambda)$ in plots in units of nm^{-1} for Location 14 in a) June b) July c) August and d) September. Line colors represent year of observation. e) Regression analysis plot of select $R_{rs}(\lambda)$ channels showing a significant decrease in $R_{rs}(412)$ and $R_{rs}(443)$ and a significant increase in $R_{rs}(555)$ and $R_{rs}(667)$ over the 16-year study period. f) Location 14 monthly Chl*a* in units of mg/m^3 for June-September, 2003-2018.

Figure A2.12. Integral-normalized $R_{rs}(\lambda)$ in plots in units of nm^{-1} for Location 15 in a) June b) July c) August and d) September. Line colors represent year of observation. e) Regression analysis plot of select $R_{rs}(\lambda)$ channels showing a significant decrease in $R_{rs}(412)$ and $R_{rs}(443)$ and a significant increase in $R_{rs}(555)$ and $R_{rs}(667)$ over the 16-year study period. f) Location 15 monthly Chl*a* in units of mg/m^3 for June-September, 2003-2018.

Chapter 1: Summary of the Chukchi Sea ecosystem and proposed measurements for monitoring climate change and ecosystem response

1.1 An introduction to the Chukchi Sea region

The Chukchi Sea is a shallow (~50 m) and dynamic sea that lies between the Pacific and Arctic Oceans (Figure 1.1). This region experiences extreme air temperature variations year-round, with sea ice cover and darkness dominating during the cold winter months (October - May). During the summer months (June - September), temperatures are warmer and sea ice retreats northward, exposing the surface waters to the atmosphere and warming by the sun. Since ~1980, sea surface temperatures and surface air temperatures have been steadily increasing within the Pacific Arctic Region (Richter-Menge et al. 2017, Overland et al. 2018). Amidst these extreme changes, it is vital to develop a better understanding of implications on the physical, chemical and biological properties of this ecosystem.

The Chukchi Sea region is represented by short food chains and strong pelagic-benthic coupling, where sinking carbon from spring and summer phytoplankton blooms provides a major food source to the underlying benthic fauna, such as bivalves, sea stars and amphipods. Between May and June, the sea ice begins its retreat in the Chukchi Sea; nutrient entrainment from winter mixing and increased light support high phytoplankton productivity, with average annual productivity reaching 184 - 208 g C m^{-2} (Hill et al. 2018). Some marine mammals, such as walruses, gray whales and sea ducks, rely on the benthic organisms as a food source as pictured in the conceptual diagram in Figure 1.2 (Grebmeier et al. 2006b, Darnis et al. 2012).

The Chukchi Sea, like the rest of the Arctic region, is facing an uncertain future, exhibiting a significant warming trend and an overall decline in sea ice cover. Summertime temperature anomalies have been measured at +2.5 °C across the Pacific Arctic Region (Frey et al. 2014). Moreover, the Chukchi Sea is experiencing a decline in annual sea ice persistence, or the number of days in a year with sea ice presence, (>30 days/decade; Figure 1.3) and sea ice thickness (~51.2 cm/decade). Earlier ice break-up (~10 days/decade) in the spring and later sea ice formation (~20 days/decade) in the winter are perpetuating the sea ice decline in this region (Frey et al. 2014). Longer periods of open water allow more heat to be absorbed during the summer months, creating a positive feedback loop of warmer water and postponing ice formation in the autumn months (Frey et al. 2014), causing various regions of the Arctic Ocean to become characterized by more seasonal sea ice rather than persistent multiyear sea ice (Steele et al. 2008, Maslanik et al. 2011, Frey et al. 2015). The increase of freshwater resulting from additional sea ice melt enhances stratification and limits mixing, thereby reducing the injection of nutrients into the euphotic zone from subsurface waters (Mathis et al. 2014).

The physical and nutrient conditions in the seasonal ice zone of the Chukchi Sea are influenced by three water masses, the Alaska Coastal Water (ACW), Anadyr Water (AW) and Bering Shelf Water (BSW), that are formed in the spring as Pacific Ocean water passes through the Bering and Chukchi Sea on their way to the Arctic Basin, seen in Figure 1.4 (Coachman and Aagaard 1988, Brugler et al. 2014). The AW (-1.0 to 1.5 °C) has a higher nutrient content (e.g. >25 μM NO_3; Walsh et al. (1989)) and salinity (>32.5 psu) than the other currents (Grebmeier and McRoy

1989). The ACW is warmer (>4 °C), less saline (<31.8 psu) and contains the lowest concentration of nutrients (e.g. 5 μM NO_3; Walsh et al. 1989) compared to the other two water masses (Grebmeier and McRoy 1989). The AW and BSW mix after flowing north through the Bering Strait to form Bering Shelf-Anadyr Water (BSAW; Grebmeier et al. (2006a)), then diverges north of the Bering Strait, flowing into both the Central Channel and along the coast of Alaska into Herald Canyon (Pisareva et al. 2015).

1.2. Phytoplankton ecology

Phytoplankton community ecology and phenology during the spring and summer in the Chukchi Sea are influenced by several factors, such as the timing of seasonal ice retreat, nutrient concentrations, temperature and water column stratification. Sea ice breakup in the Chukchi Sea begins in the south around April-May and currently progresses to the northern Chukchi Sea as early as mid-July (Frey et al. 2019). Phytoplankton blooms are initiated by the increase of light penetration to the surface ocean under the ice as snow cover melts and melt ponds form. Under ice and ice edge blooms are dominated primarily by large diatoms (> 20 μm) (Gradinger 2009, Cai et al. 2010, Arrigo et al. 2014). The diatom-dominated communities are driven by an increase in light and nutrients regenerated during the winter (Werner et al. 2007, Fripiat et al. 2014) that sink out to become a food source to the very rich and productive benthic communities (Grebmeier et al. 2006a).

On the western side of the Chukchi Sea, the larger diatom blooms persist through the summer because they are supported by the nutrient rich BSAW. As spring moves into summer in the eastern Chukchi Sea, the open waters are warmed by

exposure to the sun and become stratified. The surface water becomes depleted of nutrients as the algal blooms occur, and stratification prevents water column mixing, thus limiting the ability of large diatoms to grow. This region, dominated by larger diatoms during the spring, transitions to a community of smaller phytoplankton with lower nutrient requirements, such as prasinophytes, haptophytes, and small diatoms (Hill et al. 2005, Lee et al. 2007). However, it was recently determined that some areas of the Chukchi Sea can sustain diatom blooms for a longer period, such as around Barrow Canyon (Lowry et al. 2015). Lowry et al. (2015) suggested that a nutrient rich water mass called Winter Water (WW), which is produced through brine rejection during sea ice formation in the winter within the Bering and Chukchi Seas may play an important role in supporting subsurface phytoplankton blooms in the summer after sea ice retreat, particularly on the Chukchi Shelf (Woodgate et al. 2005a). Moreover, vertical mixing events can also replenish nutrients within the upper ocean, supporting diatom blooms (Ardyna et al. 2011).

Clearly, phytoplankton bloom phenology, magnitude (biomass) and community (taxonomic) structure in the Chukchi Sea are driven strongly by such environmental factors as photosynthetically active radiation (PAR), the location of the sea ice edge, and nutrients. The predictable seasonality of phytoplankton growth and bloom formation are important to the food web dynamics and overall ecosystem health of the Chukchi Sea. Gaining an enhanced understanding of the environmental mechanisms that drive these relationships and the phytoplankton traits that influence when and where specific species bloom and persist, are important to understand the implications of the predicted changes in the Arctic such as a longer open water

season, earlier phytoplankton blooms and increased stratification on biological community structure.

1.3 Remote sensing and the Chukchi Sea

Ocean color satellite instruments measure spectral radiance from the top of the atmosphere. Remote sensing reflectances ($R_{rs}(\lambda)$) are estimated, after the atmosphere is removed, from the spectral radiance by specific algorithms. The general relationship between $R_{rs}(\lambda)$ and water column inherent optical properties (IOPs) is approximated by the following equation:

$$R_{rs} = \frac{b_b}{a + b_b}$$

where b_b is backscatter and a is total absorption (Sathyendranath and Platt 1997, Maritorena et al. 2002). Total absorption, a, can be further broken down into its individual components: the absorption by pure water (a_w), by particles (a_p), by phytoplankton (a_{ph}) and dissolved compounds (a_g). Backscatter, b_b, can be broken down to its individual parts of backscatter by water (b_{bw}) and by particles (b_{bp}). From $R_{rs}(\lambda)$ an algorithm is used to derive Chlorophyll a (Chl*a*), a proxy for phytoplankton biomass (O'Reilly et al. 1998). Using the relationship of $R_{rs}(\lambda)$ and IOPs, we can implement bio-optical algorithms and models, such as the Quasi-Analytical Algorithm or QAA (Lee et al. 2002) and the Generalized IOP model or GIOP (Werdell et al. 2013) to derive individual constituents.

Ocean color and satellite-derived Chl*a* were recently recognized as essential climate variables (ECVs) by the Global Climate Observing System (GCOS), an internationally recognized organization that oversees the continuity and improvement

of global climate observations and measurements (Sathyendranath et al. 2019). An ECV is defined as a "physical, chemical or biological variable or a group of linked variables that critically contributes to the characterization of Earth's climate"[1]. Measurements of phytoplankton taxonomy, diversity and distribution are considered Essential Ocean Variables (EOVs) and Essential Biodiversity Variables (EBVs) (Lindstrom et al. 2012, Pereira et al. 2013, Muller-Karger et al. 2018). Phytoplankton diversity and abundance are indicators of ecosystem status and can be considered one of the canaries in the coal mine with regards to climate variability. Time series data that include ECVs, EOVs and EBVs are critical to understanding large scale environmental and ecosystem variability over longer time scales (Boss et al. 2020). Some large-scale changes in phytoplankton communities, or domain shifts, have already been observed within select systems. For example, within the past 16 years (1998-2013) the surface warming in the subtropical gyres caused a decline in Chl*a* of up to 16% and 23% reduction in phytoplankton carbon production (Signorini et al. 2015). For the Southern Ocean, analysis of a 21-year record of satellite derived Chl*a* indicates that phytoplankton biomass has increased, indicating a longer growing season, particularly in the winter season (Del Castillo et al. 2019). Such an increase in phytoplankton biomass will likely affect the biological pump in the Southern Ocean. For the North Atlantic, a multi-decadal analysis of Continuous Plankton Recorder data suggested that coccolithophore occurrence has increased an order of magnitude from 1965-2010 (Rivero-Calle et al. 2015). In coastal waters off the northeast US, a 13-year study at the Martha's Vineyard Coastal Observatory showed a change in the

[1] https://gcos.wmo.int/en/essential-climate-variables

phenology of spring blooms of *Synechococcus* associated with temperature trends (Hunter-Cevera et al. 2016). Current long-term observing systems, e.g., the Distributed Biological Observatory (Grebmeier et al. 2019), and planned long-term observing systems e.g., Saildrones[2] (De Robertis et al. 2019, Gentemann et al. 2020), and ARGO floats (Smith et al. 2019), that collect ECVs will be invaluable.

Retrieval of satellite ocean color images in the polar regions is not without its challenges. A solar zenith angle of > 70° is observed at high latitudes at most times of the year, which is thought to nullify the application of atmospheric correction algorithms that were developed for lower angles. For the rest of the year, ice cover, clouds and fog prevent passive ocean color retrieval much of the year. The presence of colored dissolved organic matter (CDOM) also complicates the retrieval of Chl*a* because CDOM absorbs at the same wavelengths as Chl*a*, as seen in Figure 1.5 (Bélanger et al. 2008). Despite these challenges, accurate remote sensing retrievals of bio-optical properties, including Chl*a,* are possible in the Chukchi Sea (Chaves et al. 2015, Kahru et al. 2016). The partitioning of total absorption into its individual constituents using satellite algorithms such as GIOP and QAA in a region of interest can be used to derive optical water types of marine assemblages and used to monitor changes in particle loads, phytoplankton biomass and assemblages, and carbon export (Neukermans et al. 2014, 2016).

1.4 Rrs and the accuracy of absorption measurements

In situ measurements of a_p are important for validation and development of inverse models where R_{rs} is used to derive IOPs a and b_b. Data collection and

[2] https://www.saildrone.com/news/2018-chukchi-sea-carbon-fisheries

analytical methods change and improve over time as technology advances. Recent developments of sampling and measurement protocols by the international oceanographic community, such as the International Ocean Colour Coordinating Group Absorption Coefficient protocol (Neeley and Mannino 2018), reinforce the need for standardization of field measurements and data processing. Not only are accurate field measurements important for algorithm validation and uncertainty estimates, many of the properties derived from ocean color, like a_{ph} are used to derive phytoplankton size classes (Ciotti and Bricaud 2006, Devred et al. 2011) and as input for global ecosystem models that help us understand the possible long-term effects of climate change (Dutkiewicz et al. 2015). Moreover, characterization of the in-water light field through the in situ and satellite measurement of absorption and scattering is important for understanding phytoplankton community/primary production and growth, as well as biogeochemical cycles (e.g., the fate of carbon). Therefore, the importance of uncertainty quantification is three-fold: 1) for assessing in situ and satellite instrument performance, 2) for selecting the appropriate scaling of validation efforts for satellite-derived products, and 3) development and validation of global models. Uncertainties in the measurement and computation of in situ properties, including a_p, are important to understand and quantify as they propagate to algorithm and model parameterization and validation.

1.5 Ocean color and ecosystem trends

Margalef's concept of phytoplankton succession describes mechanisms by which nutrients and turbulence drive phytoplankton dynamics (Margalef 1978). Within this framework, smaller phytoplankton cells dominate in calm, low nutrient

environments while larger cells succeed in areas with greater turbulence and nutrient concentrations (Figure 1.6). Although there may not be a 'one size fits all' categorization for phytoplankton species, when we understand the underlying mechanisms that influence the ecological niches of Arctic phytoplankton, we may be able to predict responses of phytoplankton dynamics and phenology to changes in the Arctic environment. Ocean color is essential for understanding these long-term trends in phytoplankton phenology and ecosystem status.

Ocean color data and associated derived products are used to study global ocean phytoplankton dynamics and carbon cycling and are, therefore, essential to studying the marine ecosystem feedbacks related to climate variability. Time-series ocean color observations are important for understanding phytoplankton bloom dynamics, as well as domain shifts in phytoplankton communities in response to the changing environment. High temporal and spatial resolution observations, whether in the Arctic or anywhere else in the global ocean are just not feasible as we are limited by time and resources. Therefore, we must make use of additional tools to fill in the gap for global and regional oceanographic observations. Satellite ocean color observations provide global ocean coverage, reaching time and space beyond our capabilities with research vessels and, therefore, may fill in the data gap where observations are limiting.

The optically active constituents, meaning any particulate or dissolved matter that absorbs and scatters light, influence the spectral shape and magnitude of $R_{rs}(\lambda)$ thereby creating its apparent color 'fingerprint'. (Figure 1.7). For example, the Forel-Ule scale, first described in 1892 (Ule 1892, Novoa et al. 2014) has been used for

years to qualitatively describe twenty-one different optical water types from blue to green to brown, based on the apparent color or "dominant' of the water and track changes in phytoplankton abundance (Wernand et al. 2013, Garaba et al. 2015). A most recently developed tool, Apparent Visible Wavelength, reduces the $R_{rs}(\lambda)$ spectrum to one number that represents the apparent color of the water (Figure 1.7). This number simplifies the evaluation of trends in AVW, which is representative not only of phytoplankton biomass and type, but other optically active constituents (Vandermeulen et al. in Review).

Because the size, shape and pigment composition of phytoplankton contributes to $R_{rs}(\lambda)$, it acts as a signal for large scale trends at the ecosystem level, used to track changes in the biology (e.g., phytoplankton abundance, phenology) and chemistry of the ecosystem without the natural variability or uncertainties of derived products (e.g., Chl*a*). Knowing that the physical environment of the Chukchi Sea is being altered by earlier sea ice breakup, later sea ice formation, and longer open water duration, spatio-temporal trends of biological and chemical features of the Chukchi sea will likely manifest within the $R_{rs}(\lambda)$ spectrum. By connecting the dots between, absorption (phytoplankton, non-algal particles and CDOM) and coincident biogeochemistry, we can track long-term trends in an ecosystem and concomitant trends in ocean color. To this end, future satellite ocean color instruments, such as PACE (Cetinic et al. 2018), will provide the advanced capability of collecting hyperspectral $R_{rs}(\lambda)$, inevitably increasing the amount of spectral information that we will use to relate the apparent color of the surface ocean to optical properties and the biogeophysical characteristics of the surface ocean.

1.6 Project objectives

The purpose of my dissertation is to investigate the underlying mechanisms that may influence phytoplankton community structure in the Chukchi Sea and to evaluate existing tools, such as satellite ocean color data, to monitor ecosystem dynamics in the changing Arctic environment. The objectives of this study are individually addressed as chapters of the dissertation and are as follows:

1. Quantify the accuracy and precision of field measurements that may impact model and algorithm development and validation.
2. Understand the intricate interactions of phytoplankton with their chemical and physical environment in the Chukchi Sea through a multivariate statistical analysis of community structure.
3. Apply time series satellite data to evaluate the spatial distribution of remote sensing reflectance spectral shapes in the Chukchi Sea and relate these 'optical fingerprints' to the trends in Chl*a*, sea ice concentrations and sea surface temperature.

Figures Chapter 1

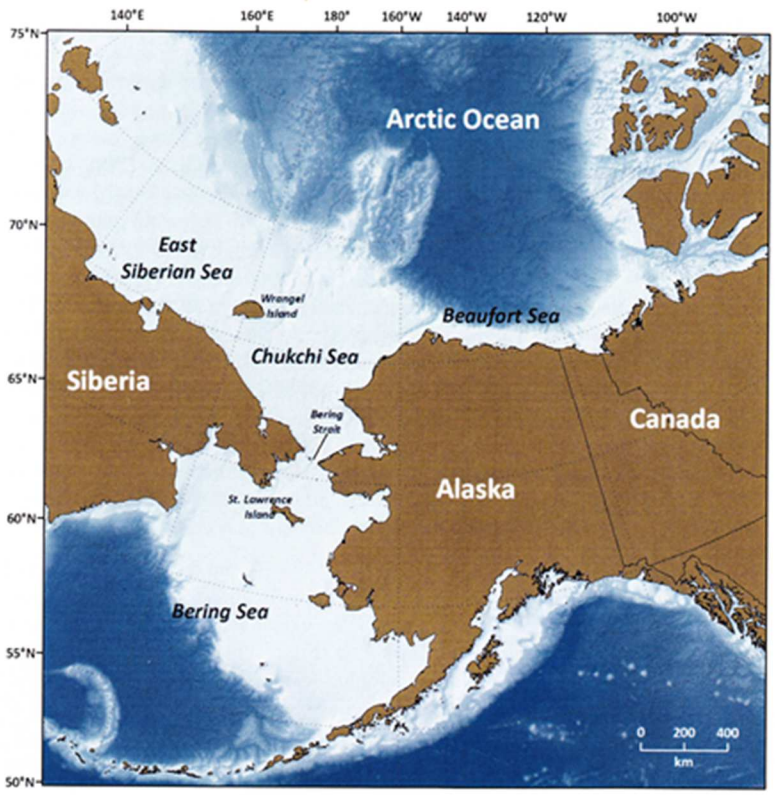

Figure 1.1. Map of the Chukchi Sea [From Grebmeier and Maslowski (2014)].

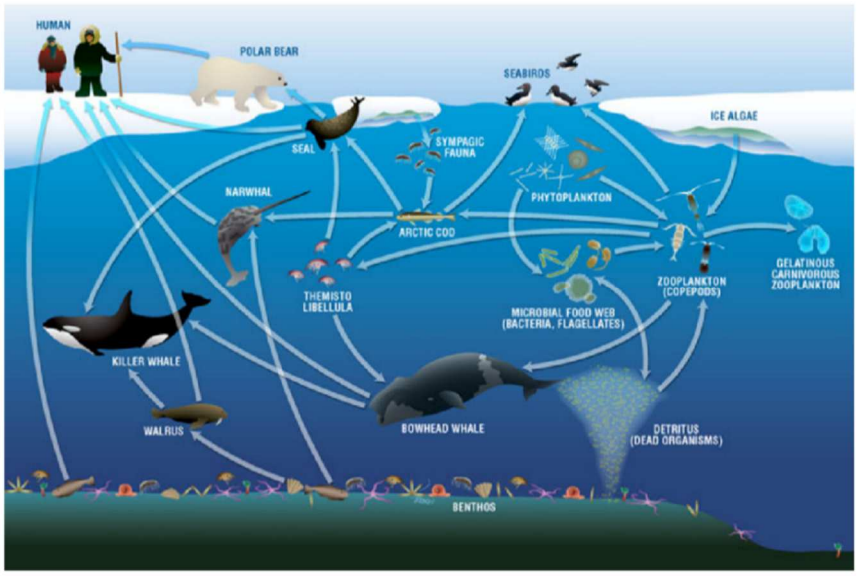

Figure 1.2. Arctic food web dynamics. [Figure from Darnis et al. (2011)].

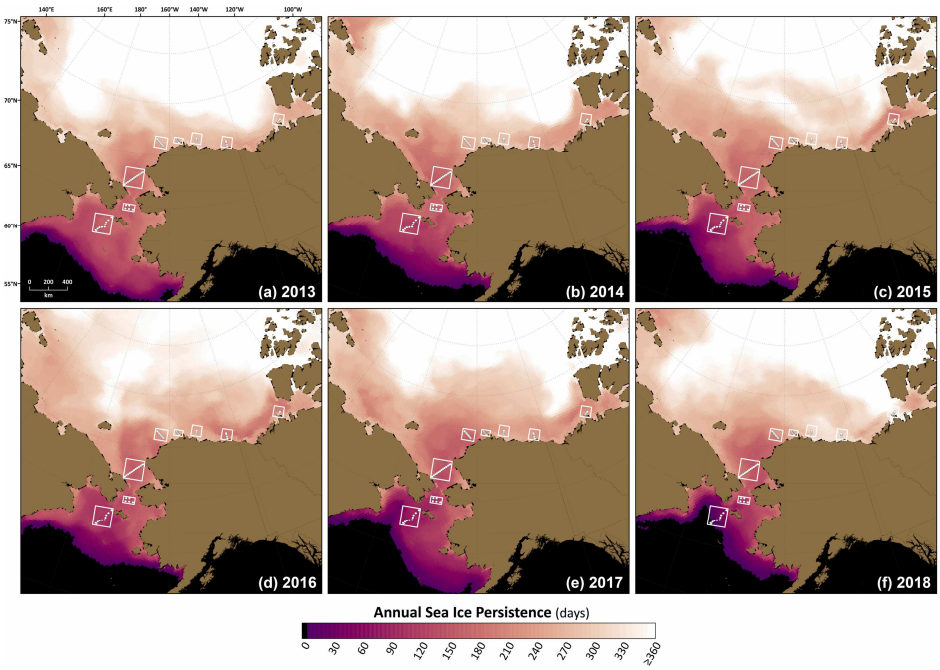

Figure 1.3 Declining annual sea ice persistence is observed in the Chukchi Sea, 2013-2018. Sea ice concentrations were determined from SSM/I and SSMIS imagery. [Figure from Grebmeier et al. (2019)]

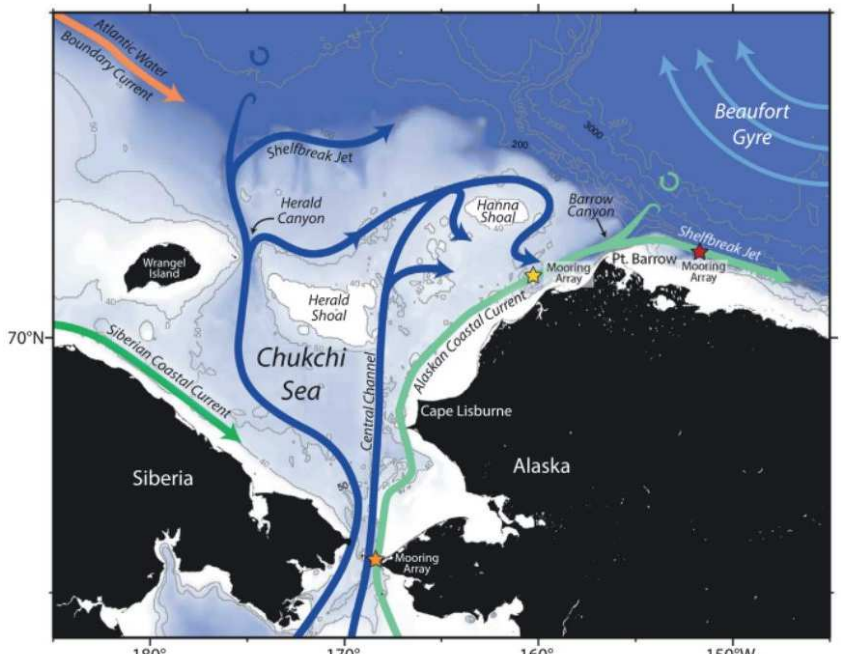

Figure 1.4. Major water masses in the Bering and Chukchi Seas. [Figure from Brugler et al. (2014)]

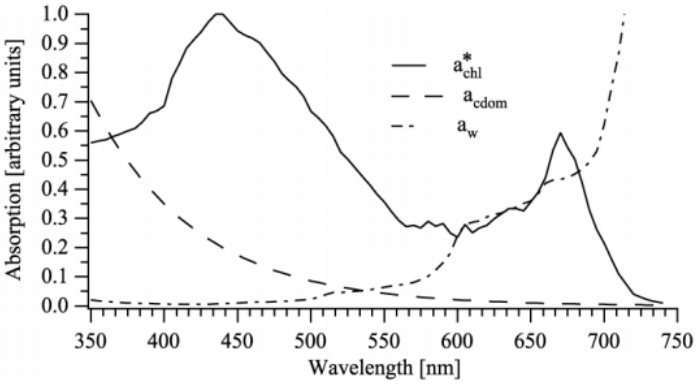

Figure 1.5. Example absorption spectra for Chl*a*-specific absorption by phytoplankton, CDOM and water.

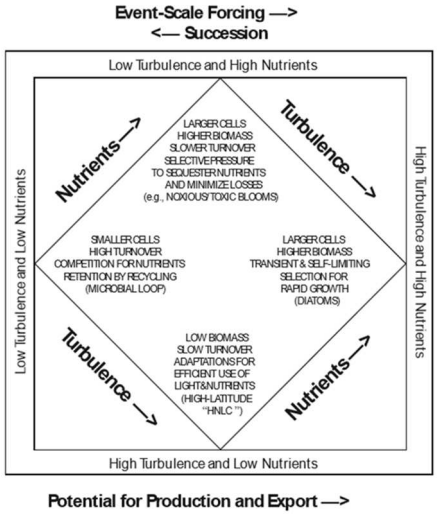

Figure 1.6. Margalef's phytoplankton succession framework later revised by Cullen et al. 2002.

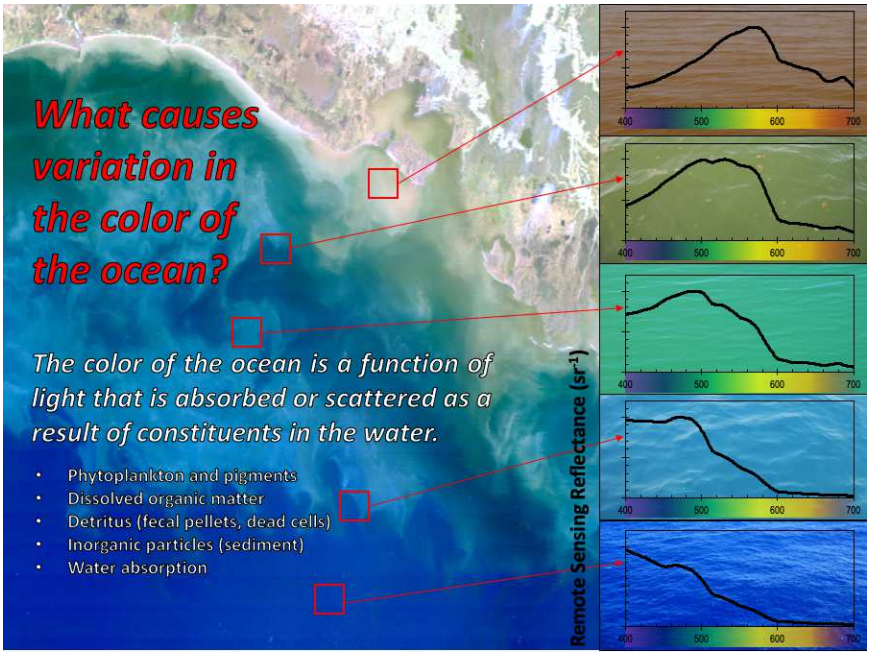

Figure 1.7. A schematic that shows how the scattering and absorption of light Influences the spectral shape of $R_{rs}(\lambda)$. The red boxes that surround portions of the ocean color figure are identified by the light spectra on the right side of the figure.

Chapter 2: A multi-method approach to quantify uncertainties in the measurements of light absorption by particles

2.1 Introduction

The variability in the global ocean has been monitored for > 20 years by satellite-borne ocean color sensors. A number of critical uses for ocean color are of particular importance in today's society. Remote estimates of algal biomass are essential in computations of ocean productivity and ultimately impact our characterization of the global carbon cycle (Behrenfeld et al. 2005). Satellite imagery has been used to monitor inter-annual variation in the timing and extent of phytoplankton blooms, which are connected to the survival of larval fish (Wilson et al. 2008). Moreover, satellite derived sea surface temperature (SST) and wave height information can help aquaculture developers plan where to establish new fish farms. Additionally, satellite imagery can be used to detect and monitor blooms of harmful algae and can inform monitoring efforts for delicate ecosystems, particularly in global coastal environments.

The spectrally-dependent backscattering (b_b) and total absorption (a) coefficients (in units of m^{-1}) of light by the dissolved and particulate constituents in water (the inherent optical properties, IOPs) ultimately control the color of the ocean (Preisendorfer 1976, Morel and Prieur 1977). The properties of this light are used to derive information about the biogeochemical components of the water column, such as the amount of carbon or the abundance of phytoplankton. Remote sensing reflectances (R_{rs}), the light that emerges from the ocean, are used to derive a with bio-optical algorithms and models, such as the Quasi-Analytical Algorithm (Lee et al.

2002). Garver-Siegel-Maritorena algorithm (Maritorena et al. 2002) and the Generalized IOP model (Werdell et al. 2013) to name a few. The general relationship between R_{rs} and IOPs includes the effects of backscattering and can be approximated by Eq. (1) (Sathyendranath and Platt 1997, Maritorena et al. 2002).

$$R_{rs} = \frac{b_b}{a + b_b} \tag{1}$$

The total absorption, a, can be separated into a set of components using Eq. (2), where a_w is spectral absorption by pure water, a_p is spectrally-dependent absorption by particles and a_g is spectrally-dependent absorption by dissolved constituents.

$$a = a_w + a_p + a_g \tag{2}$$

The a_p component can be further broken down to the absorption due to phytoplankton (pigmented particles; a_φ) and non-algal particles (NAP; a_d) by Eq. (3). The parameters a_p and a_φ can be derived analytically using additional bio-optical models (Bricaud et al. 1998, Devred et al. 2011).

$$a_p = a_\varphi + a_d \tag{3}$$

Collection of *in situ* a_p data can be accomplished in the field and in the laboratory in multiple ways (Mitchell et al. 2003, Mueller 2003). One common method, the quantitative filter technique (QFT), was first developed by Yentsch (1962) and later modified by Mitchell (1990) where particles are concentrated onto a filter pad. Absorbance, or optical density of particles on a filter (OD_f; typically defined on the base of the decadic logarithm), is measured with a spectrophotometer and is converted to a_p using Eq. 4, where 2.303 is the natural log of 10, A_{fp} is the

clearance area of the filter pad, V_f is the filtration volume, V_f/A_{fp} is the theoretical geometric path length and β is the pathlength amplification correction (Eq. 4). The scattering of light by the filter pad and particles amplifies the photon pathlength and falsely increases the value of absorption (Butler 1962). Therefore, β is included in the computation of a_p to scale the absorption measured on the filter pad to a predicted value of absorption in suspension. Additionally, the absorbance of algal and non-algal particles can be de-convolved by measuring the samples before and after extraction of algal pigments and their corresponding coefficients can be calculated using Eq. 4 (Kishino et al. 1985, Hoepffner and Sathyendranath 1992). Direct measurements of a_p in suspension can be made with a spectral absorption and attenuation meter or AC-meter (e.g., AC-S; WetLABS Inc.), or a Point Source Integrating-Cavity Absorption Meter (PSICAM) (Bricaud and Stramski 1990, Röttgers et al. 2007).

$$a_{p,d} = 2.303 \frac{A_{fp} OD_f}{V_f \beta} \tag{4}$$

Three methods commonly applied to determine a_p using particles collected on a filter pad include: the transmittance method (T) (Bricaud and Stramski 1990, Mitchell 1990, Roesler 1998), the transmittance-reflectance method (T-R) (Tassan and G.M. Ferrari 1995,2002) and the inside sphere method (IS) (Maske and Haardt 1987, Röttgers and Gehnke 2012, Stramski et al. 2015). Each method requires a different geometric configuration and is susceptible to different levels of scattering error (Table 2.1). Theoretically, the configurations of the T-R and IS methods reduce scattering error (loss of photons scattered from the filter pad and particles) producing

a more precise measurement (Kishino et al. 1985, Tassan and Ferrari 1995, Röttgers and Gehnke 2012, Stramski et al. 2015).

Many βs have been determined empirically (Bricaud and Stramski 1990, Mitchell 1990), and two βs have been derived analytically (Roesler 1998, Lohrenz 2000). Historically, β is the ratio of OD_f to the optical density of particles in a dilute suspension (OD_s), a true measurement of absorption. The source of these suspensions and filter pad samples were commonly from cultures (Roesler 1998). A power law or quadratic function and associated coefficients were calculated from a least square's regression of OD_s and OD_f, which can then be applied to field samples to derive a relationship. These βs do not necessarily encompass all particle sizes and types encountered in the ocean and can be subject to bias. Consequently, the β is a major source of uncertainty for determining particle absorption coefficients by the filter pad methods. Although not definitely proven, there are some indications that suggest β is influenced by particle size and scattering properties (Maske and Haardt 1987, Bricaud and Stramski 1990, Babin et al. 2002, Naik and D'Sa 2012, Röttgers and Gehnke 2012). Other sources of analytical uncertainty have also been discussed (McKee et al. 2014).

In contrast, AC-meter uncertainties are in absolute terms, not percentage. The field calibration term is ~0.01 m^{-1}, and the instrument precision is about half of the calibration term. Temperature effects can create uncertainties near the peak of pure-water absorption of 0.02 m^{-1}. Lee et al. (2015) claims a ~0.005 m^{-1} difference in the blue part of the spectrum (350-415 nm) in pure water. By far the largest source of

uncertainty is that of the scattering correction (Slade et al. 2010, Röttgers et al. 2013, Lee et al. 2015).

The satellite ocean color community uses field and laboratory measurements of absorption coefficients to develop, evaluate, and validate their remote-sensing bio-optical algorithms. To maximize the spatial and temporal extent of data included in such analyses, agencies such as NASA typically invest in a broad range of investigations and require that the data collected subsequently be permanently archived in a central database. NASA has invested in the development of rigorous quality and assurance metrics and measurement protocols to enable high quality data collection and to minimize investigator-to-investigator and instrument-to-instrument differences in the archived data. The NASA Ocean Optics Protocols for Satellite Ocean Color Validation (Mitchell et al. 2003) is a standard set of protocols for radiometric and biogeochemical measurement, the purpose of which is to provide measurement consistency across ocean color missions and research groups with tenable error assessments. Moreover, strict adherence to the protocols increases the probability that biogeochemical and radiometric measurements provide sufficiently accurate measurements for satellite derived product validation. In spite of the rigorous protocols developed for the measurement and computation of a_p, relative measurement uncertainties are inherent in the choices of sample analysis and a_p computation within each of these protocols.

Biogeochemical algorithms and models require high quality observational ground-truth data for both development and validation. The SeaWiFS Bio-optical Archive and Storage System (SeaBASS) is a publicly available, community-driven

archive of *in situ* bio-optical data maintained by the NASA Ocean Biology Processing Group (OBPG) at NASA Goddard (Werdell et al. 2003, Werdell and Bailey 2005). Approximately 20,000 a and a_p products derived from various field measurements can be found in SeaBASS and have been acquired multiple ways by any number of researchers. Despite the existence of community-vetted protocols and quality assurance metrics, a number of questions remain: What is the uncertainty of many researchers using different analytical methods and computational techniques for deriving a_p? To what degree are they different? Our goal here was to quantify precision of these measurements so that these uncertainties may be accounted for during model development and validation.

In this paper we address measurement agreement, or precision among multiple methods for determination of the same parameter. Three different sample sets were used to characterize uncertainties in a dynamic range of absorption from a high particle concentration with higher Chlorophyll a (C_a) concentration to lower particle concentration and lower C_a concentration. The ultimate goal was to quantify the uncertainty associated with the diverse analytical methods and computational techniques to derive a_p, and to show a test case of how these uncertainties could affect model-measurement closure. Here we are identifying the lack of precision of derived a_p as uncertainty. We cannot address the accuracy of a_p measurements here because there is no existing suspended particle absorption standard, nor did we measure suspended particle samples in parallel with the filter pad samples. Instead, we offer alternative approaches with which we endeavored to address uncertainty associated with:

1) Two analytical methods for collecting absorbance data (measurement precision)
2) Six computational techniques for deriving a_p (determination precision, hereafter referred to as uncertainty)
3) Comparison of the QFT-derived a_p to a_p measured with an AC-S
4) Comparison of measured against modeled a_p

Although similar method evaluations have been approached in previous studies (Röttgers and Gehnke 2012, Stramski et al. 2015) in this paper we conduct a valuable performance and statistical analysis that is independent from the original method papers using real world samples.

2.2 Methods

2.2.1 Sample collection

Three sources of filter pad samples and AC-S measurements of a_p were used in the comparison: one set collected off the coast of Hawaii ("Blue Water") shown in Fig. 2.1(a), another set collected off the coast of the eastern United States ("Coastal Water";) shown in Fig. 2.1(b) and the third set from laboratory cultures. Table 2.2 shows station numbers and depths at which AC-S and filter pad samples were collected concurrently in the field. Filter pad samples were collected in duplicate by vacuum filtration (~127 mmHg) onto pre-combusted 25 mm Whatman GF/F filters. Samples were placed in HistoPrep tissue capsules, flash frozen in liquid nitrogen and stored at -80° C until analysis. Samples for C_a determination were collected similarly and stored in foil. Phytoplankton pigments were determined using high performance liquid chromatography (HPLC) following the procedures of Van Heukelem and

Thomas (2001) and further described in Hooker et al. (2005). Filter pad and AC-S measurements were collected in the laboratory from dilutions of three phytoplankton species: *Thalassiosira weissflogii* (CCMP 1387), *Emiliania huxleyi* (CCMP 371), and *Nannochloropsis sp.* (15 duplicate filters). The cultures were diluted with filtered and sterilized seawater to attain the following dilution series 100%, 42%, 20%, 10% and 5%. Only the three lowest dilutions (20%, 10% and 5%) of each culture were measured with the AC-S (a total of nine measurements). For each sample source, one replicate filter was analyzed using the T method and the other with the IS method. For the culture experiment, fresh filter pad samples were used for the measurements.

2.2.2 Instrument configurations and analysis techniques

Measurements of OD_f with the T method were conducted using a Perkin Elmer Lambda 35 UV-Visible, dual beam spectrophotometer following the protocol of Roesler (1998). Briefly, the sample and reference beams were balanced by placing a neutral density filter (ESCO optics; Density=1.0) at the reference port. The sample filter was placed in the path of the sample beam. Measurements of OD_f with the IS method were conducted using a Cary 100 UV-Visible dual beam scanning spectrophotometer equipped with a 15 cm integrating sphere (Labsphere DRA-CA-30) and using the protocol of Stramski et al. (2015) and applied in Neukermans et al. (2014). The filters were placed in the center of the integrating sphere using a Plexiglas slide. For both methods, scans were performed between 290-800 nm with a 2 nm Slit Band Width (SBW), and 240 nm per minute scan speed. For both filter pad analysis methods, blank filters were moistened with 0.2 μm-filtered artificial seawater (ASW). Blank filter and air scans (for the IS method) were measured throughout the

day to monitor instrument drift. For both configurations, blank filter scans were subtracted from the raw OD_f spectra prior to a_p computation.

A fraction of scattered light is not detected using the T method due to its geometric configuration. To reduce this scattering error, a null point correction is applied that assumes there is no absorption by particles in the near infrared part of the spectrum (Roesler 1998, Mitchell et al. 2003). Data from the T measurements were null-point corrected by subtracting the average absorbance between 750 nm and 800 nm from the entire spectrum.

2.2.3 a_p computation

Three different βs were chosen for the T method and two βs were chosen for the IS method to compute $a_{p,}$ (Eq. 4) and are listed in Table 2.3, although others exist in the literature. The technique for which a_p is derived from each β will hereafter be referred to as a 'computational technique'. We are not endorsing one β over another, as it is currently not possible to prove the accuracy of a given approach. To reiterate, our goal is to make a general statement about uncertainties of existing data and the most commonly used analytical methods and computational techniques.

2.2.4 AC-S measurements

Spectral particle and dissolved absorption (a_{pg}) were measured between 400-750 nm using a WETLabs AC-S instrument. In the field, the AC-S was calibrated with ultrapure water and a mean of three days' calibrations was used to subtract the pure water offset. AC-S profiles were made at each station. For the Coastal Water measurements, the AC-S was mounted horizontally to the CTD rosette on an

auxiliary ring. The mean spectra during the period of bottle firing, approximately 90 seconds, were calculated. For the Blue Water samples, the mean spectra at each depth +/- 1 m were used.

Post processing involved merging the CTD with the AC-S by time stamp, adjusting for the time required for water to move from the intake to the center of the flow tube. For all AC-S measurements, corrections for salinity, temperature, and instrument drift were made, using the methods of Sullivan et al. (2006). For the Blue Water and Coastal Water a_{pg} measurements the proportional scattering correction (Eq. 4) of Röttgers et al. (2014) was applied using an empirical ratio of absorption at 715 nm and correcting for attenuation as well as absorption. For the culture a_{pg} measurements, three dilutions of each culture (20%, 10%, and 5%) were passed through the AC-S flow tubes, and the subsequent absorption values were corrected for scattering using proportional correction (Zaneveld et al. 1994).

Conventionally, a_p is calculated by subtracting the absorption of 0.2 μm filtered seawater (a_g) from a_{pg}, as was done for the laboratory culture experiment and the Blue Water data in this study. For the blue water, two AC-S meters were used: one with a 0.2 μm pre-filter and one without. In the laboratory, the same meter was used for both measurements, allowing for calibration-independent measurement of a_p (Slade et al. 2010). During the coastal cruise, a filter was not used, thus concurrent a_g measurements were not performed. Instead, discrete a_g samples were later measured using a bench top spectrophotometer and subtracted from a_{pg} to retrieve a_p. The value of a_p at 555 nm for Station 8 was removed from the analysis because it was negative, possibly an artifact of subtracting the laboratory-measured a_g.

2.2.5 Modeling a_p

In ocean optics, identification of uncertainty is important to assess instrument performance and is essential for the appropriate scaling of validation efforts for satellite-derived products. Model output is dependent on empirical data. Therefore, a lack of precision between measurements and models could mean either the instruments, models, or both are faulty.

Our aim was to investigate if differences in a_p computational techniques influenced model development and measurement-model closure using a case study approach with one candidate model. We chose a power law, Eq. (5), that estimates a_p from the following relationship with chlorophyll (Eq. (1) in Bricaud et al. (1998)).

$$a_p = AC_a^B \tag{5}$$

where A and B are derived coefficients from (Bricaud 2013). Bricaud et al. (1998) recommended that this model only be applied to Case 1 waters where the optical properties are determined mainly by phytoplankton and dissolved organic matter and when C_a concentration is maximally 10 mg/m^3. The Coastal Water samples are not considered Case 1; however, we still applied the model as our chlorophyll concentrations fell well within this chlorophyll range, although the concentration of suspended sediments is usually greater in the coastal waters.

Performance of the model against the measured a_p was determined using a model skill score (SS) metric (Ralston et al. 2010). The skill score is calculated using Eq. (6).

$$SS = 1 - \frac{\sum_{i=1}^{N} (X_{\mathrm{mod}} - X_{obs})^2}{\sum_{i=1}^{N} (X_{obs} - \overline{X}_{obs})} \tag{6}$$

where X_{mod} and X_{obs} are the modeled and observed values, respectively, and $\overline{X}_{obs}$ is the mean of the observations. A value of +1 indicates that the model agrees with the observations. A value of 0 indicates that the model and the mean of the observations exhibit equal predictive power and negative values indicate that the model is less predictive than the mean of the observations. An SS > 0.65 was considered very good, 0.2-0.5 as good and <0.2 as poor (Ralston et al. 2010). Additionally, Root Mean Square Error (RMSE) was calculated as a measure of the error between the measured data and the model predictions using Eq. (7) where y_i is an observation and Y_i is the predicted value.

$$RMSE = \sqrt{\frac{1}{n} \sum_{i=1}^{n} (y_i - Y_i)^2} \tag{7}$$

2.3 Results and Discussion

The measurement precision of OD_f and uncertainty of a_p were evaluated using three different particle concentrations and types: low particle concentration natural samples (Blue Water) shown in Fig. 2.2(a), high particle concentration natural samples (Coastal Water) shown in Fig. 2.2(b), and phytoplankton-derived samples (10% dilution *Emiliania huxleyi*) shown in Fig. 2.2(c). A smoothing technique was not applied to these data. Note the differences in absorption magnitude (y axis) between the samples. Spectra measured with the T method were noisier than the spectra measured with the IS method because the geometric configuration of the T

method allows for a greater loss of photons scattered from the filter pad and particles thereby reducing the signal-to-noise ratio. The geometric configuration of the IS method favors the collection of most of the scattered photons, increasing the signal-to-noise ratio (Stramski et al. 2015). Therefore, OD_f measured with the IS method is approximately 50% greater in magnitude and less noisy than of those measured with the T method.

2.3.1 Analytical uncertainty of OD_f

Measurement precision of OD_f measured between the T method ($OD_f(T)$) and IS method ($OD_f(IS)$) was evaluated by computation of the median, mean and coefficient of variation (CV; standard deviation/mean*100%) of $OD_f(T)$ and $OD_f(S)$ for each data point. Additionally, the mean bias (mean difference of $OD_f(T)$ and $OD_f(IS)$) and mean ratio of $OD_f(T)/OD_f(S)$ were also determined. A null correction was applied to values of $OD_f(T)$.

2.3.2 Uncertainty of QFT derived a_p

The median, mean, and coefficient of variation for a_p were calculated from all computational techniques for the QFT methods only, at six OC wavelengths (Table 2.3). We acknowledge that calculated uncertainties in this analysis include sample collection error without measuring this error distinctly (difference between replicates). In previous analyses, our range of replicate uncertainty for a_p derived from the T and IS computational techniques typically ranged from <0.001% to 16% and 0.001% to 21%, respectively, although most values fell well below 20%.

The range of uncertainty of the QFT-derived values of a_p derived from all computational techniques was 7.07%-62.55% for all six wavelengths (Table 2.5). The values of a_p at 555nm showed the largest uncertainty overall with a maximum value of ~63%. As shown in Table 2.6, the %CV depended on absorption range and wavelength. The largest spread of a_p between all computational techniques occurred at 555 nm between 0.015 and 0.05 nm^{-1}.

2.3.3 Uncertainty of QFT and AC-S derived ap

The median, mean, and coefficient of variation were calculated for both QFT and AC-S derived a_p (Table 2.7). Here only coincident filter pad and AC-S field measurements of a_p (Table 2.1) and dilutions 20%, 10% and 5% of the laboratory cultures were included in the analysis. The addition of AC-S measured a_p increased the uncertainty to 7.48-119% for the six wavelengths (Table 2.7). a_p at 555 nm and 670 nm showed the highest uncertainty amongst the six wavelengths at 119% and 61.38%, respectively (Table 2.8).

The increase in uncertainty when the AC-S data are included in the analysis may be attributed to low signal, particularly for the Blue Water samples, and/or data computation technique. We used an average absorption for each sample depth +/- 1 m. Another analytical technique may be used to improve accuracy and decrease uncertainties. A source of bias exists when comparing particle absorption acquired from a filter pad and that acquired from using an AC-meter, depending on the water type. The QFT uses nominal 0.5-0.7 μm pore size fiberglass filters (Chavez et al. 1995) while a_p is separated from a by measuring the a_g from 0.2 μm filtered seawater.

In this way, the 0.2-0.7 μm fraction would be measured by the AC-S but not with the QFT methods (Roesler 2014).

2.3.4 QFT and AC-S ap trends

The individual a_p values from each sample were compared with the sample median to examine deviations of the method and computational differences from the median as indicated by their distance from the 1:1 line, shown in Fig. 2.3. The a_p values derived from the IS computational techniques exhibited a smaller deviation from the median than those values derived from the T computational techniques in most cases. Values of a_p from Roesler (1998) and Mitchell (1990) computations were consistently greater than the median across the absorption dynamic range for all wavelengths. Values of a_p from the Bricaud and Stramski (1990) computation were consistently lower than the median except for 443 nm where they were greater than the median at a_p values > 1.0 m^{-1}. Values of a_p from Röttgers and Gehnke (2012) and Stramski et al. (2015) were consistently similar to the median based on their close proximity to the 1:1 line.

The values of AC-S derived a_p exhibited low values most noticeably in the Blue Water samples at 443 nm, which are in the lowest region of the absorption range (<0.10 m^{-1}). Generally, AC-S measured a_p compared reasonably well to the median, falling below the 1:1 line at values < 0.2 m^{-1} and on or above the 1:1 line at values > 0.2 m^{-1}.

2.3.5 ap model evaluation

Model skill score, RMSE and the %CV of measured and modeled a_p (Tables 2.9-2.11) were calculated to evaluate measurement-model agreement for the Blue Water and Coastal Water data. One Coastal Water station was not used in this analysis because the C_a concentration exceeded the limit of 10 mg m^{-3} for this a_p model. At 443 nm, the model performed "very good" to "good" compared to all a_p computations from the Blue Water samples except for the AC-S where the model performed poorly (Table 2.9; SS = -0.4145). For the Coastal Water samples at 443 nm, the model performed poorly compared to all computed a_p but performed good compared to AC-S measured a_p (SS = 0.4247). At 555 nm, the model compared poorly to most of the Blue Water a_p values except for Mitchell (1990) and Roesler (1998) (SS = 0.2306 and 0.6145, respectively; Table 2.10). The a_p values for the Coastal Water samples also compared poorly except for BrSB Bricaud and Stramski (1990) and the AC-S measured a_p (SS = 0.3629 and 0.5715, respectively). At 670 nm, the model performed good to very good for both the Blue Water and Coastal Water a_p values, except for Roesler (1998) (SS = 0.0869; Table 2.11). In both water types the model performed the best in most cases when compared to a_p using the BrSB (Bricaud and Stramski 1990) method, particularly at 443 nm and 670 nm. Generally, the model performed best when compared to a_p computed from the T method.

2.4 Conclusions

Three different sample sets were used to characterize uncertainties in the determination of a_p for a dynamic range of absorption. The ultimate goal was to estimate the measurement precision of the methods for measuring OD_f, the

uncertainty of a_p derived from six computational techniques, and to show how these differences could affect model-measurement closure. Therefore, an understanding of measurement uncertainties is crucial and should be accounted for during model and algorithm development. Ignoring these uncertainties can result in poor model and algorithm performance. Moreover, measurement uncertainties can decrease the signal-to-noise ratio and a fraction of detected environmental variability may be lost to uncertainty. The desired result is to distinguish real variability from measurement error.

Variability in the magnitude of a_p in the field may be attributed to natural variability and the systematic uncertainties that accumulate with sample collection and analysis. Minimization of the noise is key to accurately identifying changes in the optical properties of the global ocean. McKee et al. (2014) suggest that incorporating measurement uncertainties, both random and systematic into the computation of C_a-specific absorption of marine phytoplankton may help to discriminate natural variability from measurement error. In this paper, we focused on the inherent systematic uncertainties that exist amongst the various methods for determining a_p. These uncertainties are important to understand and quantify as they propagate to algorithm and model development and validation.

Absorption at wavelengths in the blue-to-green region of the visible spectrum (443, 490, 510 nm) is mainly influenced by phytoplankton pigments and therefore may be used to derive information about phytoplankton community structure. Light absorption in the green and red part of the visible spectrum (555 nm and >670 nm; Table 2.12) can be attributed to phytoplankton pigments as well as minerals and

sediments. The 670 nm band also allows for the evaluation of chlorophyll fluorescence, which can be used to characterize primary production and nutrient stress of phytoplankton (Del Castillo et al. 2012).

In situ measurements of a_p are important for validation and development of inverse models where R_{rs} is used to derive IOPs a and b_b. For example, the relationship between phytoplankton size and pigment composition results in an empirically derived, non-linear function of C_a and a_p for use in algorithms (Bricaud et al. 1998, Chase et al. 2013). These derived parameters can then be used to develop empirical bio-optical and ecosystem models. Additionally, satellite-derived values of a_p and a_φ are important input vectors for modeling phytoplankton size classes (Sathyendranath and Platt 1997, Ciotti and Bricaud 2006, Devred et al. 2011). Characterizing phytoplankton functional types in the global ocean and understanding their role in global carbon cycling is of great interest to many researchers (Sathyendranath et al. 2014).

From the QFT comparisons we saw that the uncertainty of a_p derived from the IS computational techniques was small and consistent across all sample types (deviating least from the median) compared to the those derived from the T computation techniques. The values of a_p computed from Mitchell (1990) and Bricaud and Stramski (1990) computational methods performed consistently higher and lower, respectively, than the median absorption values. Values of a_p derived from the IS analysis method showed lower uncertainty compared to the median. The uncertainty in measuring a_p was similar across all wavelengths. The maximum uncertainty of 119% at 555 nm across all methods could be attributed to the minimum

absorption of pigments at that waveband and to the scattering differences between the reference and sample filters, which are amplified on applying the β to the absorbance spectra of the samples. Minimal absorption by phytoplankton occurs in the green region of the spectrum (555 nm). The addition of AC-S measured a_p increased the uncertainty between the measurements. The large uncertainty in the measured a_p would be propagated through to model development and model-derived products would carry that uncertainty.

The OD_f measured by the IS method was almost 50% greater than the OD_f measured by the T method. OD_f from both methods exhibited high correlation at each of the OC wavelengths. The measurement uncertainty for these methods ranged from 0.061% at 412 nm to 63.55% at 670 nm, comparable range of uncertainty of a_p derived from these methods. The maximum uncertainty of a_p was not increased nor decreased by the inclusion of β. This work points to the sensitivity of the parameterization of β, suggesting that more work needs to be done in this area.

Output from the a_p model performed best when compared to a_p computed from the T method, particularly Bricaud and Stramski (1990), the analytical and computational technique from which it was developed. However, most of the methods compared well with the model in the Coastal Water samples at 670 nm even though the model was not optimized for the coastal regime. In general, a_p derived from both QFT and the AC-S, compared good to poorly with the model output. Empirical models such as this are typically only comparable to the water types and methods used for model development. Development of a bio-optical model or method to model a_p in Case 2 waters would be advantageous.

Data collection and analysis methods change and improve over time as technology advances. Inclusion of raw data in a database, such as SeaBASS (Werdell and Bailey 2005), allows for computational analysis flexibility in the future with technological advances. We now have a general idea of the estimate of the uncertainty of existing a_p data. Ultimately the use of traceable standards could be advantageous for addressing the accuracy of the measurements. Additionally, the assessment of analytical precision may benefit from a round robin-like activity in the future.

Figures Chapter 2

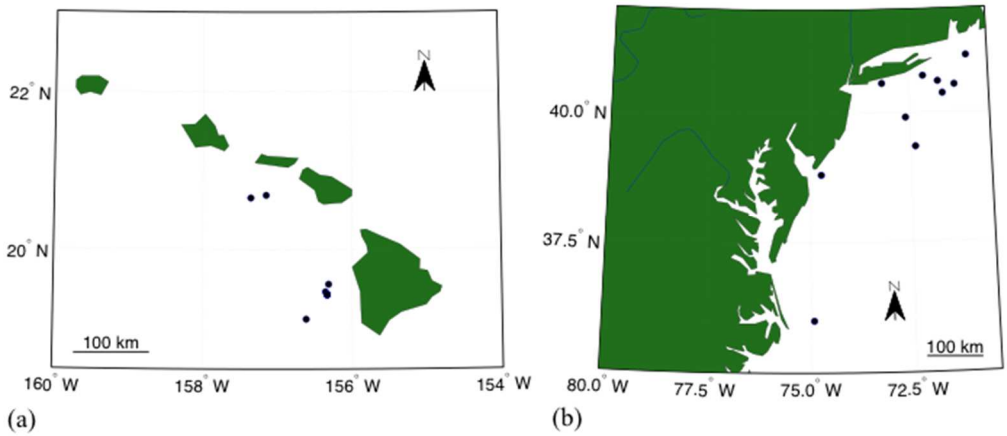

Figure 2.1. Maps showing the locations where the (a) Blue Water samples and (b) Coastal Water samples were collected. The dots represent station locations.

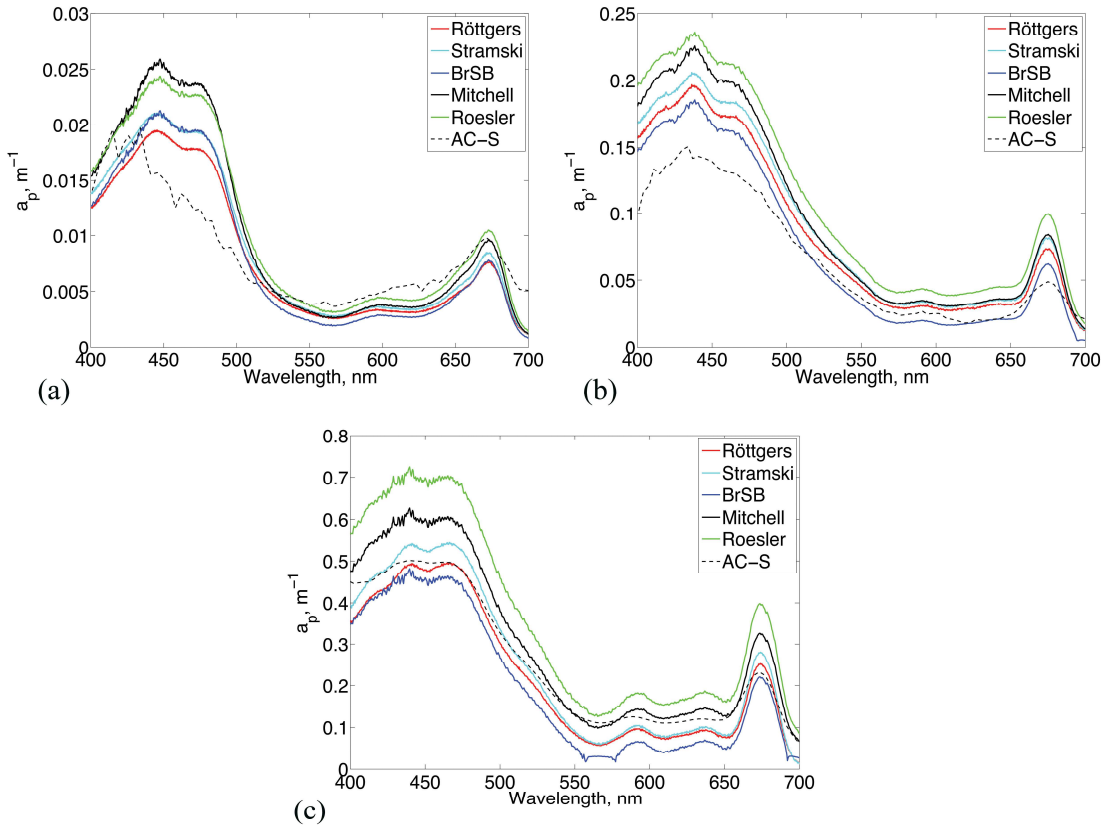

Figure 2.2. Example filter pad and AC-S $a_p(\lambda)$ for (a) Blue Water, (b) Coastal Water, and (c) a culture (*E. huxleyi).* Each computational technique is indicated in the legend.

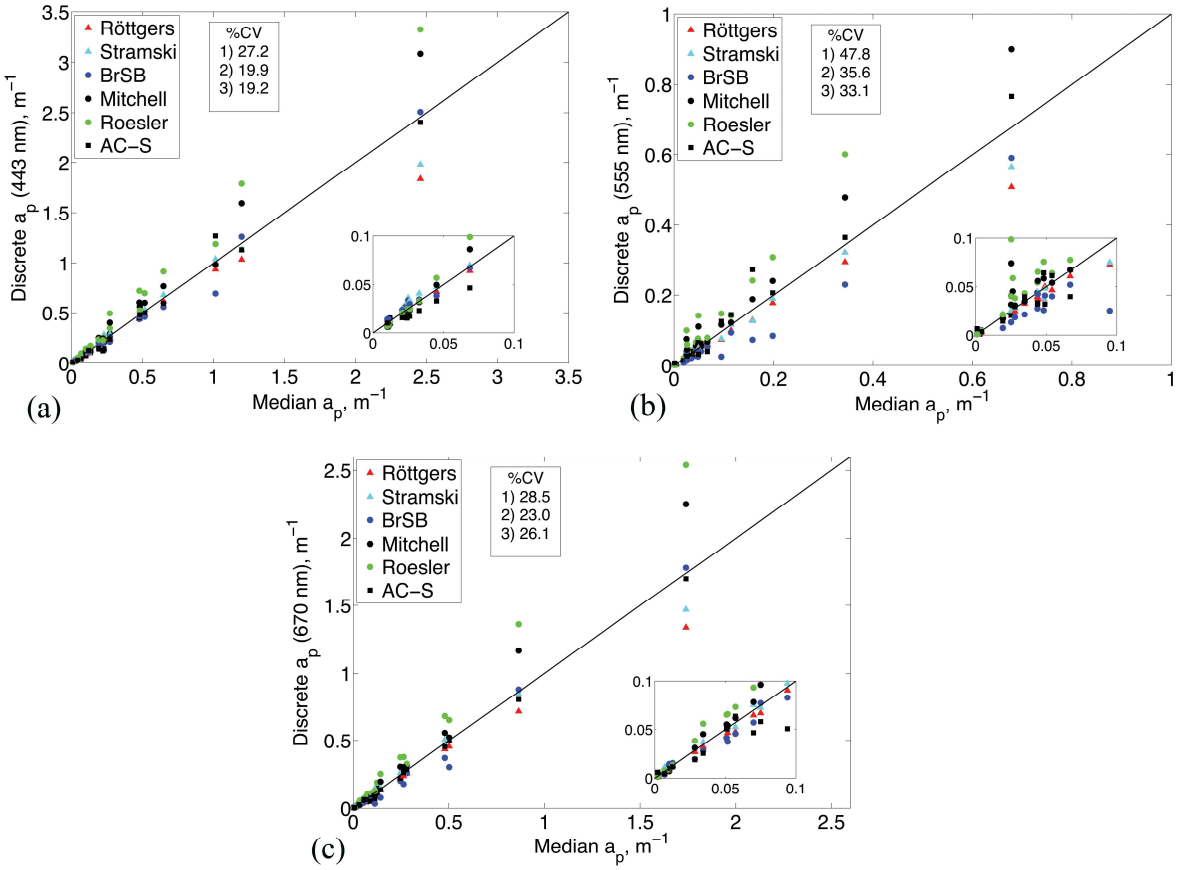

Figure 2.3. QFT and AC-S a_p vs. median a_p for (a) 443 nm, (b) 555 nm, and (c) 670 nm as shown in the legend. The inset figure shows greater detail at the low end of the dynamic range. Text box indicates %CV for the three absorption ranges from Table 2.8.

Tables Chapter 2

Table 2.1. Three instrument configurations for measuring filter pad a_p. Reference to β refers to a pathlength amplification correction factor used in the calculation of a_p.

	Transmittance Method	**Transmittance-Reflectance Method**	**Inside Sphere Method**
Filter placement	In front of detector window	Outside sphere	Inside sphere
Scattering error	Highest	Low	Lowest
Null correction	Between 750 & 800 nm (flat spectra)	None unless values are negative	None
β	Quadratic or Power function, 12 sets of coefficients	Quadratic function, one set coefficients	Quadratic or Power function, 2 sets of coefficients

Table 2.2. Station number and depth at which AC-S and filter pad samples were collected concurrently.

Water type	Station number	Depth (m)	QFT	AC-S
Blue Water	1	90	X	
Blue Water	1	3	X	
Blue Water	2	8	X	X
Blue Water	3	91	X	X
Blue Water	4	135	X	X
Blue Water	5	139	X	
Blue Water	6	124	X	X
Blue Water	7	129	X	X
Blue Water	8	3	X	X
Blue Water	8	135	X	X
Blue Water	9	4	X	X
Blue Water	9	119	X	X
Coastal Water	2	18	X	X
Coastal Water	8	63	X	X
Coastal Water	10	15	X	X
Coastal Water	10	41	X	
Coastal Water	11	20	X	X
Coastal Water	23	22	X	X
Coastal Water	40	32	X	X
Coastal Water	44	10	X	X
Coastal Water	54	7	X	X
Coastal Water	62	17	X	X
Coastal Water	65	16	X	X
Coastal Water	67	32	X	

Table 2.3. Equations used to compute β values in this analysis.

T Method	Equation	Abbreviation	Reference
Mitchell (1990)	$[0.392+0.655OD_f]^{-1}$	Mitchell	15
Roesler (1998)	2	Roesler	22
Bricaud and Stramski (1990)	$1.630OD_f^{-0.22}$	BrSB	21
IS method			
Stramski et al. (2015)	$3.096OD_f^{-0.0867}$	Stramski	27
Röttgers and Gehnke (2012)	$6.475OD_f^2-6.474OD_f+4.765$	Röttgers	26

Table 2.4. Minimum, maximum, mean, median %CV, mean bias and mean ratio of all filter pad OD_f at each OC wavelength. The Pearson's Linear Correlation Coefficient (r) analysis was applied to assess the relationship of OD_f measured by both methods at each ocean color (OC) wavelength depending on particle concentration and sample type. The corrcoeff function in MATLAB 2014a was used for this analysis [45]. The OD_f values from both methods showed a significant ($p<0.05$), positive correlation at 412 nm (r = 0.8673), 443 nm (r = 0.8510), 490 nm (r = 0.8491), 510 nm (r = 0.9062), 555 nm (r = 0.9433) and 670 nm (r = 0.9014).

Wavelength	412 nm	443 nm	490 nm	510 nm	555 nm	670 nm
Min	0.061	0.270	0.384	2.493	0.531	7.477
Max	52.64	56.71	58.14	45.22	60.52	63.55
Mean	21.70	22.01	23.39	23.36	24.14	25.66
Median	21.38	21.72	22.67	23.78	22.43	24.16
Mean bias	-0.030	-0.030	-0.024	-0.018	-0.009	-0.017
Mean ratio	0.804	0.802	0.790	0.782	0.798	0.763

Table 2.5. Minimum, maximum, mean and median %CV of the QFT derived a_p at each OC wavelength.

Wavelength	412 nm	443 nm	490 nm	510 nm	555 nm	670 nm
Min	7.32	7.07	7.72	9.34	14.26	9.00
Max	38.20	36.57	38.52	45.68	62.55	41.52
Mean	18.34	17.96	19.87	22.50	30.46	22.95
Median	17.91	17.24	19.10	21.54	26.49	23.28

Table 2.6. Absorption range, mean absorption and %CV of the QFT derived a_p at four OC wavelengths.

Range a_p	CV 412 nm	Mean a_p 412 nm	CV 443 nm	Mean a_p 443 nm	CV 555 nm	Mean a_p 555 nm	CV 670 nm	Mean a_p 670 nm
0-0.015	25.9	0.011±0.002	25.6	0.010±0.001	25.4	0.004±0.004	23.4	0.008±0.004
0.015-0.05	14.1	0.034±0.021	16.6	0.034±0.016	35.6	0.047±0.020	20.2	0.060±0.022
>0.05	17.8	1.480±2.303	16.9	1.540±2.405	31.6	0.676±0.843	23.8	1.424±2.001

Table 2.7. Minimum, maximum, mean and median %CV of the QFT and AC-S derived a_p at each OC wavelength.

Wavelength	412 nm	443 nm	490 nm	510 nm	555 nm	670 nm
Min	7.48	7.72	7.99	9.09	14.54	10.12
Max	38.80	30.01	39.60	53.52	119.0	61.38
Mean	20.94	20.31	23.67	26.82	39.23	26.07
Median	20.36	19.56	23.62	25.08	34.24	24.07

Table 2.8. Absorption range, mean absorption and %CV of the QFT and AC-S derived a_p at four OC wavelengths.

Range a_p	CV 412 nm	Mean a_p 412 nm	CV 443 nm	Mean a_p 443 nm	CV 555 nm	Mean a_p 555 nm	CV 670 nm	Mean a_p 670 nm
0-0.015	33.2	0.010±0.001	27.2	0.011±0.001	47.8	0.002±0.001	28.5	0.008±0.004
0.015-0.05	16.6	0.032±0.022	19.9	0.034±0.017	35.6	0.046±0.021	23.0	0.058±0.021
>0.05	20.8	0.502±0.591	19.2	0.531±0.616	33.1	0.322±0.254	26.1	0.501±0.536

Table 2.9. Skill Score computed for modeled a_p at 443 nm. **Bold** values indicate "very good" performance and *italicized* values indicate "poor" performance.

	Blue Water				Coastal Water			
Method	N	SS	RMSE	CV	N	SS	RMSE	CV
BrSB	13	**0.7684**	0.0019	5.8±4.1	11	0.1816	0.0524	30.7±20.7
Mitchell	13	0.5575	0.0044	12.3±6.5	11	*-0.0406*	0.0804	45.0±18.8
Roesler	13	0.6072	0.0031	12.0±8.4	11	*-0.1557*	0.0822	48.5±18.5
Röttgers	13	0.3570	0.0052	17.0±13.6	11	0.1824	0.0537	31.3±21.4
Stramski	13	0.4275	0.0047	13.3±12.2	11	*-0.0604*	0.1329	34.7±21.2
AC-S	9	*-0.4145*	0.0071	66.7±32.0	10	0.4247	0.0289	32.2±33.6

Table 2.10. Skill Score computed for modeled a_p at 555 nm. **Bold** values indicate "very good" performance and *italicized* values indicate "poor" performance.

	Blue Water				Coastal Water			
Method	N	SS	RMSE	CV	N	SS	RMSE	CV
BrSB	13	*-0.7967*	0.0017	43.3±10.7	11	0.3629	0.0102	30.9±27.6
Mitchell	13	0.2306	0.0009	16.2±6.3	11	*-0.0276*	0.0199	49.3±26.8
Roesler	13	0.6145	0.0005	10.3±6.0	11	*-0.2264*	0.0273	59.0±27.5
Röttgers	13	*-0.4030*	0.0014	26.8±16.6	11	*0.0089*	0.0158	44.6±29.9
Stramski	13	*-0.3708*	0.0012	22.9±16.6	11	*-0.0834*	0.0191	49.3±29.3
AC-S	9	*-0.1158*	0.0032	43.7±27.0	9	0.5715	0.0167	24.7±22.6

Table 2.11. Skill Score computed for modeled a_p at 670 nm. **Bold** values indicate "very good" performance and *italicized* values indicate "poor" performance.

	Blue Water				Coastal Water			
Method	N	SS	RMSE	CV	N	SS	RMSE	CV
BrSB	13	**0.7626**	0.0009	15.6±12.4	11	0.5826	0.0114	12.3±11.3
Mitchell	13	0.4927	0.0023	15.2±8.0	11	0.2608	0.0244	32.3±12.8
Roesler	13	0.3749	0.0029	22.2±6.0	11	*0.0869*	0.0331	43.2±13.4
Röttgers	13	0.6313	0.0014	13.3±10.6	11	0.4474	0.0144	23.2±22.0
Stramski	13	0.5910	0.0015	13.3±8.6	11	0.3382	0.0187	29.0±21.5
AC-S	9	0.6114	0.0022	30.2±15.5	10	0.4879	0.0102	14.6±14.5

Table 2.12. Summary of ocean color bands and their primary use.

Wavelength (nm)	Derived information
412	Dissolved organic matter
443	Chlorophyll absorption
490	Pigment absorption
510	Chlorophyll absorption
555	Pigments, sediments
670	Atmospheric correction, sediments

Chapter 3: Unraveling Phytoplankton Community Dynamics in the Northern Chukchi Sea under Sea-Ice-Covered and Sea-Ice-Free Conditions

3.1 Introduction

In the Arctic Ocean, seasonal sea ice cover shapes the ecosystem structure of the water column by influencing light, nutrients and density-driven stratification. In turn, ecosystem structure shapes pelagic phytoplankton community composition and spatial distribution under both sea-ice-cover and sea-ice-free conditions. Sea ice extent in the Arctic Ocean is declining rapidly, leading to predictions that the Arctic will be sea-ice-free in the summer as early as 2040 (Overland and Wang 2013). Enhanced stratification from freshwater input and warming is expected to limit the advection of nutrients into the euphotic zone of ice-free regions (Tremblay et al. 2008, Mathis et al. 2014). The expected consequences of ice-free summers are longer open water duration and an extended growth season for pelagic phytoplankton. While recent work has focused on our still needed understanding of sea ice algae dynamics (Selz et al. 2017), it is also timely to consider how phytoplankton communities will respond to longer periods of seasonally open water.

Under sea-ice-free conditions, water column structure (stratification or vertical mixing) across the Chukchi Sea (Figure 1.1) is influenced by a number of factors, including inflow of Pacific water to the Arctic Ocean (Mathis et al., 2014), vertical mixing through wind events (Nishino et al. 2015) and upwelling (e.g., Barrow Canyon (Hill and Cota 2005, Grebmeier et al. 2015), and the presence of nutrient rich Winter Water (Woodgate et al. 2005b, Lowry et al. 2015). Vertical mixing events can influence the magnitude of primary production in the Arctic by replenishing nutrients

to the euphotic zone, thereby creating an environment favorable to larger phytoplankton such as chain-forming diatoms (Carmack 2007, Ardyna et al. 2011). In contrast, stratification limits mixing, creating nutrient-depleted conditions that favor a community of smaller, less productive phytoplankton that exhibit lower nutrient requirements, e.g., cyanobacteria and pico-eukaryotes (Lee et al. 2007, Li et al. 2009). Recent studies have focused on the fate of net primary production (Arrigo and van Dijken 2015, Hill et al. 2017) and spatial distribution of phytoplankton communities (Tremblay et al. 2009, Ardyna et al. 2011) in response to longer open water duration and nutrient availability. The magnitude of primary production is affected by phytoplankton community composition, where diatoms are responsible for new primary production fueled by replenished new nutrients, while autotrophic picoplankton and nanoflagellate production is supported by regenerated nutrients (Ardyna et al. 2011). Considering that the impact of local processes on the spatial distribution of phytoplankton communities throughout the Chukchi Sea will likely be heterogeneous under scenarios of future climate change, the question of how earlier sea ice retreat and longer ice-free conditions will affect phytoplankton production is difficult to answer.

Gaining an enhanced understanding of the mechanisms that drive the relationship between the environment and phytoplankton community composition under sea-ice-covered and sea-ice-free conditions is important to understand the implications of longer open water duration, increased stratification and warmer sea surface temperature (SST) that will change the ecological niches that define the habitats to which the phytoplankton are adapted. To address the question of how

phytoplankton will respond to a 'new Arctic' system that describes the potential for an ice-free summer (Overpeck et al. 2005), we must first characterize phytoplankton communities in their current habitats of sea-ice-covered and sea-ice-free waters.

Margalef's mandala is a conceptual model of phytoplankton succession that describes mechanisms by which nutrients and turbulence drive phytoplankton dynamics (Margalef 1978). Within this framework, smaller phytoplankton dominate in calm, low nutrient environments while larger phytoplankton succeed in areas of higher turbulence and greater nutrient concentrations. Since its inception, this model has been updated so that it may be applied to more complex ecosystems, such as that of harmful algal blooms (Glibert 2016). As with Margalef's mandala, when we understand the underlying mechanisms that influence the ecological niches of Arctic phytoplankton under sea-ice-covered and sea-ice-free conditions, we may be able to predict responses of the phytoplankton communities to changes in the Arctic environment thereby creating a new model for that ecosystem.

A number of synthesis papers have recently emerged using data collected during the the NASA-funded **I**mpacts of **C**limate on **E**co**S**ystems and **C**hemistry of the **A**rctic **P**acific **E**nvironment (ICECAPE) field campaigns that took place in 2010 and 2011 (Arrigo 2015). One such study characterized the ecologcial drivers of the sea-ice algae community (Selz et al., 2017). Another important study characterized phytoplankton community composition of an under-ice bloom during the 2011 field campaign but did not provide a detailed discussion of the ecological drivers that shape the communities (Laney and Sosik 2014, Selz et al. 2017). Here we present a parallel study applying similar approaches to that of Selz et al. (2017) to compare

phytoplankton communites present in two different systems: sea-ice-free and sea-ice-covered. Using data collected in the summer of 2011, our goals in this study were two-fold: (1) characterize phytoplankton communities and abundances across the northern Chukchi Self and western Beaufort Sea and (2) determine which environmental drivers influence phytoplankton assemblages. Studies such as these are particularly timely in light of substantial changes in sea ice cover discussed earlier in this paper.

3.2 Materials and methods

3.2.1 Study Site

Environmental and phytoplankton taxonomic data were collected as part of the NASA funded **I**mpacts of **C**limate on **E**co**S**ystems and **C**hemistry of the **A**rctic **P**acific **E**nvironment (ICECAPE) field campaign on the United States Coast Guard Cutter Healy. The phytoplankton taxa and environmental parameters used in this study with their abbreviations are listed in Tables S1 and S2. Here we focus on a subset of the samples (n=380; 81 stations) collected during the summer season between July 2nd and July 24th, 2011 in the northern Chukchi and western Beaufort Seas (Figure 3.1).

3.2.2 Sample collection and analysis

Water column profiles were collected using a rosette equipped with a Sea-bird Electronics conductivity-temperature-depth sensor package (SBE 911+, Sea-bird Electronics): a SBE9Plus CTD with dual pumps and dual temperature (SBE3plus), dual conductivity (SBE4C) sensors. Additional instruments included a Chelsea

Technologies fluorometer (AQIII) and a Biospherical Instruments (QSP2300) Photosynthetically Active Radiation (PAR) sensor. Samples were collected for analysis of nutrients, phytoplankton taxonomy and Chlorophyll *a* (Chl*a*) at discrete depths of just below the surface, 10, 25, 50, 100, 150, and 200 m (depending on total water depth) and at the Chl*a* maximum using a rosette of twelve, 30-liter Niskin bottles. Nitrate (NO_3^-), Nitrite (NO_2^-) and Silicate (Si) concentrations were determined using a modification of the method of Armstrong et al. (1967). Ammonium (NH_4^+) concentrations were measured fluorometrically (Kérouel and Aminot 1997). Phosphate (P) concentrations were measured following the Bernhardt and Wilhelms (1967) method. Chl*a* was determined using high performance liquid chromatography (Van Heukelem and Thomas 2001, Hooker et al. 2005). Subsurface PAR (Light) was calculated as a fraction of the incoming surface PAR at each discrete sampling depth. Simulated-in-situ net primary productivity was measured using shipboard, 24-hour ^{14}C-bicarbonate incubations (Arrigo et al. 2014).

Phytoplankton taxonomy data (Table S1) were collected at each station using an Imaging FlowCytobot (IFCB) that collects images of particles greater than ~ 8 µm (Olson and Sosik 2007). A Beckman-Coulter Accuri C6 flow cytometer was used to enumerate particles between 2–14 µm (Laney and Sosik 2014) Phytoplankton biovolume was calculated using the method of Moberg and Sosik (2012). Phytoplankton carbon biomass from each taxon was estimated using the method of Menden-Deuer and Lessard (2000). It is important to note that the data are classified to the rank of genus or size class.

Sea ice cover and extent were determined at 6.25-kilometer resolution using data collected by the Advanced Microwave Scanning Radiometer for the Earth Observing System (AMSR-E) on the earth-observing satellite platform Aqua (Spreen et al. 2008). Timing of sea ice break-up was determined based on a sea ice concentration threshold of 15% (Frey et al. 2015). The sea ice index or 'ICE presence', similar to that of Lowry et al. (2015), was defined as the number of days since sea-ice breakup, where positive values represent locations still covered in ice and negative values represent locations no longer covered with sea ice.

3.2.3 Statistics

To address our goals, we applied three multivariate statistical techniques, Cluster Analysis (CA), Principle Component Analysis (PCA), and Canonical Correspondence Analysis (CCA) to the phytoplankton taxonomic composition data and environmental variables (Supporting information Tables A1.S1 & A1.S2, respectively) collected in the northern Chukchi and western Beaufort Seas (Figure 3.1). CA was applied to the phytoplankton data to group the taxa based on similar distribution and abundance patterns. CCA was applied to the taxonomic and environmental data to explain possible relationships between phytoplankton community composition and the environmental parameters (Ter Braak and Verdonschot 1995). PCA was applied to the environmental data to elucidate distributional patterns across the study site. We also considered community richness in the samples (the count of phytoplankton taxa). From these analyses, we evaluated how water column properties under sea-ice-covered and sea-ice-free conditions impacted phytoplankton community composition. CA was performed using Primer-E

version 7 software, a Bray-Curtis distance matrix and Group Average Linkage. Prior to CA, the phytoplankton data were transformed by dividing the value within each variable column (phytoplankton taxon) by the sum of the values. PCA and CCA were performed using the statistical software package Canoco Version 5. Because PCA gives more weight to variables with higher variances, the environmental variables were both centered and standardized so that the mean was equal to zero and the standard deviation was equal to one (Z scores). PCA was based on the correlation matrix. PCs were not rotated because the results were interpretable. CCA and CA were applied to the derived carbon abundances. For CCA, taxonomic carbon data were log transformed (log(X+1)) to reduce the bias associated with extreme values, the environmental variables were centered and standardized, and rare taxa were downweighted within Canoco. Because some of the environmental variables could be highly correlated, we also performed an interactive stepwise selection method in Canoco, which performs CCA on each variable separately and determines whether the fit of the variable is significant to $p<0.05$ (with Bonferroni correction).

3.3 Results and discussion

3.3.1 Phytoplankton community structure by CCA

In this study, we wanted to characterize the spatial variability and underlying patterns of the environmental variables across the study region by applying multivariate statistical analyses to the environmental and phytoplankton community composition data. We aimed to group the phytoplankton based on presence and abundance and define possible relationships between the environmental parameters and the phytoplankton community composition.

CA separated the taxa into four clusters (Figure 3.2). The first cluster included three diatom taxa, *Coscinodiscus*, *Odontella* and *Thalassionema*, which were observed in <1.6% of all samples in this study. Because this cluster contributed a small percentage to phytoplankton communities in the samples, we consider these rare taxa and, for the sake of brevity, will not discuss them in this study.

The second cluster, Phytoplankton Group A (PGA; 'ice-bloomers') was comprised of six diatom taxa (*Bacteriosira*, *Fragilariopsis*, *Detonula*, *Pleurosigma*, *Nitzschia*, and *Navicula*), a green alga (*Pyramimonas*), and a colonial haptophyte with and without diatoms (*Phaeocystis*). From the CCA biplot (Figure 3.3a), there is a clear distribution of the vectors along the CCA-axis 1, which explains 22.4% if the variation (Supporting information Table A1.S3a). Interactive-forward-CCA revealed that these taxa exhibited a significant, positive relationship ($p<0.05$; Supporting information Table A1.S3b) with the vectors silica (Si; an essential nutrient for diatoms) and 'ICE presence' (Fig. 3a; red symbols). The low turbulence and high nutrient environment (particularly Si; Supporting information Table A1.S4) created by sea ice and meltwater formed eutrophic-like conditions that are favorable for these taxa (Ardyna et al., 2011). Based on historical observations, these taxa are commonly associated with the sea ice edge and under-ice blooms in the Arctic (Selz et al., 2017; von Quillfeldt, 2000; von Quillfeldt et al., 2003). This group also exhibited the highest Chl*a* biomass, second highest carbon abundance and highest median community richness (11 taxa) in samples where PGA was dominant (Supporting information Table A1.S4 and Text A1.S2).

The relationship of sea ice and Si is important to note because Si is regenerated in pack ice or sea-ice brine channels during the winter and released to the ocean surface when sea ice melts (Fripiat et al., 2014; Werner et al., 2007). Using measurements of silica isotopic composition in ice cores collected from first year ice off of Greenland and a time-dependent geochemical single-box model, Fripiat et al. (2014) showed that silica dissolution and regeneration occurs within the brine channels of the sea ice. The dissolution to production ratios of 0.4-0.9 by measuring initial and final values of the heavier silica isotope δ^{30} relative to an analytical quartz standard. The authors suggest that biogenic dissolution of silica is favorable in sea ice because of bacterial hydrolyzing activity that breaks down diatom frustules. Dead diatoms are broken down by the brine or by high pH environment within the sea ice caused by productivity of sea ice algae that may cause silica dissolution. Similar dissolution results were also observed in Antarctic sea ice (Fripiat et al. 2007). In parallel studies to that presented here, Selz et al. (2017) and Laney and Sosik (2014) also found that the under-ice phytoplankton community accumulated in the late spring and was dominated by the same community of diatoms described in this study. Selz et al. (2017) concluded that water column phytoplankton were taxonomically distinct from the ice algae during the under-ice bloom.

The third cluster, Phytoplankton Group B (PGB; Figure 3.2), included six diatom taxa (*Eucampia*, Unclassified Pennates, *Pseudonitzschia*, *Chaetoceros*, *Thalassiosir*a, *Cylindrotheca*), nanophytoplankton, picophytoplankton and unclassified dinoflagellates. PGB exhibited the highest carbon abundance and second highest Chl*a* biomass and median community richness (10 taxa) in samples where

PGB was dominant. Interactive-forward-CCA revealed that these taxa (Figure 3.3a, green symbols), exhibited a significant, positive relationship ($p<0.05$) with density, salinity and depth where DIN and P concentrations were higher (Supporting information Table A1.S4). Like PGA, many of these taxa are commonly associated with spring blooms (Daugbjerg, 2000; Gradinger, 1996; von Quillfeldt, 2000). Brown et al. (2015) observed that during ICESCAPE 2010 and 2011, the SCM formed at least one month prior to sea ice retreat and was seeded by some members of the under-ice phytoplankton bloom (PGA). Once sea ice had fully retreated, the SCM was found at a depth of 15–30 m, deeper than the net primary productivity maximum (Brown et al., 2015). Nano- and picophytoplankton were observed in 99% of the samples, under both sea-ice-covered and sea-ice-free conditions and may be considered cosmopolitan within in this region (Supporting information Text S2).

The fourth cluster, Phytoplankton Group C (PGC; Figure 3.2) or 'oligotrophic-type' taxa included a chrysophyte (*Dinobryon*), four diatom taxa (*Ephemera*, *Leptocylindrus*, *Melosira*, and *Rhizosolenia*), a dinoflagellate (*Polarella*) and a silicoflagellate (*Dictyocha*). Interactive-forward-CCA (Figure 3.3a, orange symbols) revealed that these taxa exhibited a significant, positive relationship ($p<0.05$) with the vectors 'Temp' and 'Light'. This group was also characterized with the lowest mean Chl*a* biomass, carbon abundance and median community richness (3) in samples where PGC was dominant. PGC was observed at sampling sites no longer covered with sea ice, with the exception of *Rhizosolenia*. These taxa represent remnants of sea-ice-presence, such as *Polarella*, found in sea ice and can form cysts (Montresor et al., 2003) and taxa that are typically found in fresher, low-nutrient

conditions, i.e., *Rhizosolenia* (e.g., Villareal, 1990), *Dinobryon* (e.g., Balzano et al., 2012) and *Leptocylindrus* (e.g., Davis et al., 1980). An oligotrophic-type ecosystem (depleted nitrate) was created when the spring under-ice bloom depleted the nutrients in the surface waters supporting lower phytoplankton biomass similar to that described in Ardyna et al. (2011) and Tremblay et al. (2009) for the Canadian High Arctic.

From these analyses we separated the phytoplankton assemblages into four groups. PGA was found as part of the under-ice blooms, in the presence of sea ice and greater Si. PGB dominated the SCM associated with greater DIN and P and was partially seeded by the under-ice phytoplankton community. PGC was found primarily in warm, nutrient-depleted, sea-ice-free waters. Next, we discuss the environmental forcing that shaped the spatial distribution of these groups.

3.3.2 Water column structure explained by PCA

Using PCA, the measured environmental variables (Supporting information Table A1.S2) in samples collected from CTD profiles were grouped based on similar environmental characteristics and, using vectors to represent the environmental parameters, produced an ordination diagram or biplot to illustrate the relationship between the samples and environmental parameters. The direction and length of the vectors determine the direction at which each parameter increased the most and the rate of change of each parameter with the samples. At first glance, we see a clear distribution of the vectors along the PC-axis 2 of the biplot, explaining 48% of the variation (Figure 3.3b), where the magnitude of light and temperature increase in one direction and all other parameters, except 'ICE presence', increase in the opposite

direction. The 'ICE presence' vector explained 21% of the variation in the direction of PC-axis 1. We went a step further to distinguish each sample based on whether they were collected underneath the sea ice (squares) or in open water (circles) and if there was a depth-dependence to the distribution of the samples, where red symbols represent depths shallower than 25 m and blue symbols represent samples collected deeper than 25 m. We found that samples collected at depths shallower than 25 m (red symbols) or in a sea-ice-free location (circles) were associated with higher water temperatures and greater light. Samples collected at depths greater than 25 m (blue symbols) and those collected underneath the ice (squares) were positively associated with nutrients, salinity, density, and depth (PC-axis 2). Density and salinity followed similar patterns as salinity drives stratification in high latitude seas while subtropical seas are stratified by temperature (Carmack, 2007). The parameter 'ICE presence' explained the variability of the sampling sites across the PC-axis 1, where sites collected underneath the ice (squares) are found along the left side of the plot and sites no longer covered by sea ice (circles) were distributed along the right side of the plot. Our inclusion of an index for sea ice presence in the statistical analyses proved to be a necessary explanatory factor to group the samples.

3.3.3 Environmental forcing and phytoplankton spatial distribution

CA and CCA revealed three major phytoplankton groups based on the distributional patterns of the phytoplankton taxa related to nutrients (particularly Si), temperature, light and sea ice. Based on PCA, we concluded that the distributional pattern of the environmental variables was related to both sample depth and sea ice extent. These patterns were evident both vertically in the water column and

horizontally in space. Therefore, the PCA and CCA biplots reflect spatial variations related to sea ice extent. CCA-axis 1 is representative of the effect of time, or the seasonal transition of sea ice cover (negative CCA-axis 1) to open water (positive CCA-axis 1). The CCA-axis 2 dictates the vertical distribution of phytoplankton taxa in the water column in response to nutrient availability. Sea ice extent, and its effect on nutrient availability, SST and stratification, is clearly a major driver of the dynamics of the three phytoplankton groups in this study.

The presence of PGA appears to be driven by the favorable conditions created by sea ice, such as melt water-induced stratification (allows them to stay at the surface to access light) and higher Si and DIN concentrations, indicated by the median ratios of P:Si and DIN:Si (0.041 and 0.339, respectively at under-ice bloom stations 56-101; Laney & Sosik, 2014). Large diatoms, particularly *Bacteriosira*, *Fragilariopsis*, *Detonula*, *Pleurosigma*, and *Navicula* flourish in the high nutrient, low turbulence environment created by the presence of sea ice and melting ice that creates a freshwater lens that keeps the diatoms near the surface. Margalef's original schematic placed large diatoms in the top right-hand corner of the diagram associated with high nutrients and low turbulence. The re-drawn version of the schematic by Balch (2004) includes harmful algal bloom dinoflagellates in the top left-hand corner associated with high nutrients and low turbulence. Since no harmful algal bloom dinoflagellates were observed in this study[3], we can replace this group large diatoms. As open water duration lengthens, the surface ocean warms and become depleted of

[3] Although HAB species were not detected in this study, recent studies have detected *Alexandrium*, a known toxic species further south of this study in the Chukchi Sea beginning in 2013 (Natsuike et al. 2017) and could pose a problem in the Chukchi Sea.

nutrients and the spring bloom ends. PGC is observed in the warmer, nutrient depleted surface ocean as indicated by the median ratios of P:Si and DIN:Si (0.182 and 0.022, respectively). Once nutrients have been depleted in the surface water, PGB forms an SCM deeper in the water column at the 1% light level and where nutrients are more abundant (at top of the nutricline). PGB includes some taxa from the under-ice phytoplankton community already acclimated to low light conditions at depth. The SCM forms in response to depleted nutrients in the upper water column and increased light diffusion to deeper depths.

By characterizing phytoplankton dynamics relative to the presence or absence of sea ice using statistical tools, we have uncovered feedback mechanisms of climate change on critical features of the water column in the Chukchi Sea. Moreover, a new interpretation of Margalef's mandala using the results from this study highlights the continued importance of Margalef's conceptual model in understanding environmental drivers on phytoplankton communities.

3.3.4 Feedbacks of climate change

Using the output of these analyses, we can begin to elicit the implications of earlier sea ice retreat, thinning ice, reduction of sea ice extent and their feedbacks of warmer SST and enhanced stratification in this system. Through our knowledge of ecosystem function and the structure of phytoplankton communities, we can make a prediction about how the three phytoplankton groups revealed in this study will behave in the future northern Chukchi and western Beaufort Seas and make inferences regarding the transfer pathways of phytoplankton carbon. Based on the current trajectory of Arctic climatology, we expect to see a lengthening of open water

duration where PGC will be favored for a longer period than PGA and PGB. The fate of phytoplankton carbon will be determined by the productivity rates and total biomass of each phytoplankton group present in the system.

Within our current framework of understanding, an ecosystem characterized by low chlorophyll and carbon biomass and depleted nutrients will subsist on regenerated production while an ecosystem dominated by large diatoms and replete with nutrients represents new production (Hill et al., 2005). With the new analyses, the biomass of PGC will be lower than the diatom-rich groups PGB and PGC. We expect to see lower net primary productivity rates of PGC resembling those observed in the summer of 2011, where lower simulated-in-situ net primary productivity (e.g., 0.484 g C m^{-2} day^{-1}) was measured in a region dominated by PGC compared to the region dominated by PGA and PGB (e.g., 6.726 and 1.275 g C m^{-2} day^{-1}). Recent work by Ardyna et al. (2017) characterized shifts from eutrophic to oligotrophic conditions in the Canadian Arctic that were also driven by sea ice cover and nutrient depletion. We believe this study and others mentioned throughout this paper (Ardyna et al., 2011; Hill et al., 2005; Selz et al., 2017) improve our understanding of this ecosystem.

3.4 Conclusions

The objective of this study was to uncover the underlying mechanisms that drive phytoplankton community richness and spatial patterns in the northern Chukchi and western Beaufort Seas comparing rare data collected during a single field campaign in sea-ice-cover and sea-ice-free conditions. We went beyond Chl*a* to consider carbon quantity and phytoplankton phenotypes by including phytoplankton

taxonomic data in the analyses. It is important to emphasize the paucity of high-resolution phytoplankton community data in this region with coincident measurements of hydrochemistry, making this is a unique data set. We confirmed that phytoplankton community structure was driven by stratification, nutrients and light. We identified three major phytoplankton groups related to environmental variables in the Chukchi Sea. This study identifies a group of phytoplankton, PGC, typical of open water that adds to previously published identification of communities more likely to be found in sea ice PGA and PGB.

Longer open water duration and lower phytoplankton carbon biomass could have implications for the upper trophic level consumers of the food web that rely on phytoplankton carbon for food. A shift in food web dynamics related to changes in phytoplankton community composition is likely to impact both food quantity and quality, comparable to those observed in the northern Bering Sea (Grebmeier et al. 2006b) and western Antarctic Peninsula where the phytoplankton community has shifted from mainly large diatoms to picophytoplankton and nanoflagellates (Moline et al. 2004, Montes-Hugo et al. 2009, Smith et al. 2012). Notably, we applied a sea ice index that served as a proxy for the seasonality that controls phytoplankton life strategies in this region. Our hope is that the results from this study will assist the community in generating accurate models of phytoplankton community composition in the global ocean in response to climate change.

Figures Chapter 3

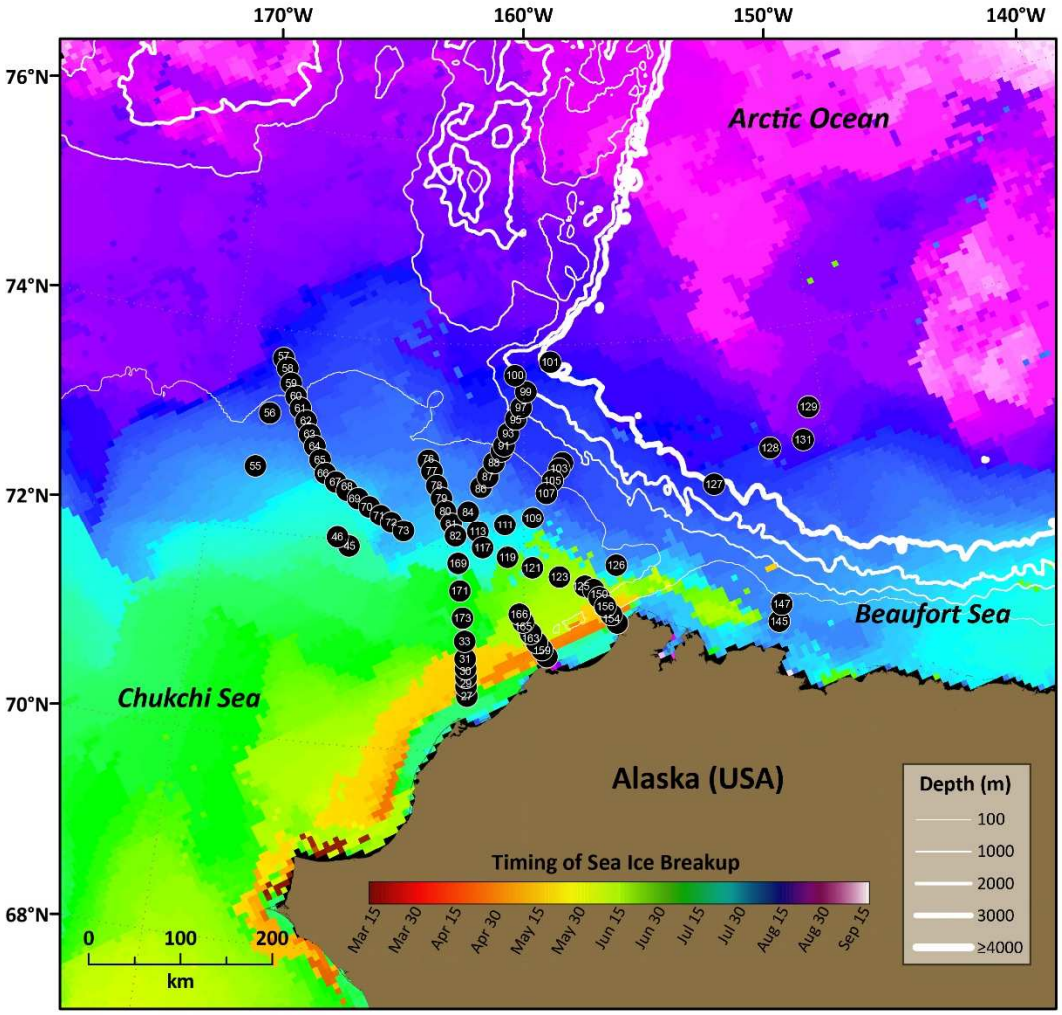

Figure 3.1. Map of ICESCAPE 2011 sampling sites. Location of each sampling site has been superimposed on the bathymetry (white lines) and timing of sea ice breakup (colors). Each pixel represents the day of breakup during the study period in 2011 determined from the timing of when AMSR-E sea ice concentrations fall below a threshold of 15%.

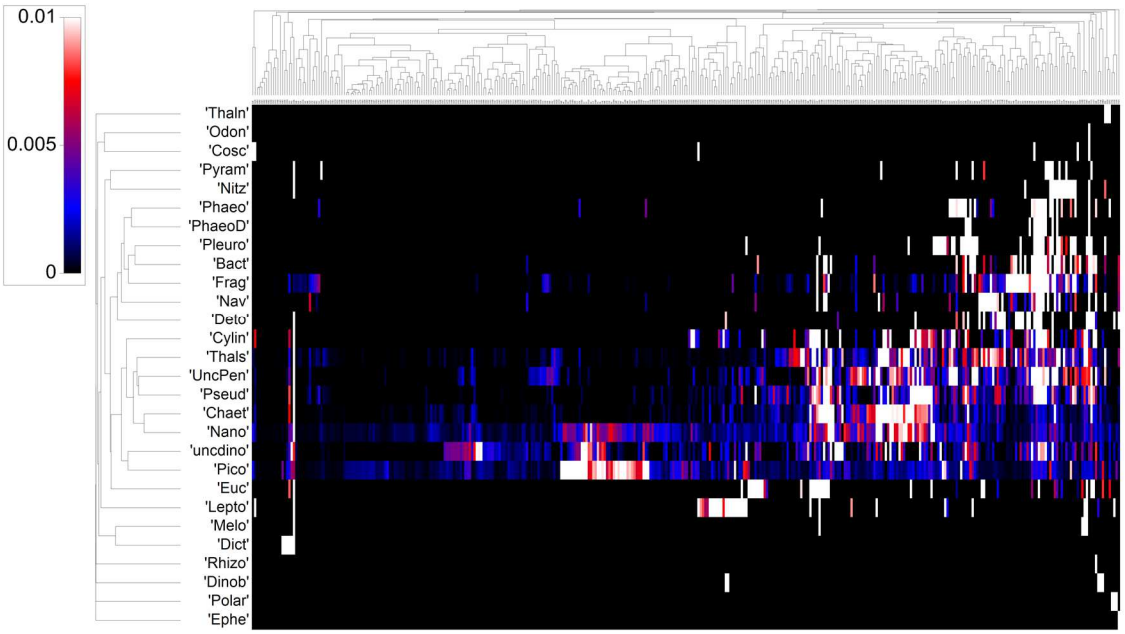

Figure 3.2. CA generated four clusters (y-axis dendrogram): Rare taxa, PGA, PGB and PGC. Within in the heatmap, warmer colors (red to white) and cooler colors (blue to black) represent the relative greater presence or lower presence of a taxon, respectively. The x-axis dendrogram represents sample clusters.

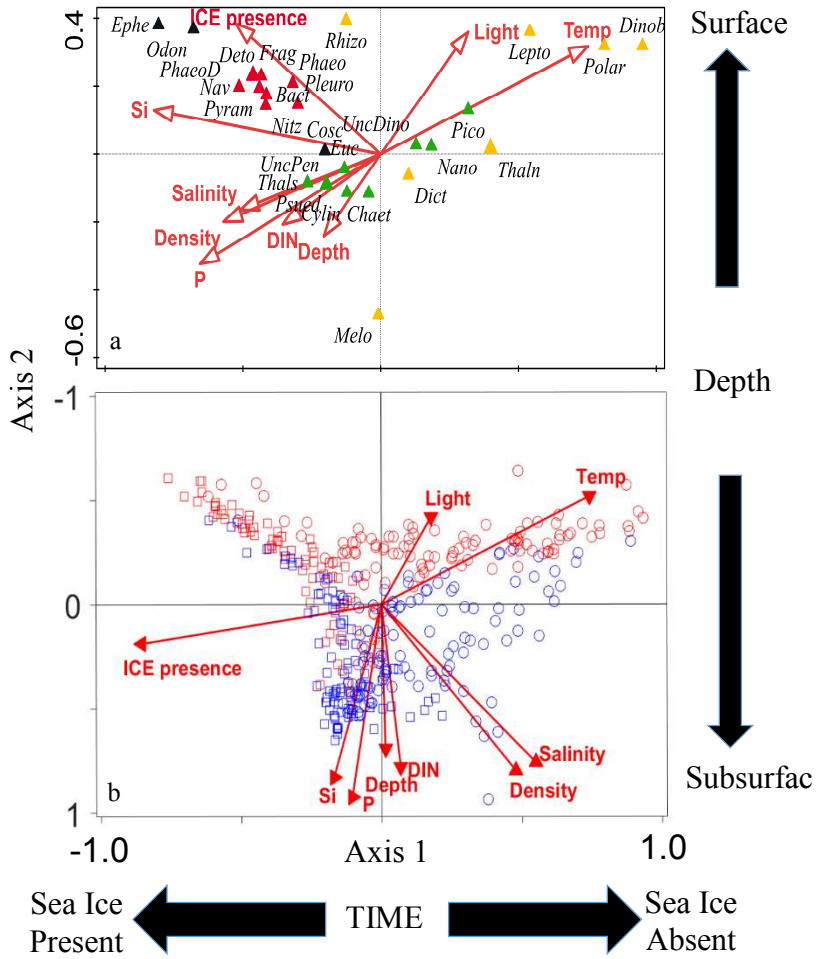

Figure 3.3. (a) The CCA biplot shows the relationships between observed phytoplankton taxa and the environmental variables where black triangles represent rare taxa, red triangles represent PGA, green triangles represent PGB and orange triangles represent PGC as determined from CA. (b) The PCA biplot shows the relationship between samples and the environmental variables where red squares represent samples collected at depths shallower than 25 m near the ice edge or underneath the ice, blue squares represent samples collected at depths deeper than 25 m near the ice edge or underneath the sea ice, blue circles represent samples collected at depths deeper than 25 m in a location no longer covered by sea ice, and red circles represent samples collected at depths shallower than 25 m in a location no longer covered by sea ice. Axes were flipped to match the CCA biplot.

Chapter 4: The brightest signal of climate change: An application of remote sensing reflectance to assess ecosystem status in the Chukchi Sea

4.1 Introduction

Marine ecosystem status is defined by its dynamics, (e.g., seasonal cycles and long-term variability), its living and non-living constituents (both physical and chemical) and how all of the constituents interact with one another in conjunction with any inherent variability (Constable et al. 2016). The impacts of climate change are currently being felt on Earth as a consequence of human activities (IPCC 2018). For example, large-scale coral bleaching and die-offs have been caused by rising ocean temperatures (Baker et al. 2008). Harmful algal blooms of toxic phytoplankton are on the rise correlated with nutrient loads into coastal environments and rising temperatures (Wheeling 2019). Given the sensitivity of our ocean ecosystems to these changes in global temperature, elucidating ecosystem variability from ecosystem change will assist us in evaluating the acute and chronic symptoms of large-scale changes in ecosystem status and function, such as changes in habitat, food web structure, organism diversity and energy transfer (Constable et al. 2016).

Significant biological shifts are occurring in the northern Bering Sea and Chukchi Sea owing to enhanced warming and a significant decline in sea ice thickness and persistence (Grebmeier 2012, Moore et al. 2014, Goethel et al. 2019, Grebmeier et al. 2019). Changes in predator-prey interactions are expected with loss of sea ice, as sea ice acts as a platform for apex predators including walrus and sea birds (Blanchard et al. 2017). The loss of sea ice has affected grey whale distributions owing to declines in the amphipod population, a major food source. Foraging

organisms, such as sea ducks and walruses, use the sea ice for resting while foraging for food and consequently are being greatly affected by the declines in sea ice (Grebmeier et al. 2006b). Some benthic organisms, and even Walleye Pollock and Pacific Cod are shifting northward where cooler water temperatures exist (Grebmeier et al. 2018, Eisner 2019). Moreover, for the first-time in reported history, cysts of *Alexandrium*, a known toxic species, have been observed in the Chukchi Sea (Natsuike et al. 2017), in response to the decline of sea ice coupled with an increase in ocean temperatures and sunlight. These are just a few indications that a change in ecosystem status is occurring in the Chukchi Sea.

To monitor many of the aforementioned ecosystem changes, extensive field platforms currently exist in the northern Bering and Chukchi Seas, including the Distributed Biological Observatory (DBO; See Figure 4.1 in Grebmeier et al. (2019)). The purpose of the DBO is to create an internationally coordinated effort of large-scale, standardized shipboard and mooring-based measurements of biological, chemical and physical parameters. Standardized measurements include surveys of benthic organisms and fish, as well as water column measurements of hydrography, nutrients, phytoplankton and zooplankton taxonomy and biomass (Moore and Grebmeier 2018, Moore et al. 2018, Grebmeier et al. 2019). Another tool, ocean color remote sensing, can be used in conjunction with field surveys to further evaluate long-term trends in ecosystem status and to a certain degree supplement data collection when research cruises are not active. Satellite ocean color data has been widely used as a water quality indicator, using derived products such as Chlorophyll a (Chl*a*), a proxy for biomass, and turbidity (Matthews 2011) and to monitor for

changes in ecosystem status and function that may be indicated by changes in phytoplankton biomass (Del Castillo et al. 2019). Ocean color remote sensing reflectances ($R_{rs}(\lambda)$) and satellite derived Chl*a* are both considered Essential Climate Variables (ECV), measures that assist in the characterization of the Earth's climate and contribute to the climate data record. ECVs are critical members of the climate data record, which is defined as a set of continuous measurements that are of a sufficient length of time that they can be used to evaluate climate variability (Groom et al. 2019).

In a recent study, Dutkiewicz et al. (2019) suggested that, $R_{rs}(\lambda)$, defined as the light that exits the water column and is measured by satellite-borne instruments, will provide the earliest and strongest signal of marine ecosystem change because they are not subject to the natural variability and algorithm uncertainties as derived products. Moreover, responses in $R_{rs}(\lambda)$ not only include the signal of Chl*a* but all of the optically active constituents in the water, which include colored dissolved organic matter (CDOM), nonalgal particles, and phytoplankton pigment signatures, all of which influence the light field of the water column (Dutkiewicz et al. 2019).

The Arctic region is warming at least twice the global average rate (Trenberth et al. 2007, Wassmann 2011). Timing of sea ice break up is crucial to the initiation of the spring diatom bloom and subsequent carbon export, a major source of food for the benthic community. Sea ice is an important driver of nutrients, light and stratification and, therefore, its presence or absence influences the diversity and abundance of both sea ice algae and pelagic phytoplankton (Neeley et al. 2018). In response to earlier sea ice breakup, the spring bloom is occurring earlier and phytoplankton growth is

extended over a longer season (Wassmann 2011). Under normal conditions, ice algae and pelagic phytoplankton bloom in early spring with the export of fresh phytoplankton carbon following soon after. With the loss of multiyear sea ice and decline in sea ice extent, longer open water duration is leading to thermal stratification that prevents nutrients from entering the euphotic zone, except during storm and wind events (Wassmann 2011, Nishino et al. 2015). Longer open water duration will also extend the time for exported production to occur (Wassmann 2011). Moreover, the spring bloom is occurring earlier, and the phytoplankton growth season has been extended longer over the summer, spreading the usual large pulse of phytoplankton carbon export over a longer period of time. It is unknown how this new ecosystem status will affect primary producers and the entire food web in the Chukchi Sea in the future, although we are already seeing its effects.

Considering the ecosystem changes observed in the Chukchi Sea, it is essential that all tools available for evaluating long term trends in ecosystem status are exploited, including ocean color remote sensing. Here, we present the application of a new algorithm, the Apparent Visible Wavelength (AVW; (Vandermeulen et al. in Review)), to monthly time series satellite $R_{rs}(\lambda)$ data collected from the Chukchi Sea. The AVW is an algorithm that reduces an integral-normalized $R_{rs}(\lambda)$ spectrum to one number that represents the apparent color of the water. Because AVW is based on the shape of the $R_{rs}(\lambda)$ spectrum, it is representative of all types of absorbing and scattering constituents in the water column, including phytoplankton. The significant trends in AVW and satellite-derived Chl*a* observed in this study will show that ecosystem-level changes are occurring in the Chukchi Sea. The potential

environmental factors that may be driving this change and a preliminary interpretation of the underlying optical-active constituents that are influencing AVW will be discussed.

4.2 Materials and Methods

4.2.1 Satellite data

Level 3 monthly Moderate Resolution Imaging Spectroradiometer-Aqua (MODISA) $R_{rs}(\lambda)$, and Chl*a* data (June-September, 2003-2018, 4-kilometer resolution) were downloaded for the entire Chukchi Sea (-180˚W to -140˚W, 65˚N to 76˚N) from the NASA Ocean Biology Processing Group data webpage[4]. For the sake of continuity, the 2003-2018 time period was chosen because it is inclusive of the entire lifespan of the MODISA mission. AVW was computed for each 4-km pixel using all visible wavelengths (MODISA λ = 412, 443, 469, 488, 531, 547, 555, 645, 667, 678 nm). The standard OCx band ratio algorithm was used to derive Chl*a* (O'Reilly et al. 1998, O'Reilly et al. 2000).

The methods outlined here are those proposed by Vandermeulen et al. (in Review). AVW represents one number in units of nm^{-1} and is indicative of the shape of $R_{rs}(\lambda)$ and represents the apparent color of the water (Vandermeulen et al. In review). AVW was computed as the weighted harmonic mean of Level 3 monthly MODISA $R_{rs}(\lambda)$ using Eq. 8

$$\boldsymbol{AVW} = \frac{\sum_{i=\lambda_1}^{\lambda n} \boldsymbol{R_{rs}(\lambda_i)}}{\sum_{i=\lambda_1}^{\lambda n} \frac{\boldsymbol{R_{rs}(\lambda_i)}}{\boldsymbol{\lambda_i}}} \quad (8)$$

[4] https://oceancolor.gsfc.nasa.gov/l3

where $R_{rs}(\lambda_i)$ is the value of satellite or in situ measured $R_{rs}(\lambda_i)$ at each given wavelength (n=9) of the instrument. The normalized $R_{rs}(\lambda)$ spectra were derived by dividing each value of $R_{rs}(\lambda)$ by the trapezoidal integration of the entire spectrum, thereby removing the magnitude and focusing on the spectral shape. Because the shape of a normalized $R_{rs}(\lambda)$ spectrum is influenced by each of the optically active constituents of the water column, underlying ecosystem alterations could manifest in changes in the signals of absorption and scattering thereby influencing dominant color of the water represented by AVW . Further details regarding this method are provided in Appendix 3.

4.2.2 Spatial statistical analyses

For this study, the Earth Trends Modeler module in the TerrSet Geospatial Monitoring and Modeling software[5] was used to compute statistical trends in AVW, Chl*a*, sea surface temperature (SST) and sea ice concentrations over the study period 2003-2018 in the Chukchi Sea. Satellite data scenes were first imported into TerrSet and converted into rasters using TerrSet's GDAL raster conversion utility. To compute annual trends of AVW, SST, Chl*a* and sea ice concentration for June-September, 2003-2018, the median trend (Theil Sen) analysis method was used. Median trend is a robust, nonparametric technique that is optimal for computing rates of change in noisy data (Hoaglin et al. 1983). To ensure statistical robustness, only pixels that contained data at least 71% of the study period (i.e., 12 out of 16 years) were included in the analyses. Pixels with data covering less than 71% of the time were masked out of the analysis. The Theil Sen method applies a 29% breakdown

[5] https://clarklabs.org

bound or point that limits the number of extreme values that could affect the results of the analysis. This means that extreme data points must occur more than 29% of the time to be included within the analysis. A Mann Kendall significance test was also applied during the time series analyses to test for statistical significance within the trends (Neeti and Eastman 2011). For this study a p value of less than 0.1 ($p<0.1$) was considered significant.

To examine specific locations of interest more closely, the median of normalized AVW, $R_{rs}(\lambda)$, and monthly Chl*a* values were computed for a 5x5 pixel box around 15 locations across the Chukchi Sea for every month and year of the time series. To examine trends within the $R_{rs}(\lambda)$, detrended least squares robust regression (**robustfit** function in MATLAB) was applied to the normalized $R_{rs}(\lambda)$ values at 412, 443, 490, 555 and 670 nm (Vandermeulen et al. in Review).

4.2.3 Ancillary data

Sea ice concentrations were determined at 25-kilometer resolution using data collected by the Special Sensor Microwave Imager (SSM/I) and the special sensor Microwave Imager/Sounder (SSMIS) sensors on the Defense Meteorological Satellite Program satellites (Cavalieri et al. 2011). Level 3 monthly MODIS-Aqua daytime 11µ SST data were downloaded for the entire Chukchi Sea (-180˚W to -140˚W, 65˚N to 76˚N) from the NASA Ocean Biology Processing Group data webpage. A scale factor was applied to convert the SST data to geophysical numbers and additional sea ice masking was performed prior to analysis.

Particulate and dissolved absorption data were collected as part of the NASA funded **I**mpacts of **C**limate on **E**co**S**ystems and **C**hemistry of the **A**rctic **P**acific

Environment (ICECAPE) field campaigns on the United States Coast Guard Cutter Healy that took place in 2010 and 2011 (Arrigo et al. 2014). Discrete water samples (n=49) were collected from the surface during the summer season between June 18 and July 16, 2010 and June 28 and July 24, 2011 in the northern Chukchi and western Beaufort Seas. Filter pad samples were collected by vacuum filtration (~127 mmHg) onto pre-combusted 25 mm Whatman GF/F filters. Samples were placed in HistoPrep tissue capsules, flash frozen in liquid nitrogen and stored at -80° C until analysis. Values of total particulate absorption ($a_p(\lambda)$) and absorption of non-pigmented particles ($a_{nap}(\lambda)$) were derived using the method of Stramski et al. (2015). Phytoplankton absorption ($a_{ph}(\lambda)$,) was determined by the subtraction of $a_{nap}(\lambda)$ from $a_p(\lambda)$. Absorption coefficients of colored dissolved organic matter (aCDOM) was measured at each station using an Ultrapath World Precision liquid waveguide system (Matsuoka et al. 2015). Total absorption in each sample is defined as the sum of $a_g(\lambda)$, $a_{nap}(\lambda)$, and $a_{ph}(\lambda)$. To determine the fractional contribution of each constituent of absorption, $a_g(\lambda)$, $a_{nap}(\lambda)$, and $a_{ph}(\lambda)$ were normalized to the computed total absorption.

Water column profiles of upwelling radiance ($Lu(\lambda)$; $\mu W\ cm^{-2}\ nm^{-1}\ sr^{-1}$) and downwelling irradiance ($Ed(\lambda)$; $\mu W\ cm^{-2}$) were measured with either a Biospherical PRR-800 with a spectral range of 313-875 nm or a Biospherical C-OPS profiling radiometer with 19 spectral bands between 300 and 900 nm following NASA Ocean Optics Protocols (Mueller and Austin 1995). $R_{rs}(\lambda)$ were computed using the methods of Werdell and Bailey (2005). AVW was computed from $R_{rs}(\lambda)$ derived for each station using the previously described method.

Sea ice cover and extent were determined at 6.25-kilometer resolution using data collected by the Advanced Microwave Scanning Radiometer for the Earth Observing System (AMSR-E) on the earth-observing satellite platform Aqua (Spreen et al. 2008). Although the AMSR-E sea ice data are collected at a higher spatial resolution than the SSMIS data that were used for the trend analysis, Frey et al. (2015) showed that both data sets are similar in this region. Timing of sea ice break-up was determined based on a sea ice concentration threshold of 15% (Frey et al. 2015). The sea ice index was defined as the number of days since sea-ice breakup, where negative values represent locations still covered in ice and positive values represent locations no longer covered with sea ice (Neeley et al. 2018).

Principal Component Analysis (PCA) was applied to the fractionated absorption, AVW, bottom depth and a sea ice index. PCA was performed using the statistical software package Canoco Version 5. Because PCA gives more weight to variables with higher variances, the environmental variables were both centered and standardized so that the mean was equal to zero and the standard deviation was equal to one (Z scores). PCA was based on the correlation matrix. PCs were not rotated because the results were interpretable. When interpreting PCA biplots, the direction and length of the vectors determine the direction at which each parameter increased the most and the rate of change of each parameter with the samples.

To further explore which optically-active constituents, CDOM, nonalgal particles or phytoplankton, could be driving the observed trends in AVW, principal component analysis (PCA) was applied to /the proportion of CDOM (a_g), nonalgal particles (a_{nap}), and phytoplankton (a_{ph}) to total nonwater absorption measured at the

surface during two field campaigns, ICESCAPE 2010 and 2011. Radiometric profiles coincident with absorption measurements were converted to AVW values and acted as the samples in PCA. Bottom depth, a sea ice index (ICE presence; number of days since sea ice retreated) and Chl*a* were included as additional parameters to further explain the relationship of absorption to AVW. Sea ice presence has been used successfully in previous studies to elucidate relationships between the environment and phytoplankton (Neeley et al., 2018).

4.3 Results

4.3.1 Time series trends in AVW

The AVW algorithm was applied to monthly MODISA $R_{rs}(\lambda)$ data collected in the Chukchi and western Beaufort Seas for June – August, 2003-2018. An example map of AVW and the corresponding integral normalized $R_{rs}(\lambda)$ spectra for the Chukchi Sea observed for September 2018 can be seen in Figure 4.1a and 4.1b, respectively. Note that the colors of each spectrum represent the 'dominant color' or AVW based on the weighted mean of the integral normalized $R_{rs}(\lambda)$.

Median trend analysis of AVW across the Chukchi and western Beaufort Seas for the 2003-2018 period revealed a statistically significant (Mann Kendall significance test, $p<0.1$) positive trend, or red shift, of AVW at a rate of up to 15 nm/decade over a large region of the Chukchi Sea in June, July and September, as indicated by hashed regions in Figures 4.2a, 4.2b and 4.2d. The red shift in AVW is observed mainly in the eastern and central Chukchi Sea in June and both eastern and western portions of the Chukchi Sea in July and September. There was a significant negative trend or blue shift of AVW observed in the southeast the Chukchi Sea and in

the Kotzebue Sound in June at a rate of 5-10 nm/decade (indicated by the blue color in Figure 4.2a). Although there were small areas of the Chukchi Sea that exhibited significant changes of AVW, including a negative trend or blue shift in AVW in the northcentral region of the Chukchi and western Beaufort Sea, the month of August appeared to remain relatively stable over the 16-year time series (Figure 4.2c).

4.3.2 Time series trends in Chl*a*

In the previous sections the significant trends in AVW over much of the Chukchi Sea were described. The next step was to investigate if a parallel trend in Chl*a* that could be correlated with the trends in AVW. Median trend analysis was applied to monthly composite images of MODISA Chl*a* in the Chukchi and western Beaufort Seas for June-September, 2003-2018 (Figures 4.3a-4.3d). Overall the same regions that exhibited significant positive and negative trends in AVW also exhibited significant trends ($p<0.1$) in Chl*a* (in units of mg/m^3). June and September displayed significant increase in Chl*a* of $\geq 0.5 mg/m^3$/decade (Figures 4.3a, 4.3d). Interestingly, July showed a significant decrease in Chl*a* (Figure 4.3b) in the same region that exhibited a significant red shift in AVW (Figure 4.2b) over the study period. The southwest region of the Chukchi Sea and Kotzubue Sound that showed the blue shift in AVW within the month of June showed a coincident decrease in Chl*a* at a rate of >0.5 mg/m^3/decade over the study period (Figure 4.3a). Similar to AVW, large-scale significant trends in Chl*a* were not observed in August (Figure 4.3c).

4.3.3 Evaluation of spatio-temporal trends of AVW, $R_{rs}(\lambda)$ and Chl*a* at specific locations

To further investigate the trends in both AVW and Chl*a* described in sections 4.3.1 and 4.3.2, fifteen locations (see Figure 4.1a) were chosen quasi-randomly to demonstrate the spatial variability and underlying shifts in $R_{rs}(\lambda)$ spectral shape, Chl*a* concentration and trends in the individual $R_{rs}(\lambda)$ channels. At each location the median $R_{rs}(\lambda)$ spectra (in units of nm), monthly Chl*a* (in units of mg/m^3) and least squares regression results for five normalized $R_{rs}(\lambda)$ channels (412, 443, 488, 555 667 nm) in units per steradian (Sr^{-1}) per decade were plotted separately for each month of the study. Note that five of the locations were chosen because they were at or near stations where in water samples and measurements were collected during the 2010 and 2011 ICESCAPE field campaigns and, therefore, would be relevant to the interpretation of the results. Three locations (4, 8 and 12; see Figure 4.1a) that exhibited significant trends in AVW, Chl*a* and normalized $R_{rs}(\lambda)$ will be the focus of the following section. However, the figures for all locations are reported in Appendix 2.

Location 4 displayed significant ($p<0.1$), positive trends (red shift) in AVW for June and July 2003-2018 at rates of 7.93 and 8.84 nm/decade, respectively (Figures 4.2a, 4.2c; Tables 4.1, 4.2). Although not significant (p0.1), positive trends in AVW were also observed in August and September 2003-2018 (Figures 4.2b, 4.2d; Tables 4.1c, 4.1d). For June and July, the observed red shift in AVW is clearly observed in the normalized $R_{rs}(\lambda)$ spectral shapes that exhibit a flattening and peak shift from the blue end (shorter wavelengths) to the red end (longer wavelengths) of

the visible spectrum between 2003 and 2018 (Figures 4.4a, 4.4b). August and September exhibited larger variability in the normalized $R_{rs}(\lambda)$ spectra but did not show a clear trend.

Linear regression analysis of the selected five $R_{rs}(\lambda)$ channels corroborated this red shift in $R_{rs}(\lambda)$ spectral shape from June and July 2003-2018, showing significant ($p<0.1$) negative trends in the blue channels of $R_{rs}(412)$, $R_{rs}(443)$ and $R_{rs}(488)$ at rates of $-5.231*10^{-4}$, $-6.094*10^{-4}$ and $-3.597*10^{-4}$/Sr/decade with a coincident significant increase in the green and red channels, $R_{rs}(555)$ and $R_{rs}(670)$ at rates of $4.988*10^{-4}$ and $1.618*10^{-4}$/Sr/decade, respectively (Figure 4.4e; Table 4.5). Locations 2 and 3 exhibited similar trends in AVW and $R_{rs}(\lambda)$ for the months of June and July, with a red shift in AVW and significant, positive trends for $R_{rs}(555)$ and $R_{rs}(670)$ (Figures A2.2, A2.3; Table 4.5). The shifts in spectral shape and trends in the individual $R_{rs}(\lambda)$ manifest in the AVW values, with a general increase in AVW for all four months over the study period (Figure 4.4f).

Location 4 showed a significant, increase in monthly Chl*a* of 0.312 and 0.580 mg/m^3/decade for June and September, respectively, contemporaneous with the trends in AVW and $R_{rs}(\lambda)$ (Figures 4.2a, 4.2d; Tables 4.1, 4.3). Trend analysis also revealed a significant decrease in Chl*a* for July over the 2003-2018 study period at a rate of -0.305 mg/m^3/decade (Table 4.2, Figure 4.2b). Although a slight increase in Chl*a* in 2015 and 2018 was observed, Chl*a* remained fairly low and stable during July (Figure 4.4g). June and, particularly September, exhibited some larger peaks in Chl*a*, particularly 2017 for September (5.5 mg/m^3) and 2014 for June (2.5 mg/m^3). The Chl*a* in September 2017 occurred coincidently with a peak in AVW (Figure 4.4f).

Although not statistically significant ($p>0.1$), August also exhibited a slight increase in Chl*a* over the study period (0.197 mg/m^3/decade). All four months displayed slightly higher Chl*a* concentrations in 2018 compared to 2003 (Tables 4.6-4.9). Locations 2 and 3 also exhibited positive and negative trends in June and July, respectively, with some Chl*a* peaks in June and August (Figures A2.2, A2.3).

Location 8 exhibited a significant ($p<0.1$), red shift in AVW in the months of June and August at rates of 8.46 and 8.52 nm/decade, respectively. Although not statistically significant ($p>0.1$), July and September also showed red shifts in AVW at rates of 6.43 and 2.85 nm/decade, respectively. The normalized spectral shapes for June and August (Figure 4.5a, 4.5c) display a flattening and shift in the spectral peaks to the longer wavelengths or red-end spectrum from the early (2003-2006) to later years (2015-2018) of the study period.

Linear regression analysis of the five $R_{rs}(\lambda)$ channels corroborated the red shift in AVW, exhibiting a significant ($p<0.1$) decrease in normalized $R_{rs}(443)$ and $R_{rs}(488)$ at rates of $4.379*10^{-4}$ and $3.335*10^{-4}$/Sr/decade and significant increases ($p<0.1$) in normalized $R_{rs}(555)$ and $R_{rs}(670)$ at rates of $3.828*10^{-4}$ and $1.728*10^{-4}$/Sr/decade (Figure 4.5e; Table 4.5). Locations 5 and 6 showed similar positive trends in AVW in the month of June at rates of 8.79 and 8.43 nm/decade, respectively (Figures A2.4 and A.5; Table 4.1). Location 6 also exhibited significant, positive trends in $R_{rs}(555)$ and $R_{rs}(670)$ at rates of $1.924*10^{-4}$ and $1.089*10^{-4}$/Sr/decade, respectively (Figure A.5; Table 4.5). Despite large annual variability, particularly in August and September, the shifts in spectral shape and trends in the individual $R_{rs}(\lambda)$

channels manifested in AVW with a general increase over the months of June, August and September over the study period (Figure 4.5f).

Location 8 exhibited an increase in Chl*a* over the 2003-2018 study period in the months of June and August (Figure 4.5g) at rates of 0.358 and 0.599 mg/m^3/decade, respectively (Tables 4.6, 4.8) contemporaneous with the red shift in AVW. Although not significant, July exhibited a negative trend in Chl*a* and September exhibited a positive trend in Chl*a* (Figure 4.5g; Tables 4.7, 4.9). Large peaks in Chl*a* were observed in September, particularly in 2012 and 2017 (~7.5 and 9 mg/m^3, respectively) that occurred coincident with small peaks in AVW (Figure 4.5f). A steady increase over the 16-year period can be observed in the months of June and August, with a peak in August 2017 (~6.5 mg/m^3; Figure 4.5g). Similarly, Location 5 displayed positive trends for Chl*a* in June and September ($p<0.1$) with a peak of Chl*a* in September 2017 (5.5 mg/m^3; Figure A2.4).

Location 12 exhibited significant ($p<0.1$), red shifts in AVW for the months of July and September at rates of 5.92 and 5.8 nm/decade, respectively (Figures 4.6 b, 4.6d; Tables 4.2, 4.4). These rates are similar to that of location 13, which also exhibited red shifts in AVW of 4.67 and 4.02 nm/decade, respectively, during the months July and September (Tables 4.2, 4.4). Although not significant, Location 12 exhibited a negative trend (blue shift) in AVW, similar to Location 10 that exhibited a significant, negative trend in AVW at a rate of 6.96 nm/decade in the month of June (Figure A.8; Table 4.1). The normalized spectral shapes for July and September show a peak shift towards the longer wavelengths (red end) with a concomitant peak flattening (Figures 4.6b, 4.6d). Although the spectral shapes for September are more

variable than in July, the spectra observed in the later years (2015-2017, in red) clearly show the peak shifting to the right (Figure 4.6d).

Linear regression of the of the five R_{rs} channels corroborated the observed shift in spectral shape and AVW, with significant, negative trends in $R_{rs}(412)$ and $R_{rs}(443)$ at rates of $-4.006*10^{-4}$ and $-3.791*10^{-4}$/Sr/decade and significant, positive trends in normalized $R_{rs}(555)$ and $R_{rs}(670)$ at rates of $2.572*10^{-4}$ and $0.802*10^{-4}$/Sr/decade (Figure 4.6e; Table 4.2). These trends are similar to Location 13, which also displayed significant, negative trends in $R_{rs}(412)$ and $R_{rs}(443)$ at rates of $-4.686*10^{-4}$ and $-4.689*10^{-4}$/Sr^{-}/decade and significant, positive trends in normalized $R_{rs}(555)$ and $R_{rs}(670)$ at rates of $2.988*10^{-4}$ and $1.061*10^{-4}*Sr^{-1}*decade^{-1}$ (Figure A2.10; Table 4.2). Location 12 exhibited large peaks in AVW, particularly in September 2010 and June, August and September 2015 (Figure 4.6f). Overall the shifts in spectral shape and trends in the individual $R_{rs}(\lambda)$ channels manifested with a general increase in AVW over the study period, particularly in the months of June and July (Figure 4.6f).

Location 12 exhibited a significant decrease in Chl*a* during the month of July 2003-2018 (Figure 4.6g) at a rate of -0.242 mg/m^3/decade (Table 4.7) contemporaneously with the blue shift in AVW. Although not significant, location 12 did exhibit small, positive trends in August and September (Tables 4.8, 4.9) and a small, negative trend in June at a rate of -0.041 mg/m^3/decade (Table 4.6). Despite particularly large peak in Chl*a* of ~7 mg/m^3 observed in September of 2010 (and not observed in any of the other locations), sizable changes in Chl*a* were not observed at location 12 during the study period (Figure 4.6g). Chl*a* peaks in 2010 and 2015

occurred coincidently with peaks in AVW (Figure 4.6f). Similarly, location 14 also exhibited a significant decrease in Chl*a* at a rate of -0.748 mg/m^3/decade (Table 4.7). Despite this trend, location 14 exhibited peaks in Chl*a* during the month of July in the years 2008 (~2.3 mg/m^3), 2012 (~2.5 mg/m^3), and 2018 (~3 mg/m^3; Figure A2.11).

4.3.4 PCA and absorption

PCA analysis revealed a clear relationship between the three components of non-water absorption and AVW (Figure 4.7). 'Bluer' AVW values (467-488 nm) were associated with a larger proportion of $a_g(\lambda)$ at all wavelengths and deeper bottom depth. Higher values of AVW (>490 nm) were associated with high proportions of absorption by either $a_{ph}(\lambda)$ or $a_{nap}(\lambda)$. Because similar AVW values were associated with both $a_{ph}(\lambda)$ and $a_{nap}(\lambda)$, the addition of Chl*a* and the sea ice index as environmental parameters helped to further explain under what conditions $a_{ph}(\lambda)$ or $a_{nap}(\lambda)$ was dominant. Although the length of the ICE presence vector is small, it did fall in line with the $a_{nap}(375)$ and $a_{nap}(412)$ vectors indicating the greater presence of $a_{nap}(\lambda)$ after sea ice has retreated. On the other hand, the Chl*a* vector followed the same direction as the $a_{ph}(\lambda)$ vectors, indicating that red AVW values were associated with higher phytoplankton abundance.

4.4 Discussion

4.4.1 A redder Chukchi Sea

We applied a new remote sensing tool, the AVW algorithm, to examine trends in ocean color within the Chukchi Sea during the summer months (June-September) of 2003-2018. We observed significant, positive trends in AVW, i.e., a red shift, over

the course of the study in large regions of the Chukchi Sea during the months of June, July and September. The southeast region of the Chukchi Sea exhibited a negative trend, or blue shift, in AVW during the month of June. August exhibited small regions of AVW trends but remained mostly stable over the study period. AVW trends were further investigated by examining the integral-normalized $R_{rs}(\lambda)$ spectral shapes at fifteen locations across the Chukchi Sea to confirm that a coincident red-shift in the spectral shapes supported the observed trends in AVW. Additionally, robust linear regression analysis was performed on five normalized $R_{rs}(\lambda)$ channels (412, 443, 488, 555, and 670 nm) and coincident negative trends in the blue channels (412, 443, and 488 nm) and positive trends in the red and green channels (555 and 670 nm) were observed coincident with a positive trend in AVW was observed. The observed red shift in AVW is supported by the trends in spectral shape and the normalized $R_{rs}(\lambda)$.

4.4.2 Trends in phytoplankton biomass

Next trends in satellite derived Chl*a* were evaluated to determine if coincident trends in phytoplankton biomass could explain the red shift in AVW. Significant trends in Chl*a* were observed within the same regions as the significant AVW trends. June and September showed significant, positive trends in Chl*a*, with Chl*a* increasing $\geq$0.5 mg/m^3/decade. The southeast region of the Chukchi Sea that displayed a blue shift in AVW exhibited a coincident decrease in Chl*a*. Interestingly, despite the positive trend in AVW, July exhibited a negative trend or decrease in Chl*a*. Further examination of monthly Chl*a* at fifteen locations did confirm these observations in the Chl*a* trends despite the annual variability. The positive Chl*a* trends presented in

this study for June and September 2003-2018 are consistent with other field observations in the Chukchi Sea. Nishino et al. (2015) reported high Chl*a* concentrations in May, indicating an early spring bloom, between July 2012 and July 2013. They also captured high Chl*a* (>1mg/m^3) in autumn (August-October) indicating a second, fall phytoplankton bloom.

4.4.3 A disconnect between AVW and Chl*a*

One interesting result from this study showed that AVW and Chl*a* do not always covary. The positive trend in AVW and concomitant negative trend in Chl*a* in July 2003-2018 may be explained by the presence of a subsurface Chl*a* maximum that is prevalent in the Chukchi Sea and occurs coincidently with depleted surface nutrients and a shallow mixed layer depth (Brown et al. 2015, Hill et al. 2018). Note that satellite ocean color instruments can only observe optical properties within the first optical depth, which is determined by the turbidity of the water column. The mixed layer depth has been observed at 12 m or deeper in the Chukchi Sea. Given that field observation-based calculations of the first optical depth ($1/Kd_{490}$) are between 10-11 m on the shelf, it is likely that the turbidity of the surface waters would inhibit the capture of the subsurface Chl*a* from satellite observations.

The uncoupling of AVW and Chl*a* in July indicates that a 'missing link' exists between the red shift in AVW and the negative Chl*a* trend in July. AVW does appear to trend with Chl*a* in some years, but not all. The observed redshift coincident with a decrease in Chl*a* indicates that phytoplankton biomass is not the only factor contributing to AVW trends. It is possible that a higher concentration of nonalgal particles may be the underlying cause of the red shift in AVW when Chl*a* in the

surface water is low. High concentrations of nonalgal particles have been observed in the Chukchi Sea associated with the fall bloom (Nishino et al. 2015). The PCA biplot shows that non-water absorption is a significant driver of AVW, where 'bluer' values of AVW indicate a stronger influence of $a_g(\lambda)$ and 'redder' values indicate a stronger influence of $a_{ph}(\lambda)$ or $a_{nap}(\lambda)$. $a_{ph}(\lambda)$ is more predominant when phytoplankton biomass is high, whereas greater $a_{nap}(\lambda)$ is observed once sea ice has retreated and the phytoplankton biomass declines. $R_{rs}(\lambda)$ is driven by the absorption and backscattering properties of optically active constituents in the water column. Non phytoplankton absorbers, CDOM and nonalgal particles, have been established as strong absorbing components in the Chukchi Sea (Neukermans et al. 2016, Reynolds and Stramski 2019). A positive trend in $R_{rs}(555)$ and $R_{rs}(670)$ with a coincident negative trend in $R_{rs}(412)$ $R_{rs}(443)$ and $R_{rs}(488)$ indicates increased absorption in the blue wavelengths. CDOM, Chl*a* and nonalgal particles all absorb most strongly in the blue end of the visible spectrum. Therefore, these trends in $R_{rs}(\lambda)$ indicate an increase in one or more of these optically active constituents.

Based on field data, locations 6 and 11 are located in areas where $a_{nap}(\lambda)$ dominated total non-water absorption and exhibited higher AVW values (490-510 nm). One previous study indicated that the sources of nonalgal particles on the Chukchi Shelf included resuspension from the bottom to the surface ocean, cellular material left over from a large bloom or microbial heterotrophs (Neukermans et al. 2016). Both locations have exhibited positive trends in AVW over the study period. Location 4 is located in an area that was dominated by $a_g(\lambda)$ and bluer AVW (485 nm) but has exhibited a significant increase in AVW over the study period, ending at

501 nm in 2018. Location 7, on the other hand, is located in an area that was dominated by $a_{ph}(\lambda)$ and showed high values of AVW (>490 nm). This case study suggests that the strong contributions of $a_{nap}(\lambda)$, $a_{ph}(\lambda)$ or a mix of the two result in higher AVW values. The addition of sea ice and Chl*a* observations can assist in determining which constituent is dominating at a specific time. Although this analysis is limited in scope, it is proof that additional field data, such as coincident biological, bio-optical and radiometric profiles, could strengthen the validity of this theorem.

4.4.4 A loss of sea ice and indications of a fall bloom

Sea ice concentrations in the Chukchi Sea have significantly declined over the last decade related to warmer air and SSTs. The loss of multiyear sea ice as well as a decline in sea ice extent has been reported extensively in this region (Frey et al. 2014, Stroeve et al. 2014, Frey et al. 2015, Frey et al. 2019, Grebmeier et al. 2019). As such, trends in sea ice concentration within the Chukchi Sea were computed and compared with the trends in AVW and Chl*a*. Median trend analysis on monthly SSM/I and SSMS sea ice concentrations (January-December 2003-2018) indicated a significant (Mann Kendall, $p<0.1$) negative trend (indicated by the red color in Figure 4.8) in sea ice concentrations at a rate of ~-15-25%/decade within the Chukchi Sea and north of the Chukchi Sea in all months except April. It is important to note that the Chukchi Sea is mostly open water during the summer and autumn months, (July-September) so the trend the analysis was used to evaluate the pre- and post-conditioning of the Chukchi Sea or, in other words, the timing of sea ice breakup and formation.

The large, significant declines of sea ice concentrations both in the spring (May-June) and autumn/early winter months (October, November and December) observed in this study indicate earlier sea ice break up and later sea ice formation, respectively. The timing of sea ice breakup controls the timing of sea ice and pelagic phytoplankton bloom formation. Nutrients regenerated over the winter and released when the ice has melted initially support the spring diatom-dominated bloom and are further supported by the Pacific inflow of nutrients. Once the water becomes warmer, stratified and nutrient deficient, surface chlorophyll declines and smaller phytoplankton types dominate the water column (Neeley et al., 2018). Earlier sea ice breakup and later sea ice formation allows for longer open water duration in the Chukchi Sea and allow additional physical and biological processes to take place. For example, open water in September allows wind mixing events to occur that resuspend nutrients from the bottom, supporting a fall bloom (Nishino et al. 2015). Satellite Chl*a* observations indicate a second fall bloom is occurring in the Chukchi Sea, which has been observed by previous studies (Ardyna et al. 2014, Frey et al. 2019). A region that was once defined by one annual bloom initiated by sea ice break up and increased sunlight just over a decade ago is now becoming a region with a secondary bloom like that of temperate oceanic regions (Ardyna et al. 2014). These changes indicate that the Chukchi Sea is beginning to mimic seasonal patterns observed at lower latitudes.

4.4.5 SST trends coincident with declining sea ice concentrations

In addition to sea ice concentrations, we also evaluated whether SST trends over the 2003-2018 study period could have contributed to the patterns observed in

AVW and Chl*a*. Median trend analysis did reveal some patches of positive (warming) and negative (cooling) SSTs across the Chukchi Sea during all four months (Figure 4.9). Although we did not observe the same regionally significant trends as AVW and Chl*a*, there were some coincident regions of SST trends. For example, a significant ($p<0.1$) trend in SST is observed in the same region as a negative trend in Chl*a* in June (see black circle in Figure 4.9a). Secondly, within the region of the eastern Chukchi Sea that exhibited a negative trend in Chl*a* and an increase in SST was observed for the month of July (see black circle in Figure 4.9b). In August, a significant negative trend in Chl*a* was observed in the Kotzebue Sound coincident with a negative trend in SST (see circle in Figure 4.9c). Interestingly, although both sides of the southern Chukchi Sea exhibited positive trends in Chl*a*, the western side exhibited a negative trend in SST while the eastern side exhibited a positive trend in SST (see circles in Figure 4.9d). It appears that some warming and cooling has occurred in the Chukchi over the study period; however, a direct relationship among the trends in SST, AVW and Chl*a* is not apparent. Although this study did not show large significant trends in SST, possibly related to the short time scale of the study, other studies have shown that there has been a significant increase in SST anomalies in the Chukchi Sea between 1982 and 2019 of 0.08 °C/year (Frey et al. 2019). This makes sense as longer open water duration allows for enhanced solar insolation of heat in the open waters, creating a positive feedback loop of warmer water and delayed sea ice formation (Frey et al. 2014, Neeley et al. 2018). An evident relationship exists between trends in AVW and Chl*a* with some increases in SST and longer open water duration driven by a decline in sea ice concentrations.

4.4.6 Recommendations for remote sensing applications

The AVW represents the apparent, dominant color of the subsurface ocean. The apparent color is a manifestation of the optical properties of the water column, which are driven by all types of optically active constituents, dissolved and particulate. Trends therein indicate that one or more of those constituents are changing, phytoplankton being only one. Trends in AVW are indicators of change. Investigation into the mechanisms prompting the change requires additional data, including that of in-water optical properties (particle size distribution, absorption and scattering), full radiometric spectra, and indicators of phytoplankton taxonomy. From this additional information, any observed trends in AVW may be unraveled and explained.

The AVW trends described in this study indicate that an underlying change in the optical properties of large regions of the Chukchi Sea is reddening, which is manifested in the $R_{rs}(\lambda)$ spectral shape. PCA analysis presented in this study indicated that the 'redder' values of AVW are influenced by nonalgal particles, phytoplankton community, or both simultaneously. Unfortunately, these field data are limited to 2010 and 2011. Additional field data that include particle absorption and phytoplankton taxonomy, particularly in more recent years (e.g., 2015 and thereafter) that exhibited the strongest trends in AVW, are required to further elucidate the cause of the red shift in AVW. Data that consist of nonalgal particle absorption and phytoplankton taxonomy over the entire study period could use used to explain current and future trends in AVW and $R_{rs}(\lambda)$ spectral shape.

The spectral shape of phytoplankton absorption that contributes to the overall apparent color of the water column is determined by taxonomic group-specific cellular photosynthetic and photoprotective pigment composition (Ciotti et al. 2002). The difference in spectral shape among different taxonomic groups can be exploited to derive phytoplankton community composition and size classes from satellite ocean color data (Ciotti et al. 2002, Devred et al. 2011). The combination of spectral absorption information and measurements of taxonomic diversity in the Chukchi Sea would provide a robust mechanism to understand how changes in taxonomic diversity may be influencing AVW. A recent study conducted in collaboration with NASA Goddard and Bigelow Laboratory looking at taxon-specific optical properties, including both scatter and absorption, using phytoplankton monocultures (NASA OBB Grant **NNH15ZDA001N**) will be valuable for gaining insights into phytoplankton diversity and AVW in the Chukchi Sea.

Hyperspectral (high spectral resolution) radiometric information is key to better understanding the optically active constituents, in particular phytoplankton taxonomy, in the global ocean. Current ocean color instruments measure $R_{rs}(\lambda)$ at up to 12 wavelengths in the ultraviolet-visible spectrum that are required for measuring phytoplankton. NASA's upcoming PACE (Plankton Aerosols Clouds and ocean Ecosystem) mission will be the first to provide global ocean, hyperspectral coverage at 5nm resolution extended in both the UV and near infrared and short wave infrared wavelengths (Cetinic et al. 2018, Werdell et al. 2019). Hyperspectral capability is essential for detecting unique spectral patterns that distinguish different phytoplankton taxonomic groups that current sensors miss because of the wider

spectral bandwidth that miss taxonomic-specific spectral features. For example, in Figure 4.11, the spectral features of HAB and non-HAB forming taxa are shown to illustrate how hyperspectral information (4.11a) captures spectral features that a multispectral OCI would miss (Figure 4.11b). As such, PACE in conjunction with remote sensing algorithms, such as AVW and phytoplankton taxonomy algorithms, will provide more spectral information, and this provide more information and insights into ecosystem-level changes in the Chukchi Sea.

4.5 Conclusions

The optical signature of the ocean can be an indicator of water quality and the state of the ecosystem. Absorption and backscatter by dissolved matter, as well as living and non-living particles fundamentally control the spectral shape of $R_{rs}(\lambda)$. Therefore, trends in $R_{rs}(\lambda)$ and spectral shape can provide information about what in the water column within the scope of satellite observations. Previous studies have suggested that $R_{rs}(\lambda)$ represents a stronger signal of ecosystem change due to lower natural variability than Chl*a*. Moreover, $R_{rs}(\lambda)$ embodies all optically important constituents, not just phytoplankton biomass (Dutkiewicz et al. 2019). In this study we explored the utility of a new tool, the AVW algorithm, to evaluate trends in the optical signature of the Chukchi Sea. We found that there was a significant red shift in AVW over the late spring and summer months from 2003-2018 related to declines in sea ice concentration and increases in Chl*a*. There is also a mismatch between AVW and Chl*a*, particularly in July, suggesting that patterns in AVW, and thus $R_{rs}(\lambda)$, can be become decoupled from Chl*a*. The absorption case study suggests that an increase in nonalgal particles may also be contributing to the overall red shift in

AVW. Regardless of the underlying cause, this study demonstrated that the AVW algorithm and subsequent trends in $R_{rs}(\lambda)$ have revealed a fundamental ecosystem change that is occurring, even over this short time series. AVW scenes for 2019 (Figure 4.10) indicate that the positive trends in AVW observed in this study are not anomalous and are continuing in the Chukchi Sea. Future studies that include additional field data such as phytoplankton taxonomy, could allow further development of this approach and to fully characterize the ecosystem changes that are occurring in the Chukchi Sea.

Figures Chapter 4

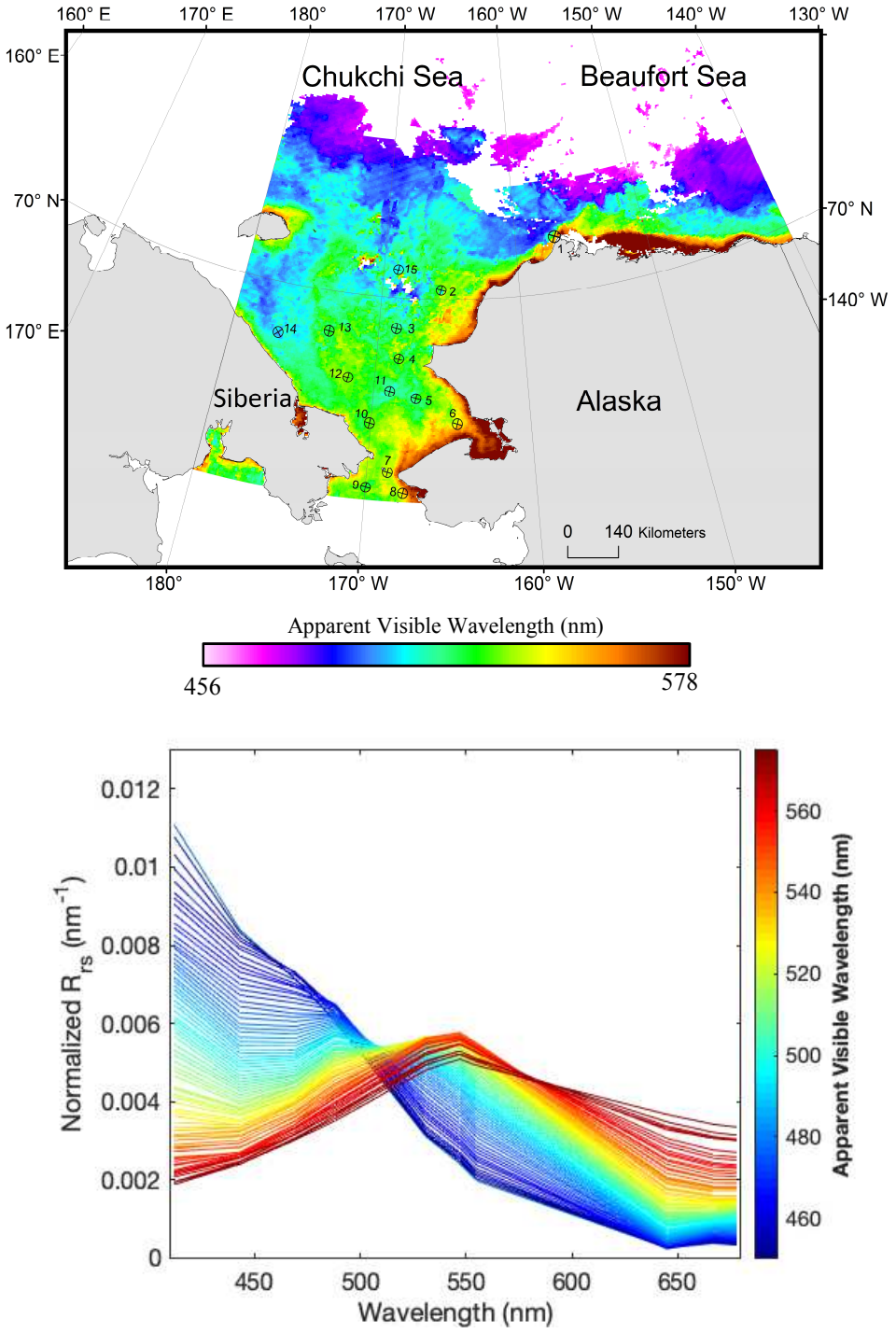

Figure 4.1 a) Example AVW scene derived from MODISA AVW in September 2018 in units of nm. The numbered circles represent locations examined in detail later in this chapter. b) A plot showing integral-normalized $R_{rs}(\lambda)$ spectra for September 2018 that correspond with the AVW values.

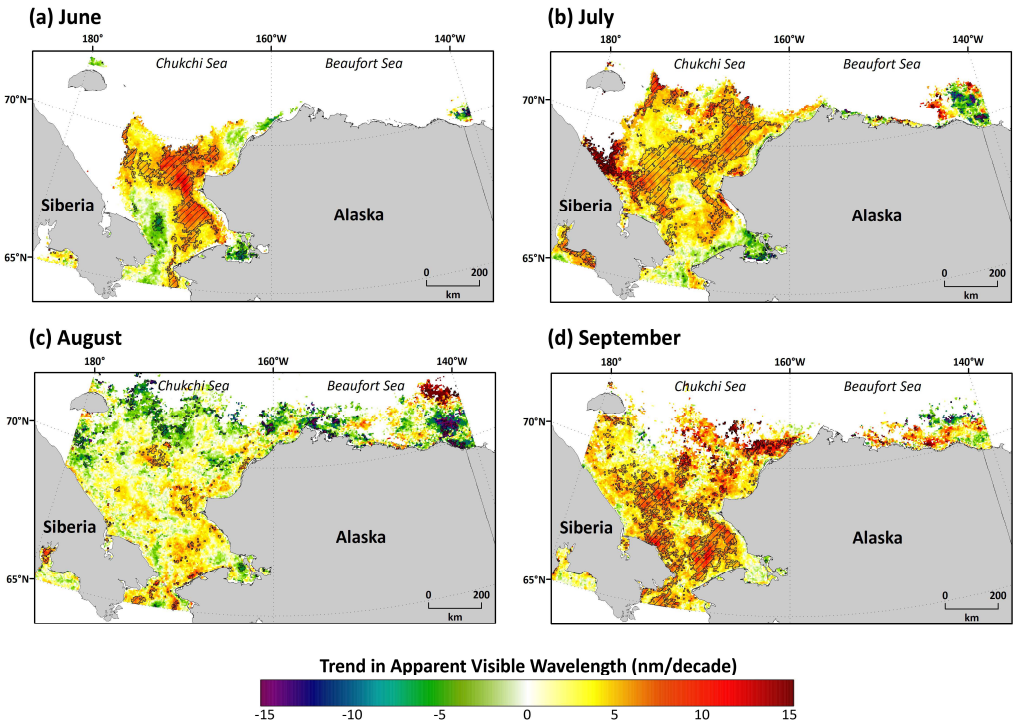

Figure 4.2. Theil Sen median trend plots of AVW for a) June, b) July, c) August and d) September in units of nm/decade. Hashed polygons represent regions of significant trends ($p<0.1$) based on the Mann-Kendell significance test.

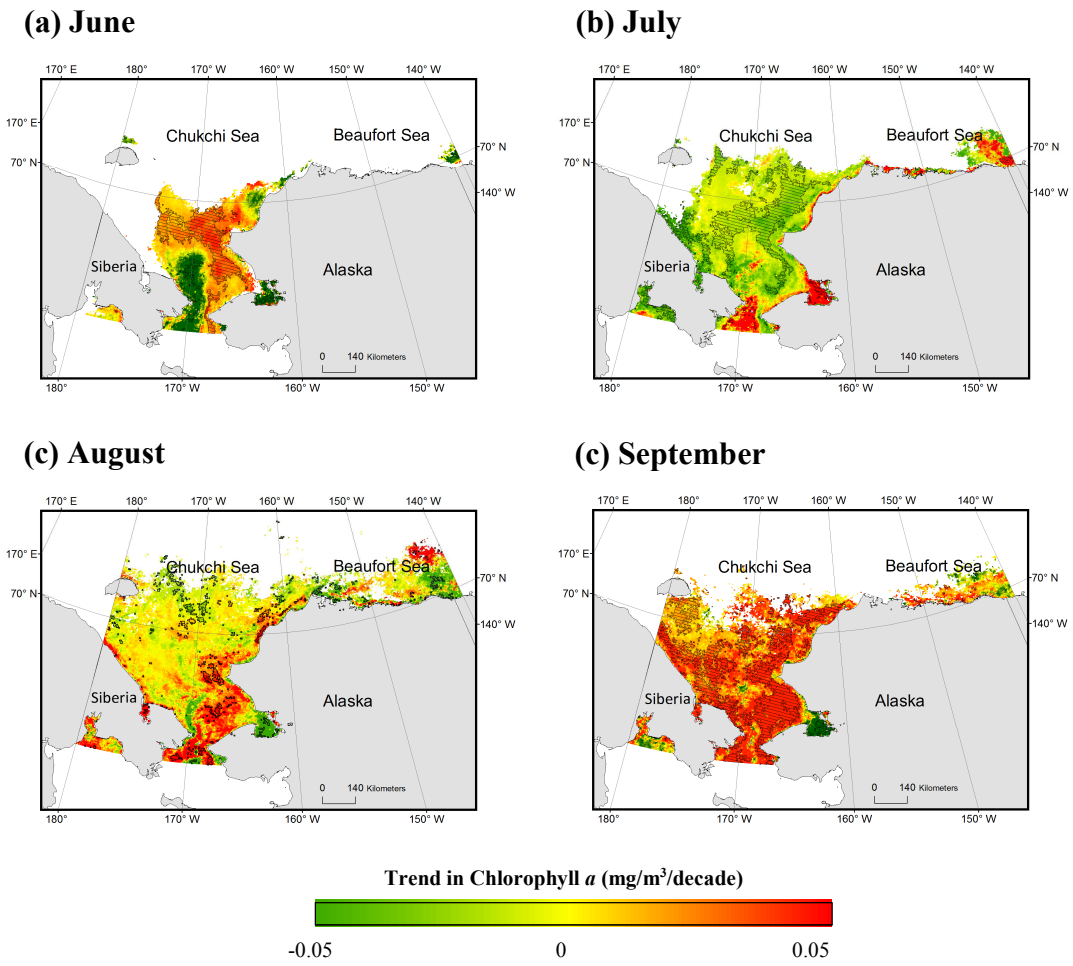

Figure 4.3. Theil Sen median trend plots of monthly 4km resolution MODISA Chl*a* for a) June, b) July, c) August and d) September in units of mg/m^3/decade. Hashed polygons represent regions of significant trends ($p<0.1$) based on the Mann-Kendell significance test.

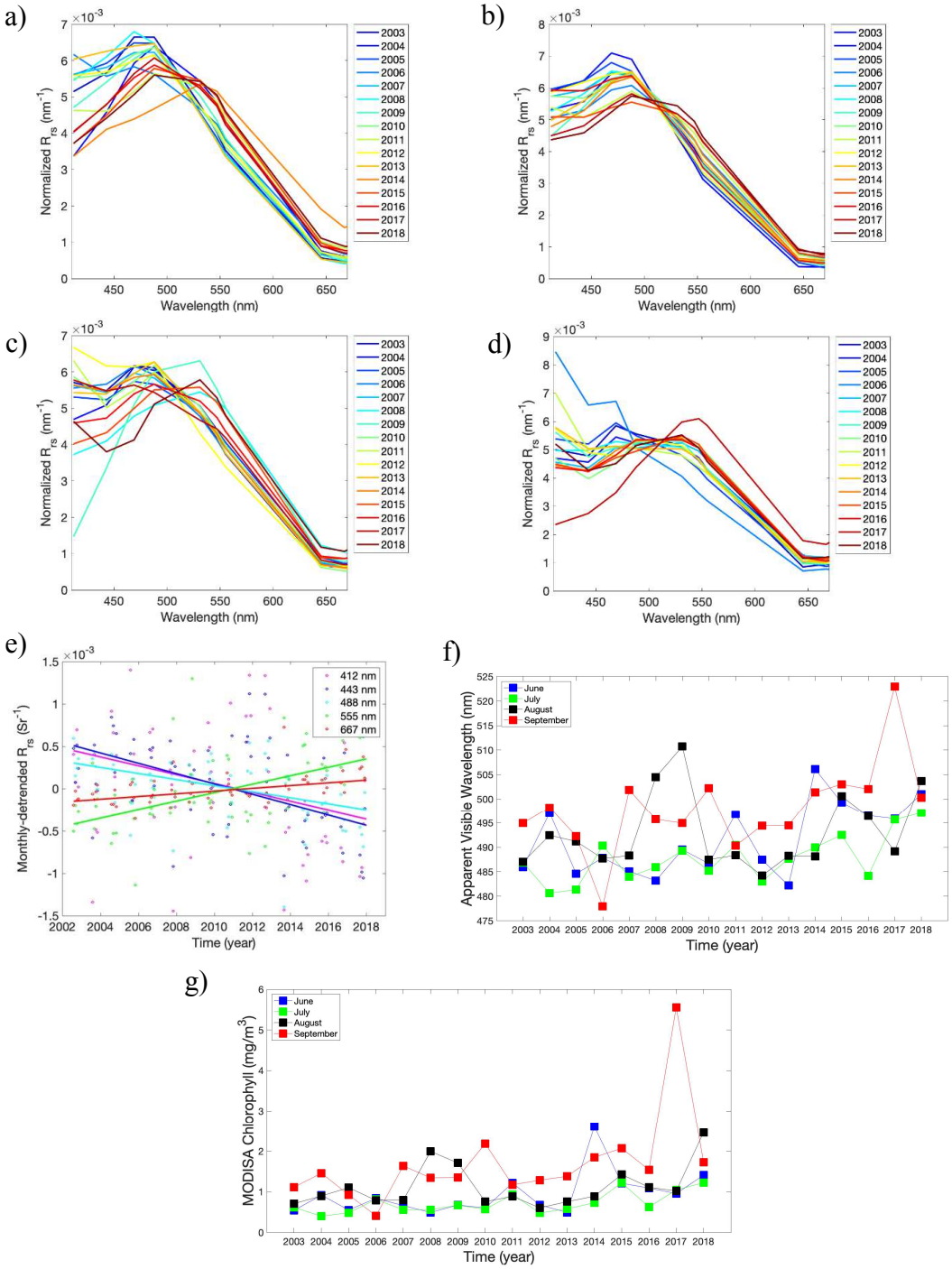

Figure 4.4. Integral-normalized $R_{rs}(\lambda)$ in plots in units of nm^{-1} for Location 4 in a) June b) July c) August and d) September. Line colors represent year of observation. e) Regression analysis plot of select $R_{rs}(\lambda)$ channels showing a significant decrease in $R_{rs}(412)$, $R_{rs}(443)$ and $R_{rs}(488)$ and a significant increase in $R_{rs}(555)$ and $R_{rs}(667)$ over the study period. f) Location 4 monthly AVW values in units of nm. g) Location 4 monthly Chl*a* in units of mg/m^3 for June-September, 2003-2018. The trend was significantly positive in June and negative in July ($p<0.1$).

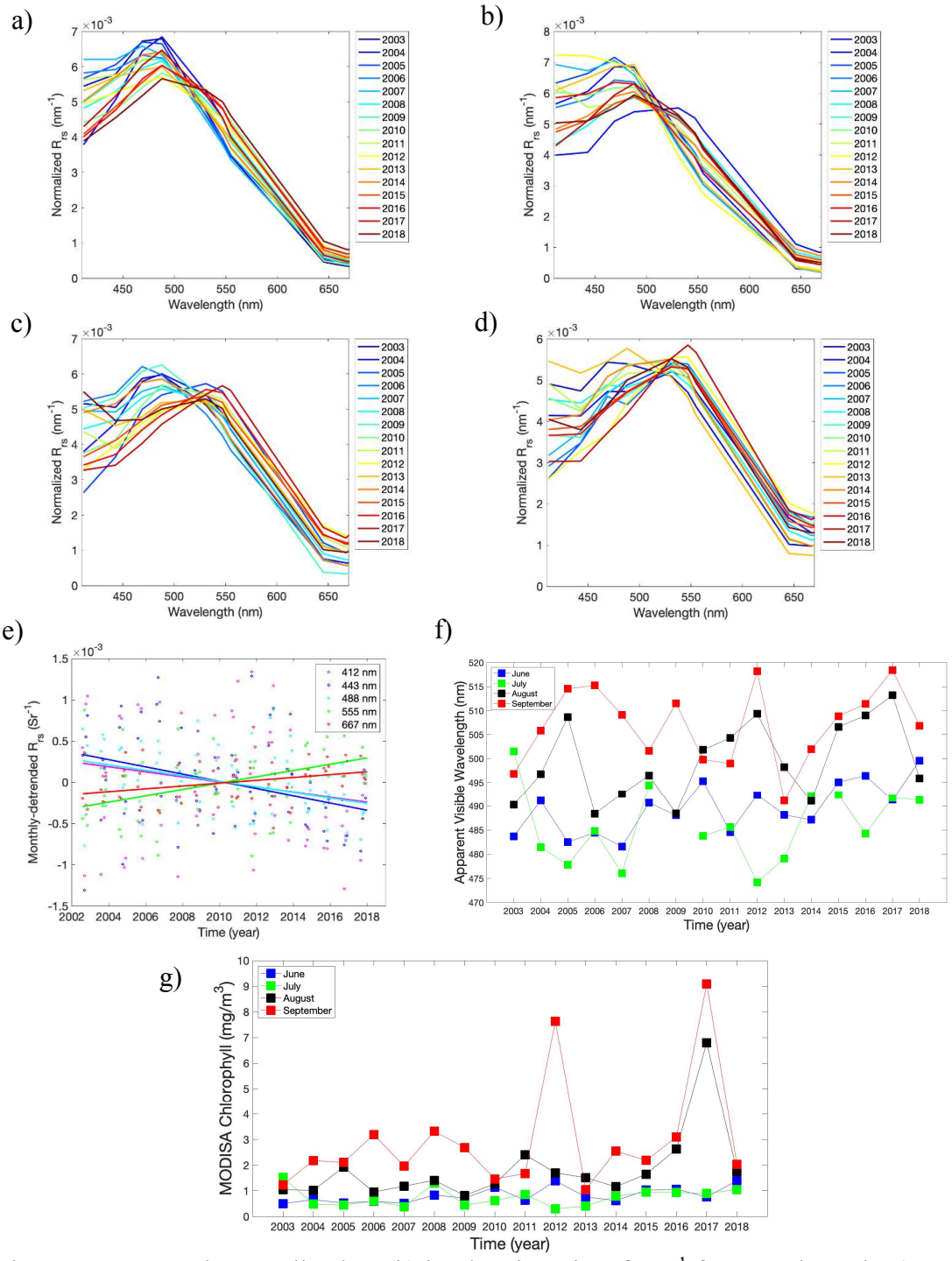

Figure 4.5. Integral-normalized $R_{rs}(\lambda)$ in plots in units of nm^{-1} for Location 8 in a) June b) July c) August and d) September. Line colors represent year of observation. e) Regression analysis plot of select $R_{rs}(\lambda)$ channels showing a significant decrease in $R_{rs}(443)$ and $R_{rs}(488)$ and a significant increase in $R_{rs}(555)$ and $R_{rs}(667)$ over the study period. f) Location 8 monthly AVW values in units of nm. g) Location 8 monthly Chl*a* in units of mg/m^3 for June-September, 2003-2018. The trends were significantly positive in June and August ($p<0.1$).

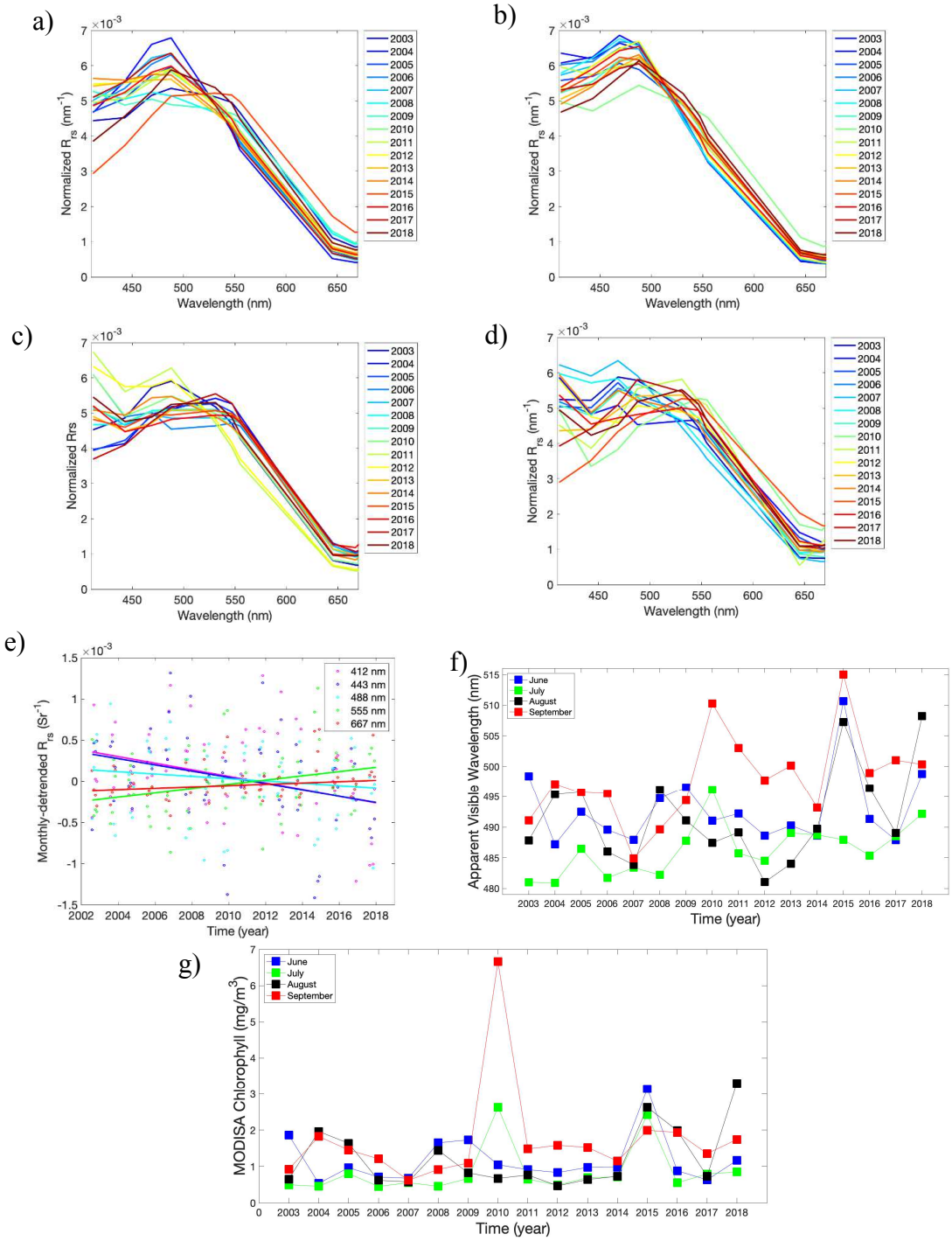

Figure 4.6. Integral-normalized $R_{rs}(\lambda)$ in plots in units of nm^{-1} for Location 12 in a) June b) July c) August and d) September. Line colors represent year of observation. e) Regression analysis plot of select $R_{rs}(\lambda)$ channels showing a significant decrease in $R_{rs}(412)$ and $R_{rs}(443)$ and a significant increase in $R_{rs}(555)$ and $R_{rs}(667)$ over the study period. f) Location 12 monthly AVW values in units of nm.
g) Location 12 monthly Chl*a* in units of mg/m^3 for June-September, 2003-2018. The trend was significantly negative in July ($p<0.1$).

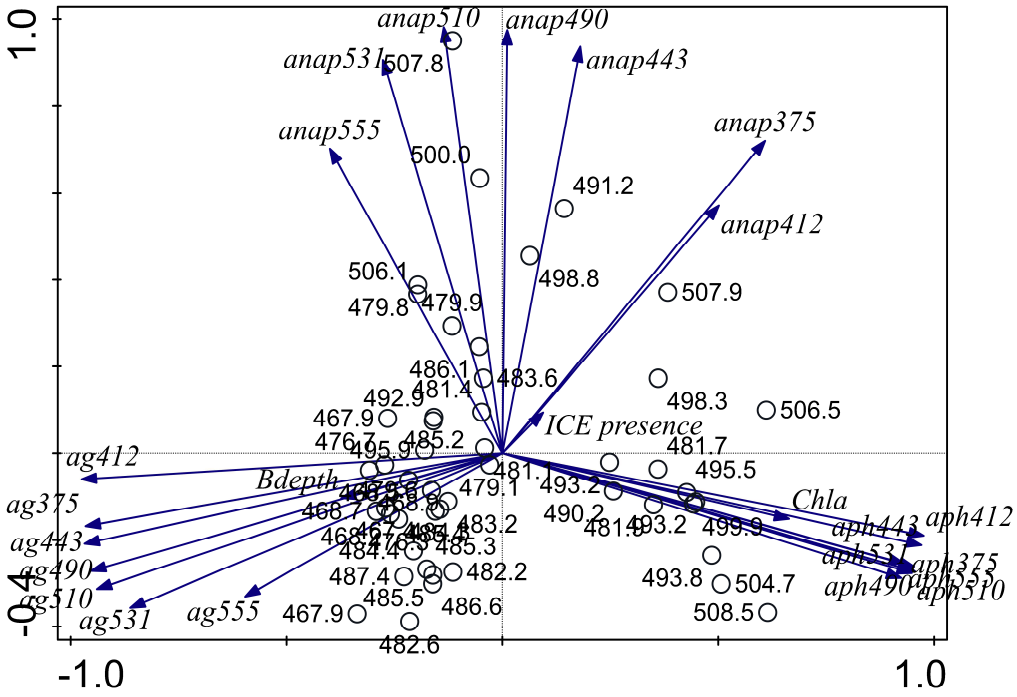

Figure 4.7. The PCA biplot shows the relationship between AVW and $a_g(\lambda)$, $a_{ph}(\lambda)$ and $a_{nap}(\lambda)$. Vector lengths indicate the strength of the relationship. ICE presence, bottom depth and Chl*a* were added to further elucidate the relationship between absorption and AVW.

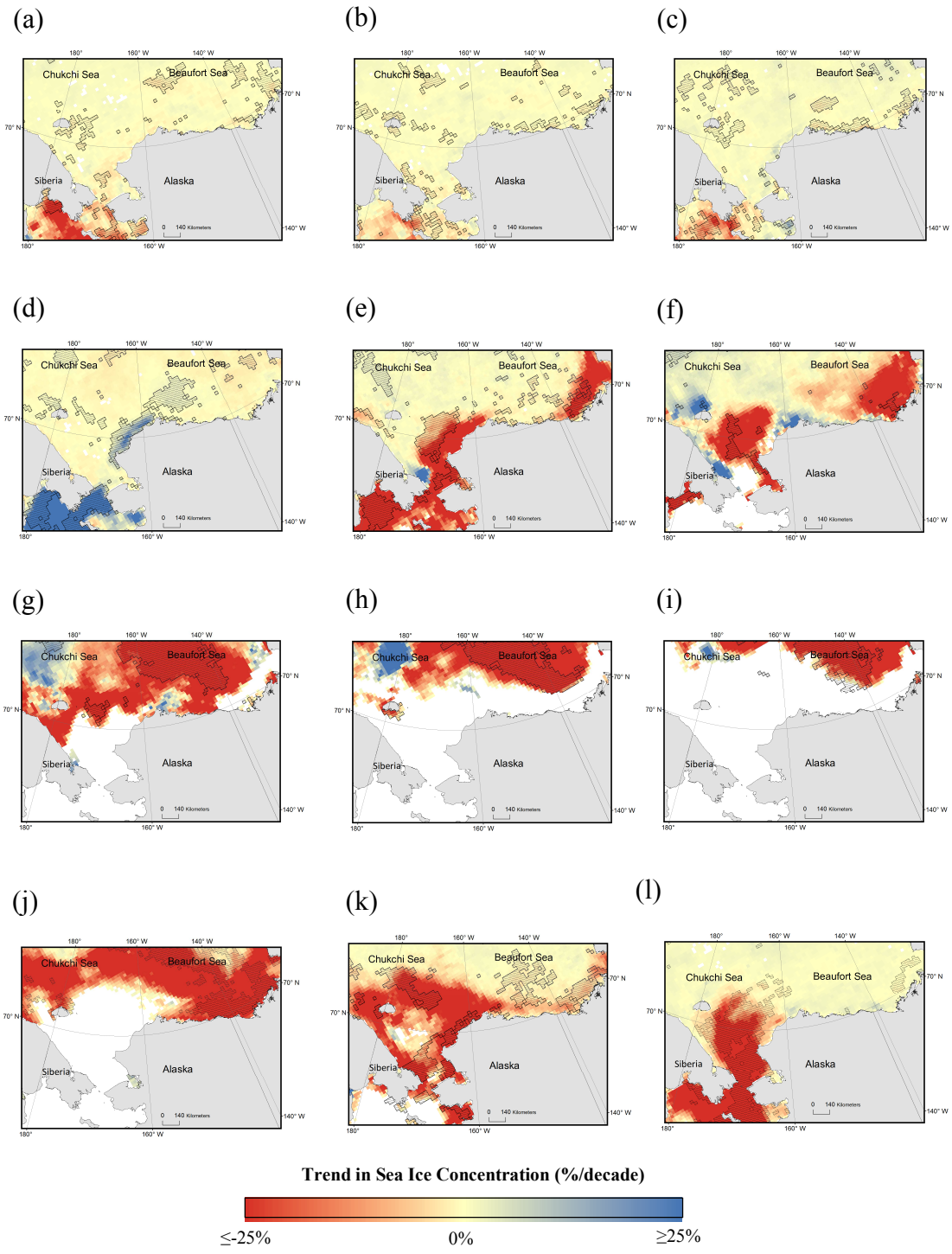

Figure 4.8. Theil Sen median trend plots of monthly sea ice concentrations (%/decade) for January (a) -December (l) 2003-2018. Red cooler indicates a loss of sea ice concentration while blue color indicates increase in sea ice concentration. Hashed polygons represent regions of significant trends ($p<0.1$) based on the Mann-Kendell significance test.

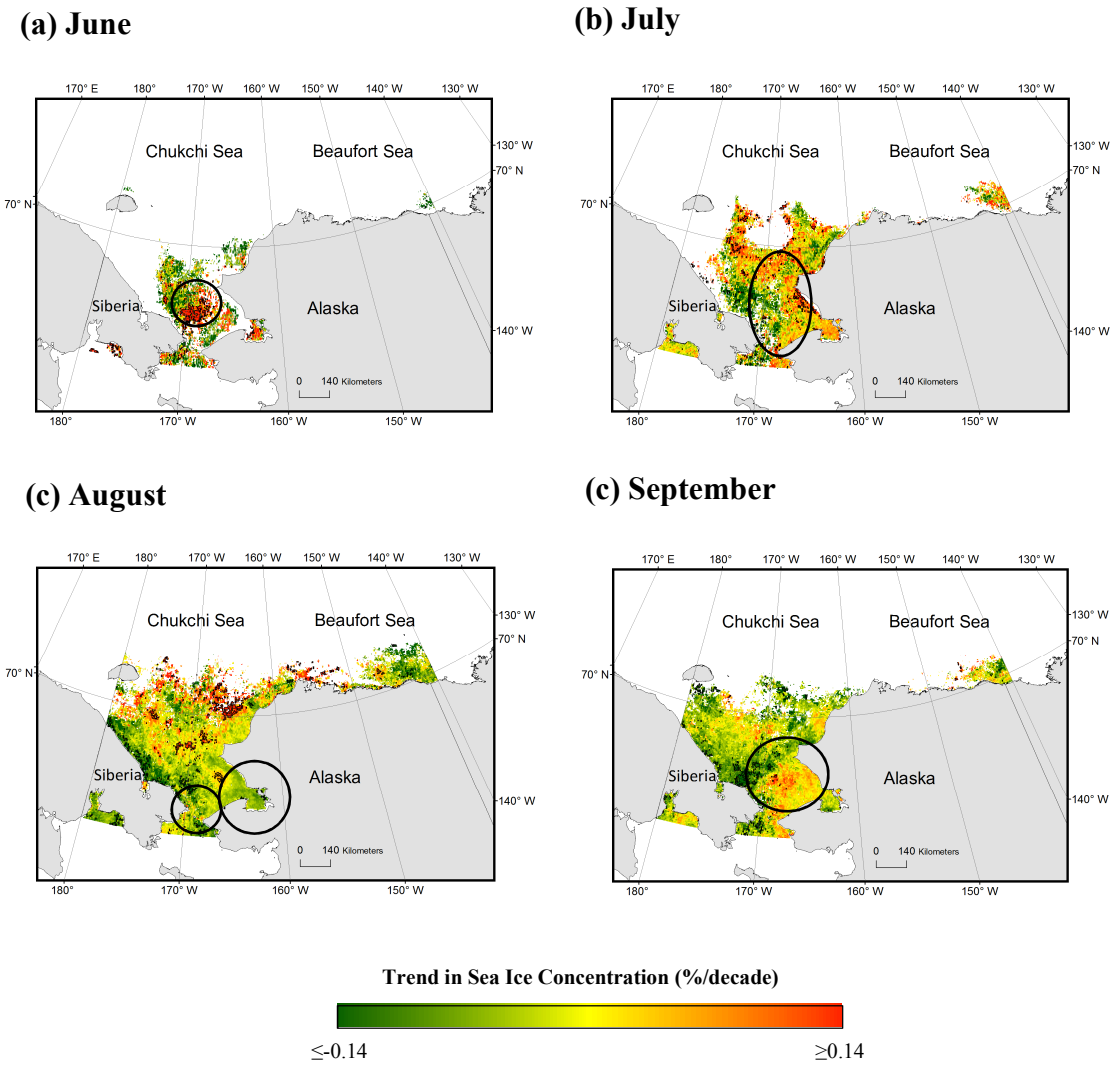

Figure 4.9. Theil Sen median trend plots of MODISA Daytime 11µ SST for a) June, b) July, c) August and d) September in units of °C/decade. Hashed polygons represent regions of significant trends ($p<0.1$) based on the Mann-Kendell significance test. Circles indicate large regions of warming or cooling.

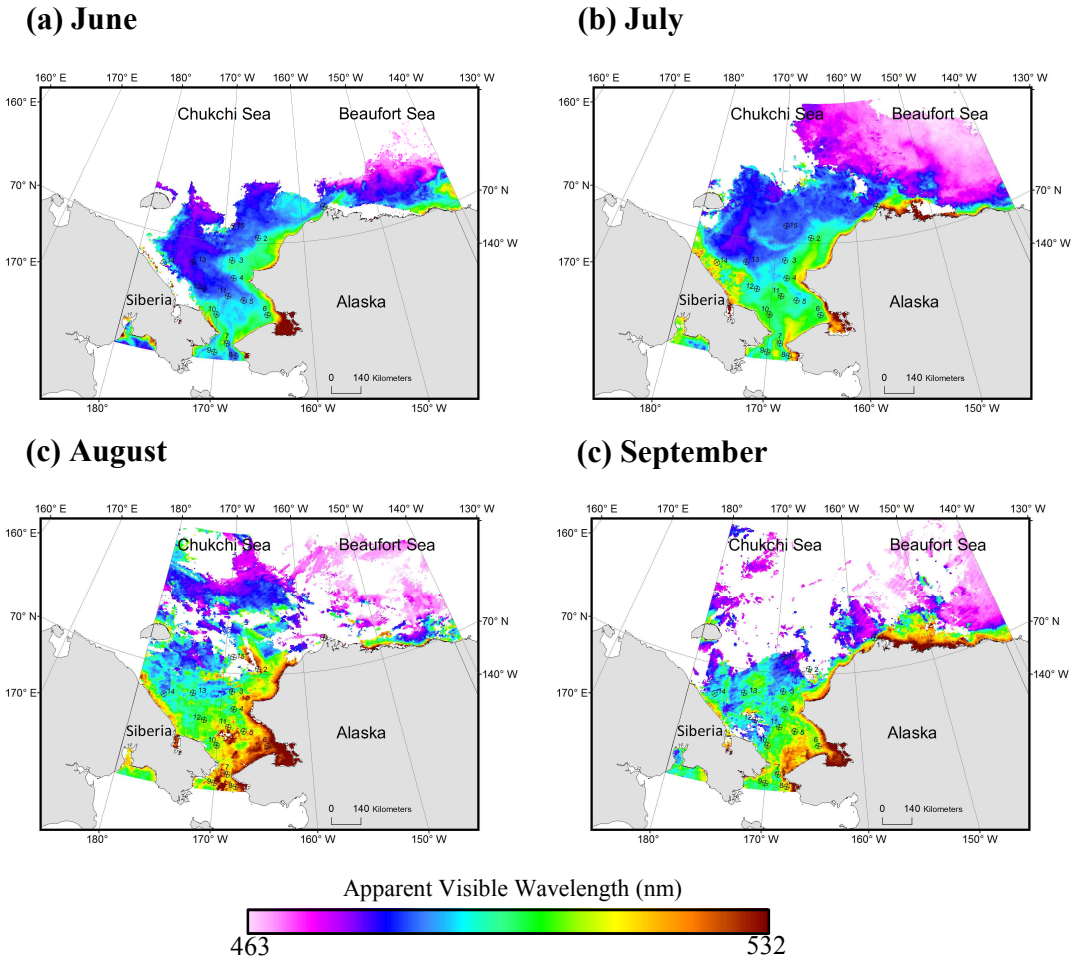

Figure 4.10. MODISA scenes of AVW for a) June, b) July, c) August and d) September 2019 in units of nm.

a)

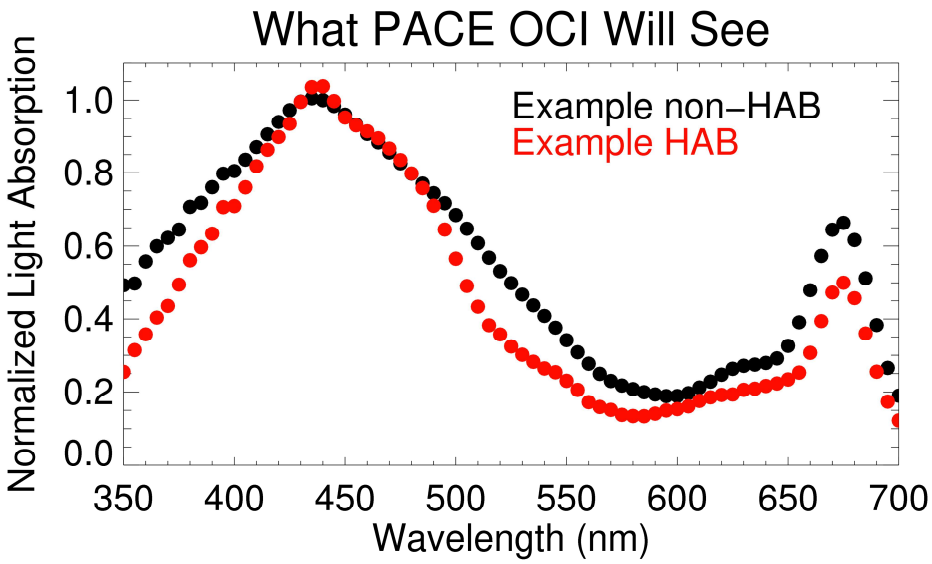

b)

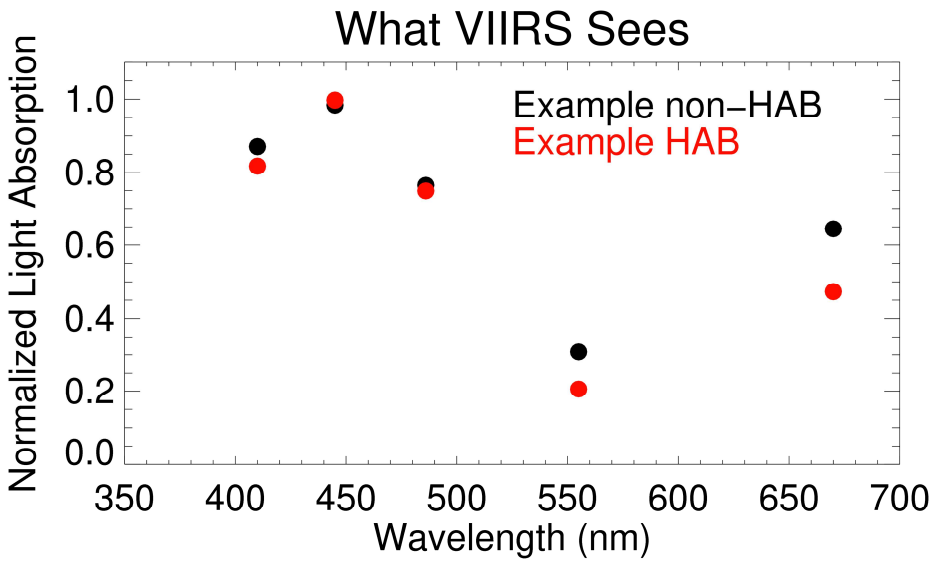

Figure 4.11. a) Hyperspectral light absorption as measured at a resolution of 5 nm, indicative that which will be measured by PACE. b) Multispectral lights absorption measured by current ocean color instruments. Figures take from the NASA PACE website[6]

[6] https://pace.oceansciences.org

Tables Chapter 4

Table 4.1 AVW trend statistics for fifteen locations in June 2003-2018. Red represents positive trends and blue represents negative trends. P values in **bold** indicate statistical significance.

Location	Latitude	Longitude	Trend (nm/decade)	p value	AVW 2003	AVW 2018
1	71.379	-156.954	NaN	NaN	489.96	479.44
2	70.212	-165.688	5.48	0.32	482.72	496.05
3	69.240	-168.783	9.99	**0.05**	483.96	498.93
4	68.500	-168.500	7.93	**0.03**	485.93	501.02
5	67.539	-167.251	8.79	**0.01**	484.39	500.36
6	66.938	-164.604	8.53	0.32	485.23	500.64
7	65.703	-168.766	2.89	0.55	497.53	499.96
8	65.211	-167.811	8.46	**0.02**	483.68	499.58
9	65.303	-169.979	0.12	0.96	507.40	504.94
10	66.876	-170.083	-6.95	**0.04**	510.11	499.93
11	67.680	-168.958	2.13	0.55	498.01	505.24
12	67.937	-171.748	-0.26	0.96	498.38	498.79
13	69.006	-173.400	5.55	**0.01**	481.82	492.89
14	68.759	-176.810	NaN	NaN	501.05	NaN
15	70.698	-168.923	NaN	NaN	500.57	494.85

Table 4.2 AVW trend statistics for fifteen locations in July 2003-2018. Red represents positive trends and blue represents negative trends. P values in **bold** indicate statistical significance.

Location	Latitude	Longitude	Trend (nm/decade)	p value	AVW 2003	AVW 2018
1	71.379	-156.954	2.36	0.68	481.38	484.31
2	70.212	-165.688	8.54	**0.004**	478.12	491.56
3	69.240	-168.783	8.85	**0.01**	474.93	496.11
4	68.500	-168.500	6.64	**0.01**	486.85	497.10
5	67.539	-167.251	5.37	0.22	488.08	500.39
6	66.938	-164.604	-0.60	0.82	501.31	500.04
7	65.703	-168.766	-0.37	0.96	491.90	489.47
8	65.211	-167.811	6.43	0.39	490.22	495.90
9	65.303	-169.979	-0.47	0.964	497.92	492.51
10	66.876	-170.083	3.79	0.3	498.83	499.28
11	67.680	-168.958	0.04	1	496.07	499.22
12	67.937	-171.748	5.92	**0.003**	481.02	492.19
13	69.006	-173.400	4.67	**0.017**	476.57	495.17
14	68.759	-176.810	23	**0.01**	478.45	518.96
15	70.698	-168.923	4.37	0.3894	470.59	488.38

Table 4.3 AVW median trend statistics for fifteen locations in August 2003-2018 Red represents positive trends and blue represents negative trends. P values in **bold** indicate statistical significance.

Location	Latitude	Longitude	Trend (nm/decade)	p value	AVW 2003	AVW 2018
1	71.379	-156.954	-7.91	0.79	488.55	475.05
2	70.212	-165.688	-4.91	0.37	493.16	477.18
3	69.240	-168.783	2.49	0.62	485.60	495.83
4	68.500	-168.500	2.25	0.34	487.02	503.67
5	67.539	-167.251	1.70	0.75	486.91	496.89
6	66.938	-164.604	-2.23	0.44	511.78	507.88
7	65.703	-168.766	4.86	0.28	490.96	488.84
8	65.211	-167.811	8.52	**0.04**	490.22	495.90
9	65.303	-169.979	6.53	**0.08**	495.22	508.50
10	66.876	-170.083	-3.33	0.44	495.05	504.13
11	67.680	-168.958	-0.37	1	494.27	495.58
12	67.937	-171.748	4.17	0.44	487.83	508.22
13	69.006	-173.400	1.68	0.82	487.26	492.02
14	68.759	-176.810	1.70	0.82	487.78	503.09
15	70.698	-168.923	-3.45	0.32	476.44	NaN

Table 4.4 AVW median trend statistics for fifteen locations in September 2003-2018. Red represents positive trends and blue represents negative trends. P values in **bold** indicate statistical significance.

Location	Latitude	Longitude	trend (nm/decade)	p value	AVW 2003	AVW 2018
1	71.379	-156.954	5.56	0.68	482.33	507.31
2	70.212	-165.688	0.98	0.79	494.78	495.56
3	69.240	-168.783	0	1	490.94	494.13
4	68.500	-168.500	6.14	0.13	494.99	500.25
5	67.539	-167.251	6.47	**0.05**	491.88	495.90
6	66.938	-164.604	4.61	0.22	508.39	506.35
7	65.703	-168.766	1.18	0.69	504.29	504.79
8	65.211	-167.811	2.84	0.75	496.81	506.83
9	65.303	-169.979	4.40	0.19	500.03	497.68
10	66.876	-170.083	6.98	0.05	492.93	499.86
11	67.680	-168.958	1.80	0.55	489.99	492.35
12	67.937	-171.748	5.80	**0.09**	491.09	500.34
13	69.006	-173.400	4.02	0.26	486.27	496.16
14	68.759	-176.810	6.18	0.34	491.15	485.57
15	70.698	-168.923	6.30	0.47	NaN	487.31

Table 4.5. Regression statistics for fifteen locations. Trends in $R_{rs}(\lambda)$ are in units of 10^{-4} Sr^{-1} $decade^{-1}$. Values in **bold** and indicated by an * indicate statistical significance ($p<0.1$).

Location	Latitude	Longitude	412 nm	443 nm	488 nm	555 nm	667 nm
1	71.379	-156.954	-2.088	-3.101	-2.133	2.036	**1.276***
2	70.212	-165.688	-1.843	**-3.425***	**-1.860***	**2.639***	**0.6760***
3	69.240	-168.783	-2.735	**-5.046***	**-3.745***	**4.367***	**1.271***
4	68.500	-168.500	**-5.231***	**-6.094***	**-3.597***	**4.988***	**1.618***
5	67.539	-167.251	**-4.495***	-4.926	**-2.616***	3.831	1.610
6	66.938	-164.604	-2.250	**-2.571**	-1.160	**1.924**	**1.089**
7	65.703	-168.766	**-3.406***	-0.282	**1.951***	-0.333	0.007
8	65.211	-167.811	-3.063	**-4.379***	**-3.335***	**3.828***	**1.728***
9	65.303	-169.979	-2.394	-1.787	-0.997	1.505	1.267
10	66.876	-170.083	-2.220	-1.195	0.431	0.766	0.388
11	67.680	-168.958	-0.643	-0.646	0.483	0.159	0.422
12	67.937	-171.748	**-4.006***	**-3.791***	-1.425	**2.572***	**0.802***
13	69.006	-173.400	**-4.686***	**-4.689***	**-1.532***	**2.988***	**1.061***
14	68.759	-176.810	-1.971	**-4.082***	-1.591	**2.637***	8.892
15	70.698	-168.923	-2.000	**-3.761***	**-1.651***	**2.642***	**8.851***

Table 4.6 Chl*a* median trend statistics for fifteen locations in June 2003-2018. Red represents positive trends and blue represents negative trends. P values in **bold** indicate statistical significance.

Location	Latitude	Longitude	Trend (mg/m^3/decade)	p value	Chl*a* 2003	Chl*a* 2018
1	71.379	-156.954	-0.346	0.44	1.143	0.455
2	70.212	-165.688	0.099	0.79	0.504	0.972
3	69.240	-168.783	0.414	**0.04**	0.493	1.126
4	68.500	-168.500	0.313	**0.02**	0.544	1.406
5	67.539	-167.251	0.407	**0.003**	0.532	1.644
6	66.938	-164.604	0.519	0.13	0.557	1.309
7	65.703	-168.766	-0.3	0.39	2.4723	1.585
8	65.211	-167.811	0.358	**0.006**	0.502	1.396
9	65.303	-169.979	-1.4	0.30	4.902	2.330
10	66.876	-170.083	-1.225	0.16	5.087	1.692
11	67.680	-168.958	-0.469	0.22	2.134	1.912
12	67.937	-171.748	-0.041	0.89	1.859	1.170
13	69.006	-173.400	0.265	**0.01**	0.448	0.926
14	68.759	-176.810	NaN	NaN	1.708	NaN
15	70.698	-168.923	NaN	NaN	3.329	1.220

Table 4.7 Chl*a* median trend statistics for fifteen locations in July 2003-2018. Red represents positive trends and blue represents negative trends. P values in **bold** indicate statistical significance.

Location	Latitude	Longitude	Trend (mg/m^3/decade)	p value	Chl*a* 2003	Chl*a* 2018
1	71.379	-156.954	-0.081	0.65	0.567843	0.661827
2	70.212	-165.688	-0.293	**0.01**	0.351025	0.490868
3	69.240	-168.783	-0.431	**0.01**	0.307545	1.058894
4	68.500	-168.500	-0.305	**0.01**	0.616698	1.222433
5	67.539	-167.251	-0.274	0.44	0.970996	1.544643
6	66.938	-164.604	-0.063	0.82	1.672712	1.591006
7	65.703	-168.766	0.497	0.26	1.457	0.908
8	65.211	-167.811	-0.278	0.24	1.519529	1.050687
9	65.303	-169.979	1.643	0.26	2.965987	1.336809
10	66.876	-170.083	-0.051	0.82	2.820528	1.614782
11	67.680	-168.958	0.296	0.62	2.072308	1.620791
12	67.937	-171.748	-0.241	**0.02**	0.49904	0.850097
13	69.006	-173.400	-0.105	0.16	0.363081	0.979158
14	68.759	-176.810	-0.748	**0.004**	0.413883	3.269153
15	70.698	-168.923	-0.297	0.21	0.211446	0.639284

Table 4.8 Chl*a* median trend statistics for fifteen locations in August 2003-2018. Red represents positive trends and blue represents negative trends. P values in **bold** indicate statistical significance.

Location	Latitude	Longitude	Trend (mg/m^3/decade)	p value	Chl*a* 2003	Chl*a* 2018
1	71.379	-156.954	-0.116	0.79	0.687	0.405
2	70.212	-165.688	-0.152	0.32	0.844	0.450
3	69.240	-168.783	0.052	0.75	0.617	1.562
4	68.500	-168.500	0.197	0.34	0.709	2.460
5	67.539	-167.251	0.195	0.68	0.783	1.416
6	66.938	-164.604	-0.209	0.50	2.175	2.709
7	65.703	-168.766	0.667	0.26	1.209	1.097
8	65.211	-167.811	0.599	**0.01**	1.051	1.745
9	65.303	-169.979	1.677	0.16	1.664	3.932
10	66.876	-170.083	-0.522	0.26	1.129	2.134
11	67.680	-168.958	-0.128	0.82	0.978	1.486
12	67.937	-171.748	0.139	0.30	0.656	3.302
13	69.006	-173.400	-0.024	0.89	0.838	1.000
14	68.759	-176.810	0.038	0.82	0.608	1.492
15	70.698	-168.923	-0.094	0.32	0.367	NaN

Table 4.9 Chl*a* median trend statistics for fifteen locations in September 2003-2018. Red represents positive trends and blue represents negative trends. P values in **bold** indicate statistical significance.

Location	Latitude	Longitude	Trend (mg/m^3/decade)	p value	Chl*a* 2003	Chl*a* 2018
1	71.379	-156.954	NaN	NaN	0.546	1.954
2	70.212	-165.688	0.348	**0.04**	1.062	1.709
3	69.240	-168.783	0.464	0.32	0.868	1.522
4	68.500	-168.500	0.580	**0.04**	1.113	1.726
5	67.539	-167.251	0.939	**0.005**	0.916	1.468
6	66.938	-164.604	0.747	0.12	2.236	3.149
7	65.703	-168.766	-0.074	0.82	2.662	2.650
8	65.211	-167.811	0.626	0.44	1.235	2.026
9	65.303	-169.979	0.958	**0.08**	1.384	1.384
10	66.876	-170.083	0.627	0.26	1.2442	2.143
11	67.680	-168.958	0.389	0.56	0.849	1.356
12	67.937	-171.748	0.480	0.22	0.926	1.742
13	69.006	-173.400	0.149	0.19	0.707	1.494
14	68.759	-176.810	0.327	**0.05**	0.746	1.003
15	70.698	-168.923	0.311	0.32	NaN	0.942

Chapter 5: Summary

The research presented in this dissertation adds to our knowledge of widely used methods for measuring and deriving absorption from oceanographic field samples and satellite observations, the influences of ecosystem conditions on phytoplankton community structure in the Chukchi Sea, and the application of a new tool to track trends of ecosystem-level changes in the Chukchi sea related to unprecedented warming and a decline in sea ice in this region. Chapter 1 provides a general overview of the Chukchi Sea, the environmental changes occurring therein in response to warming, and discusses the various tools that we can use to measure and track changes in the physical and chemical properties of the Chukchi Sea. Chapter 2 focuses on uncertainties related to different methods for measuring absorption and the importance of establishing uncertainty budgets for algorithms that derive inherent optical properties from satellite $R_{rs}(\lambda)$. Chapter 3 represents a deep dive into the phytoplankton ecology of the Chukchi Sea in relation to the physiochemical properties of the water column. Lastly, Chapter 4 details a proof of concept study in which the utility of recently developed satellite algorithm to measure ecosystem-level trends in the Chukchi is evaluated. A summary of the results from Chapters 2-4 is presented below.

5.1 Method closure for absorption

An important part of satellite algorithm development and validation is the collection of high quality in-water measurements. For the inherent optical property absorption, which is a derived satellite product and input parameter for various algorithms, multiple measurement methods currently exist. In Chapter 2, two methods

for measuring particle absorption, $a_p(\lambda)$, were compared in a measurement-measurement closure experiment, meaning that the uncertainties of two methods of measuring the same parameter was quantified. In the first method an ac-s measures $a_p(\lambda)$ from the water directly. The second method requires that particles are concentrated onto a filter, the absorbance of the particles is measured using a spectrophotometer, and $a_p(\lambda)$ is derived using an empirical algorithm. Within the filter pad measurements, two analytical methods, T and T-IS, each with its own set of algorithms to derive $a_p(\lambda)$ were compared. Because no material standard exists for measurements of $a_p(\lambda)$ by an ac-s or on a filter pad, the precision between all measurements was computed as a representation of uncertainty. An algorithm for modeling $a_p(\lambda)$ from Chl*a* was included within the multi-method comparison. To enrich this closure experiment, three water types were included, phytoplankton monocultures, clear open water and turbid coastal water, to determine if the precision of the measurements was influenced by the turbidity of the water samples and types of particles within the samples. Inclusion of phytoplankton monocultures allowed for comparison of different pigment types. A turbid sample includes more nonalgal particles and terrestrial input while particles in an open ocean sample consists mainly of phytoplankton.

The results of the closure experiment indicated that measurements using the T-IS method provided the best measurement precision. The T-IS method is considered the current state of the art method and thought to be the standard for filter pad measurements of $a_p(\lambda)$. However, the knowledge of the precision, or uncertainty, compared to the T method is important as historical data sets only include the T

method as the T-IS method was more recently developed. The $a_p(\lambda)$ model performed best at low Chl*a* values and should only be applied to open ocean, low Chl*a* data.

5.2 Arctic phytoplankton ecology

..Much attention is currently focused on the warming in the Arctic. Declines in sea ice extent, concentration and losses in multiyear ice have been attributed to the fact that the Arctic is warming ~2x faster than the rest of the Earth. Chapter 3 focused on the cascade effects of sea ice loss on the phytoplankton community. Phytoplankton is the base of the food web in most marine environments and, therefore, any changes in community composition could have a negative effect on the rest of the food web. Phytoplankton taxonomy measurements within the Chukchi Sea are sparse. Traditional microscopy techniques for identifying and enumerating phytoplankton cells are tedious and require a trained taxonomist. However, recent advances in flow cytometry have resulted new technologies, such as the imaging flow cytometer, which is an instrument that captures and saves images of each particle in the sample. One advantage of this technique is that the images can be saved for future annotation using computer software. Imaging flow cytometry facilitates rapid phytoplankton taxonomic data collection that results in high resolution phytoplankton taxonomic data. Chapter 3 demonstrates the utility of phytoplankton taxonomic data with the coincident collection of physiochemical water column data and sea ice extent information to explain how the environment influences phytoplankton community structure and make some inferences regarding how phytoplankton will respond to a warming Arctic system.

Using a multivariate statistics approach, the relationship between phytoplankton community structure, nutrients and sea ice became apparent. This study confirmed that the seasonal transition between different phytoplankton communities is largely driven by the ebb and flow of sea ice. Seasonal sea ice retreat initiates the spring phytoplankton bloom. The nutrients regenerated during the winter months, particularly silica along with increased light and stratification from the sea ice fuel the initial diatom-dominated bloom. As the summer progresses and sea ice retreats further north the surface waters warm, become thermally stratified and nutrients are depleted, leading to a phytoplankton community of smaller phytoplankton, like cyanobacteria and nanoeukaryotes, creating a recycling

community as opposed to the new production community like that of the spring diatom bloom. From these results, it was postulated that increased warming and sea ice loss in the Chukchi sea will result in an earlier spring diatom bloom and longer duration of the recycling community, which ultimately affects the food web.

Although the data used in Chapter 3 represents only one field campaign's worth of data, it proved the utility of having rich phytoplankton taxonomic data in addition to Chl*a,* as part of an in-depth analysis of water column ecology. This study can be further expanded upon with data collected from additional field campaigns over the course of, at least, 5-10 years. The addition of remote sensing tools would enhance a future time series study to evaluate trends in phytoplankton biomass and taxonomy in the Chukchi Sea as sea ice continues its decline and warming continues.

5.3 Remote sensing and ecosystem status

In Chapter 3, the effects of sea ice loss on the water column and phytoplankton community structure were evaluated. From that study, sea ice extent was determined to be an important driver of nutrients and physical conditions that initiate the spring diatom bloom. Earlier sea ice break-up promotes thermal stratification to occur over a longer summer season exacerbating nutrient limitation and extending the season for a recycled production-based phytoplankton community. In Chapter 4, a recently developed remote sensing tool, AVW, was applied to satellite data scenes of the Chukchi Sea during June-September 2003-2018. The advantage of the AVW algorithm is that the shape of the entire $R_{rs}(\lambda)$ spectrum is reduced to a single number that is representative of an apparent color. Because $R_{rs}(\lambda)$ is influenced by all absorbing and scattering materials in the water column, AVW can be used to

evaluate trends in the proportion of CDOM, phytoplankton and nonalgal particle absorption, which can be indicative of an ecosystem-level change, including within the phytoplankton community, in response to environmental forcings.

In this study, a red shift or a shift in the $R_{rs}(\lambda)$ spectrum peak to the red end of the visible spectrum, was observed in much of the Chukchi Sea over the 16-year study period. The red shift in AVW was correlated with an increase in satellite derived Chl*a* in all months except July when a decrease in Chl*a* was observed. As discussed in Chapter 3, an SCM, which is a common occurrence the Arctic Ocean, forms at the top of the nutricline and the 1% level of the euphotic zone once nutrients have been depleted by the phytoplankton community in the upper water column (Steiner et al. 2016). At this depth, the phytoplankton are too deep for the satellite to measure, resulting in an apparent decline in Chl*a*.

Even more interesting, the positive trend in Chl*a* in September indicated a secondary fall bloom is now occurring, which has been verified by field data. The Polar ocean typically exhibits only a phytoplankton bloom that occurs in the spring supported by the availability of nutrients and light (Sverdrup 1953). The spring bloom dissipates due to nutrient depletion and by zooplankton grazing. Both light and sea ice limit the formation of additional phytoplankton blooms over the rest of the year. The midlatitudes exhibit both a spring and fall bloom, where the spring bloom is supported by nutrients carried to the upper water column after winter mixing. The fall bloom is driven by the entrainment of nutrients into the upper ocean when the mixed layer deepens (Figure 5.1). The midlatitude fall bloom dissipates as light availability decreases as the season moves toward winter (Longhurst 1995, Martinez et al. 2011).

In the Chukchi Sea, delayed sea ice formation in the fall are likely allowing for the entrainment of nutrients into the upper water column, resembling the seasonal fall bloom of the midlatitudes. Until now, fall blooms have been unprecedented in the polar ocean. Their recent occurrence indicate that a significant ecosystem change is occurring due to longer open water duration allowing possible nutrient entrainment to occur.

Massive declines of sea ice concentrations in the Chukchi Sea were observed coincident with the trends in AVW and Chl*a* over the spring and fall months. The consequences of the observed declines in sea ice concentration are earlier sea ice break up and later sea ice formation. Trends in SST were largely not significant, likely due to the short time series of the data, although anomalies of high SSTs have been observed during the study period. These results indicate that a large-scale ecosystem alteration is occurring, which has been confirmed by field data (Grebmeier et al. 2019).

The next step was to evaluate which optically active absorbing constituent(s), i.e., nonalgal particles, phytoplankton or CDOM, are altering the water column light field. In Chapter 2, absorption was established as a major component of $R_{rs}(\lambda)$ and field measurements of absorption are vital to model development and validation. Moreover, ocean-truth measurements of absorption are important for the interpretation of $R_{rs}(\lambda)$. The results of PCA indicate that 'bluer' AVWs (~467-488 nm) were associated with the dominance of CDOM absorption while the 'redder' AVWs (~490-510 nm) were associated with the dominance of either nonalgal particles or phytoplankton absorption. Nonalgal particles are associated with riverine

input, resuspension by mixing and post-bloom conditions, when phytoplankton material breaks down and heterotrophic microbes consume these materials. An index for sea ice and Chl*a* were included in the analysis in anticipation that it would provide insight as under what conditions absorption by nonalgal particles or phytoplankton was dominant. Preliminary results indicate that absorption by nonalgal particles became dominant after sea ice retreated and, as expected, higher Chl*a* concentrations were associated with the greater phytoplankton absorption. Although this case study was limited by the available data, the analysis could be significantly strengthened by additional field data.

5.4 Conclusions

The research in this dissertation established the need to include routine measurements of phytoplankton taxonomy in the Chukchi Sea in addition to phytoplankton biomass and the utility of remote sensing tools to capture ecosystem-level trends. One additional study that could build upon this research would include phytoplankton taxonomic, environmental and optical data to relate the trends in AVW to phytoplankton community structure. For example, The Distributed Biological Observatory has collected a plethora of environmental and optical data over many years. More recently routine measurements of phytoplankton taxonomy have been added to the standard measurements for the DBO. Combined with additional information, such as phytoplankton taxonomy, the AVW algorithm could be a powerful tool to evaluate spatio-temporal ecosystem trends in $R_{rs}(\lambda)$ in the Chukchi Sea.

Chapter 5 Figures

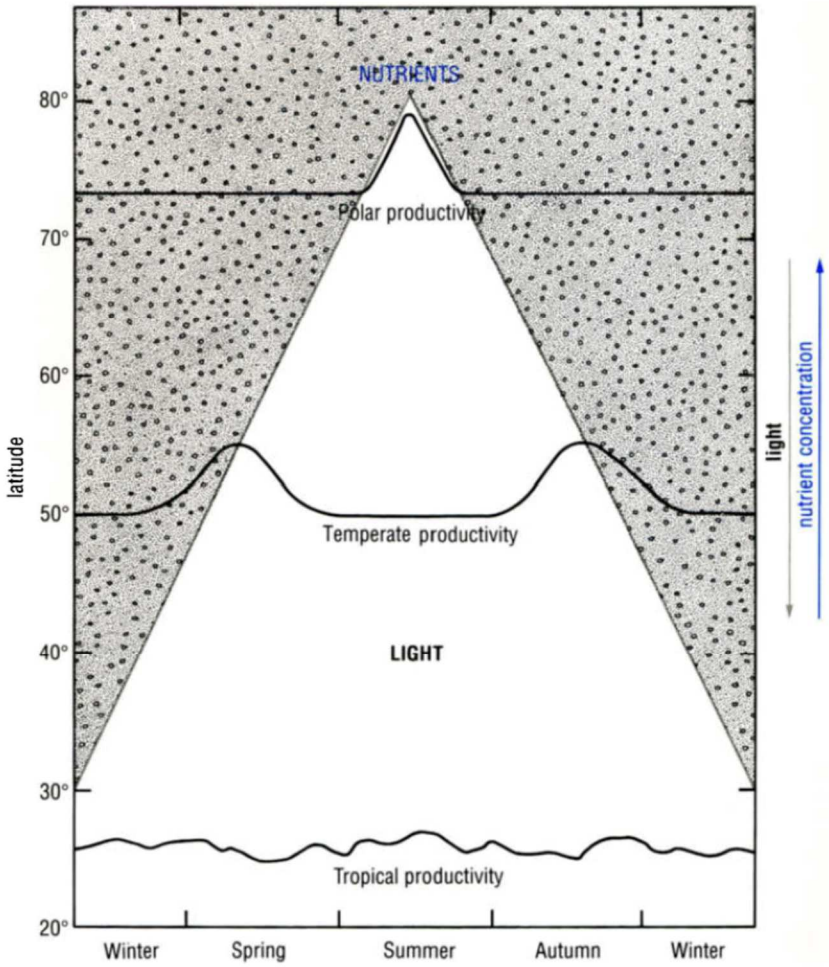

Figure 5.1 A schematic showing the relationships of nutrients and light to latitudinal seasonal cycles in primary productivity (Lalli and Parsons 1997).

Appendix 1

Supplementary text

Introduction

The supporting information includes supplementary text for the methods section the provides further detail regarding the identification and quantification of phytoplankton using the Imaging FlowCytobot (IFCB) and Accuri C6 flow cytometer and text for the results and discussion section the provides further detail regarding size class groupings of nanophytoplankton and picophytoplankton

Text A1.S1

A detailed discussion of IFCB data analysis and processing is described in Laney and Sosik (2014) and Selz et al. (2017). Briefly, microphytoplankton abundances (particles above 8 μm) were estimated using the IFCB. Digital micrographs collected by the IFCB were classified manually and by supervised machine learning. Picophytoplankton from 2-14 um were analyzed using the Accuri C6 flow cytometer. The size range of nanophytoplankton falls between 2-20um, which overlaps with the size thresholds of both the Accuri and IFCB. Therefore, the data from both instruments were merged so that smaller nanophytoplankton (2-10 μm) were estimated using data from the Accuri C6 and larger nanophytoplankton (10-20 μm) were estimated using data from the IFCB.

Text A1.S2.

It is important to note that grouping by size class does have some limitations. Because nano- and picophytoplankton combine different taxa into generic size classes, we cannot determine what taxonomic differences may have occurred between sea-ice-cover and sea-ice-free conditions. The size relationship works well between size and the same phytoplankton type. However, this relationship falls apart when different phytoplankton types are combined in the same size class (e.g., here, picoeukaryotes and cyanobacteria are categorized as picophytoplankton), as these taxa have different traits, such as nutrient requirements and function within the environment. Size class based solely on cell size, tells us little about phytoplankton taxonomy, but they can still play an important role in establishing a relationship between phytoplankton size, carbon fixation (Huete-Ortega et al., 2012) and sinking velocities (Bach et al., 2012). Although nano- and picophytoplankton are present throughout the study site, the actual species composition within these classes may be changing. Therefore, we must be cautious when interpreting size class data such as these.

Tables

Introduction

The supporting information includes tables that are referenced within the main text. These tables include the abbreviations for the phytoplankton taxonomic and environmental parameter data, summary statistics associated with the Canonical Correspondence Analysis and summary data for each environmental parameter.

Table A1.S1. Abbreviations for the phytoplankton taxonomy classifications and associated functional type or size class category.

Abbreviation	Taxon	Functional Type or Size Class	Abbreviation	Taxon	Functional Type or Size Class
Bact	*Bacteriosira*	Diatom	**Nav**	*Navicula*	Diatom
Chaet	*Chaetoceros*	Diatom	**Odon**	*Odontella*	Diatom
Cosc	*Coscinodiscus*	Diatom	**Phaeo**	*Phaeocystis*	Haptophyte
Cylin	*Cylindrotheca*	Diatom	**PhaeoD**	*Phaeocystis with* Diatoms	Diatoms attached to colonies
Deto	*Detonula*	Diatom	**Pico**	Autotrophic Picoplankton	Pico-eukaryotes and cyanobacteria
Dict	*Dictyocha*	Silicoflagellate	**Pleuro**	*Pleurosigma*	Diatom
Dinob	*Dinobryon*	Golden alga	**Polar**	*Polarella*	Dinoflagellate
Ephe	*Ephemera*	Diatom	**Pseud**	*Pseudonitzschia*	Diatom
Euc	*Eucampia*	Diatom	**Pyram**	*Pyramimonas*	Green alga
Frag	*Fragilariopsis*	Diatom	**Rhizo**	*Rhizoselenia*	Diatom
Lepto	*Leptocylindrus*	Diatom	**Thaln**	*Thalassionema*	Diatom
Melo	*Melosira*	Diatom	**Thals**	*Thalassiosira*	Diatom
Nano	Nanophytoplankton	Nano-eukaryotes	**Uncdino**	Unclassified Dinoflagellates	Dinoflagellates
Nitz	*Nitzschia frigida*	Diatom	**UncPen**	Unclassified Pennates	Diatom

Table A1.S2. Environmental variables and associated abbreviations included in CCA and PCA.

Abbreviation	Description
Density	Sigma-theta, potential density
Depth	Depth
DIN	Total Dissolved Inorganic Nitrogen (NO_3 + NO_2 + NH_4)
ICE presence	Ice index
Light	Photosynthetically available radiation
P	Phosphate
Salinity	Salinity
Si	Silicate
Temp	Temperature

Table A1.S3a. Summary statistics, significance and explained variation, determined from CCA.

	Axis				*Total Inertia*
	1	2	3	4	
Eigenvalues	0.192	0.045	0.022	0.009	
Species-environmental Correlation	0.793	0.508	0.627	0.472	0.857
Cumulative % variance of species data	22.4	27.3	29.8	30.6	
Cumulative % variance of species-environmental relationship	70.6	86.1	94.2	96.4	
Sum of all Canonical Eigenvalues					0.2612
					F=19.1 P=0.002

Table A1.S3b**.** Significance and explained variation for the Interactive stepwise CCA.

Environmental variable	**% variation explained**	**Cumulative contribution %**	**Adjusted P value**
Si	15.9	50.1	0.018
Temp	5.3	16.6	0.018
Depth	2.4	7.7	0.018
Salinity	2.5	7.8	0.018
ICE presence	1.8	5.6	0.018
Density	1.3	4.1	0.018

Table A1.S4. Mean and range of variation for each of the measured environmental variables and carbon abundance for all samples as well as those collected in regions at which each of the phytoplankton groups: PGA, PGB and PGC, were observed. Mean carbon abundances for each phytoplankton group were computed based on the clustered sample scores and associated taxon scores across the CCA axes.

Parameter	Mean and range of variation	Mean and range of variation-PGA	Mean and range of variation-PGB	Mean and range of variation-PGC
Depths sampled (m)	32.3 (1.4–202.2)	38.5 (1.9–151.6)	33.4 (2.0–108.7)	29.3 (1.4–202.2)
Fraction of surface PAR	0.246 (undet.–28.820)	0.101 (undet–1.39)	0.094 (undet.–1.28)	0.381(undet–5.918)
Chl a (mg/m^3)	3.336 (0.002–32.840)	8.093 (0.037–32.840)	7.332 (0.204 – 28.95)	0.462 (0.002–7.090)
DIN (mmol/m^3)	6.50 (undet. – 89.08)	12.00 (undet–21.88)	12.18 (undet.–63.12)	3.102 (undet–72.77)
PO_4 (mmol/m^3)	1.09 (0.01–3.86)	1.61 (0.49–2.50)	1.58 (0.54 – 2.93)	0.750 (0.01–2.52)
SiO_3 (mmol/m^3)	16.22 (0.43–59.2)	36.92 (2.71–59.2)	25.45 (0.92 – 57.81)	6.30 (0.43–42.69)
Temperature (°C)	-0.171 (-1.778 – 7.264)	-1.620 (-1.778–-0.143	-1.260 (-1.764 – 3.544)	0.906 (-1.675–7.264)
Salinity (PSU)	31.301 (24.642 – 34.556)	32.314 (29.834–34.442)	32.276 (29.784 – 33.378)	30.532 (24.642 –34.556)
SigmaT (kg/m^3)	25.098 (19.765-27.747)	25.992 (23.997–27.663)	25.948 (23.928 – 26.860)	24.410 (19.765 –27.747)
Phytoplankton Carbon (µg/L)	35.912 (0.001–1002.251)	83.980 (1.210–161.780)	99.544 (4.012 – 1002.251)	12.260 (0.002–46.280)

Appendix 2: Figures

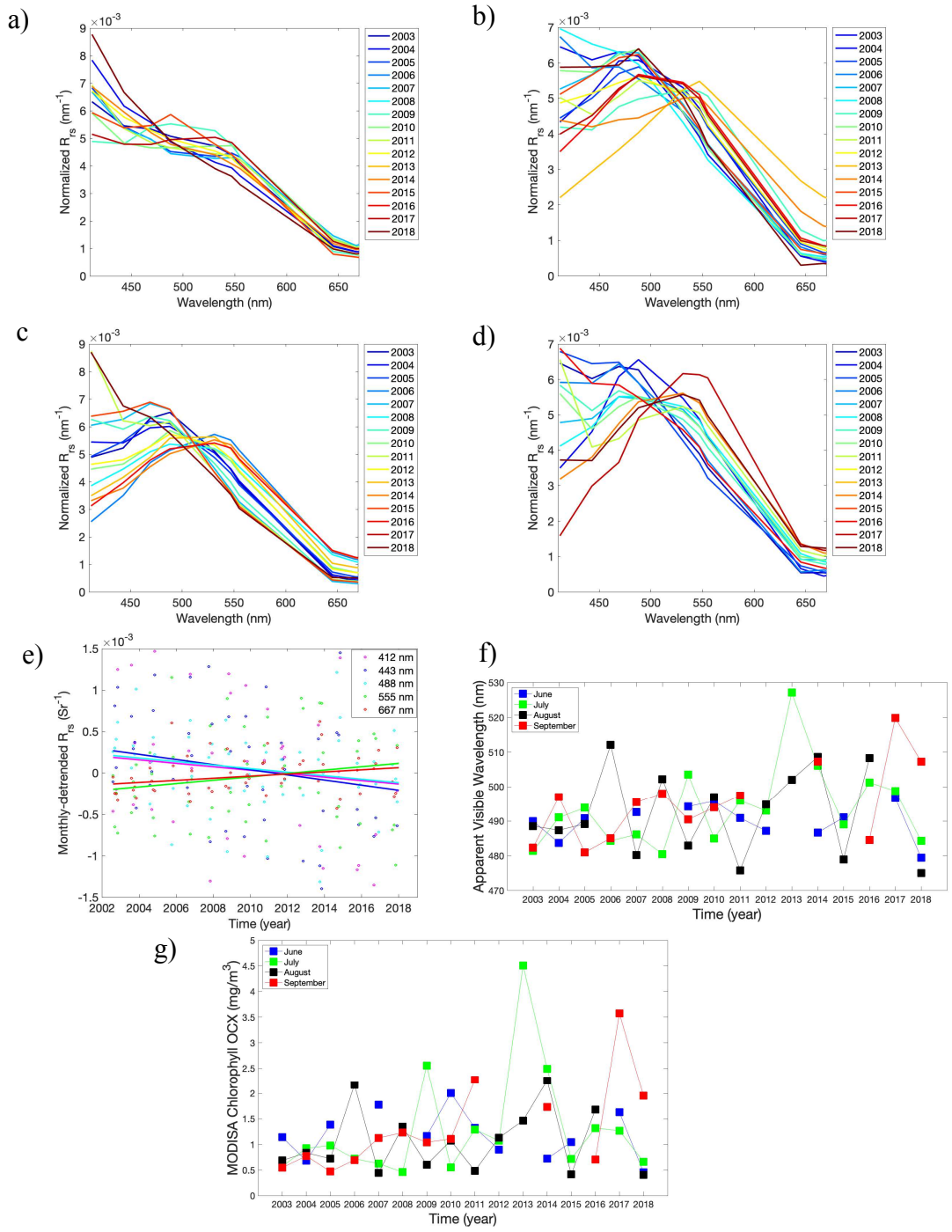

Figure A2.1. Integral-normalized $R_{rs}(\lambda)$ in plots in units of nm^{-1} for Location 1 in a) June b) July c) August and d) September. Line colors represent year of observation. e) Regression analysis plot of select $R_{rs}(\lambda)$ channels showing a significant decrease in $R_{rs}(412)$ and $R_{rs}(443)$ and a significant increase in $R_{rs}(555)$ and $R_{rs}(667)$ over the study period. f) Location 1 monthly AVW values in units of nm.
g) Location 1 monthly Chl*a* in units of mg/m^3 for June-September, 2003-2018.

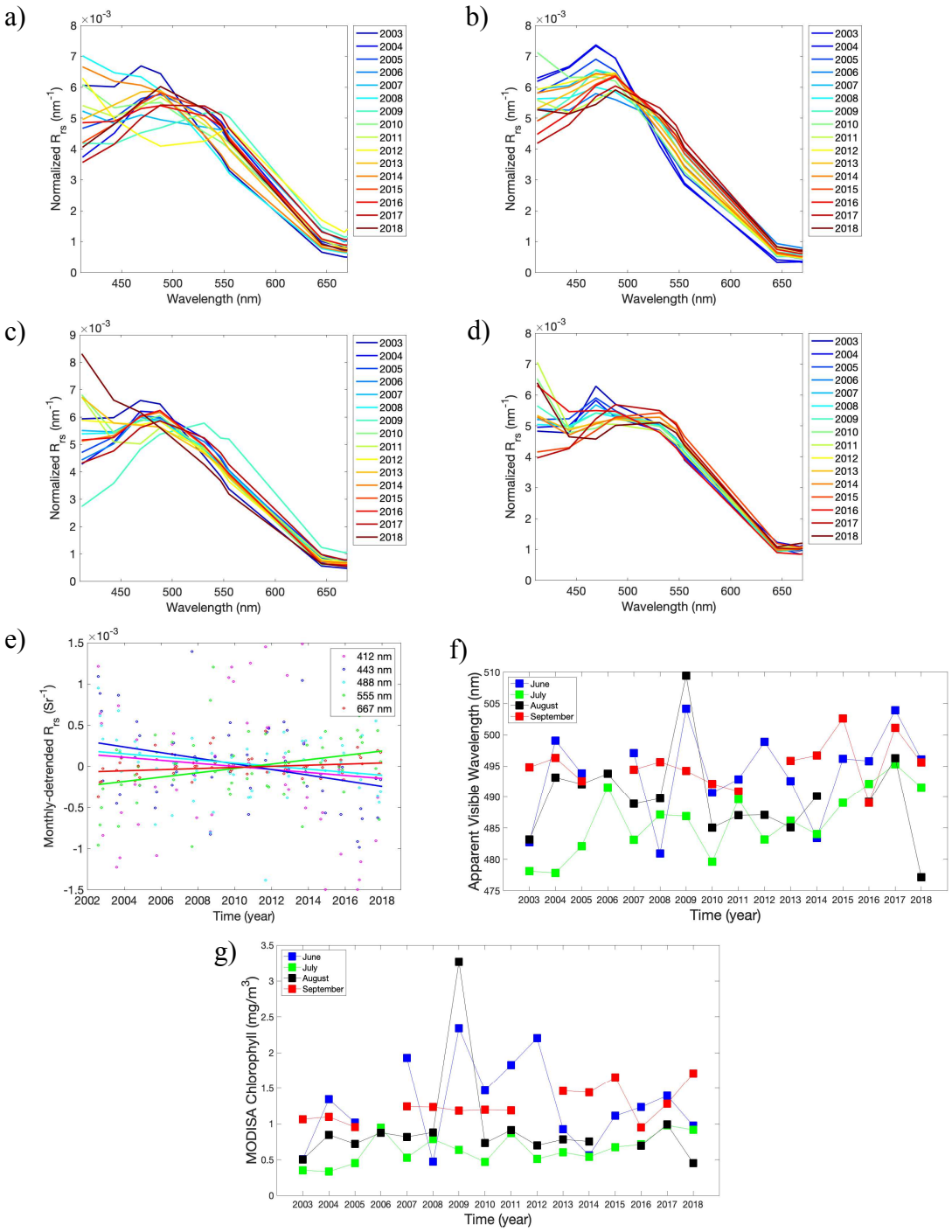

Figure A2.2. Integral-normalized $R_{rs}(\lambda)$ in plots in units of nm^{-1} for Location 2 in a) June b) July c) August and d) September. Line colors represent year of observation. e) Regression analysis plot of select $R_{rs}(\lambda)$ channels showing a significant decrease in $R_{rs}(412)$ and $R_{rs}(443)$ and a significant increase in $R_{rs}(555)$ and $R_{rs}(667)$ over the study period. f) Location 2 monthly AVW values in units of nm.
g) Location 2 monthly Chl*a* in units of mg/m^3 for June-September, 2003-2018.

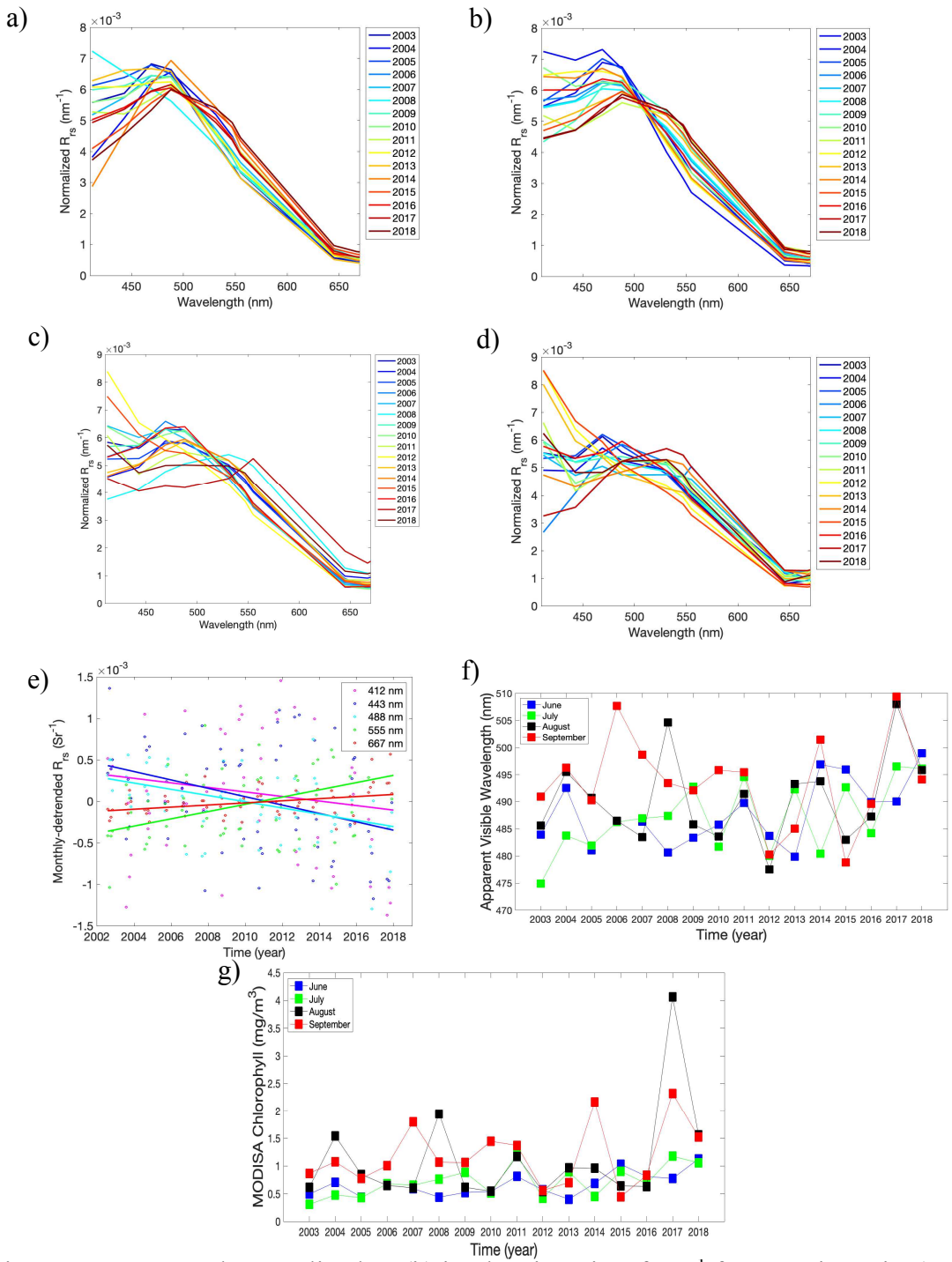

Figure A2.3. Integral-normalized $R_{rs}(\lambda)$ in plots in units of nm^{-1} for Location 3 in a) June b) July c) August and d) September. Line colors represent year of observation. e) Regression analysis plot of select $R_{rs}(\lambda)$ channels showing a significant decrease in $R_{rs}(412)$ and $R_{rs}(443)$ and a significant increase in $R_{rs}(555)$ and $R_{rs}(667)$ over the study period. f) Location 3 monthly Chl*a* in units of mg/m^3 for June-September, 2003-2018. g) Location 3 monthly AVW values in units of nm.

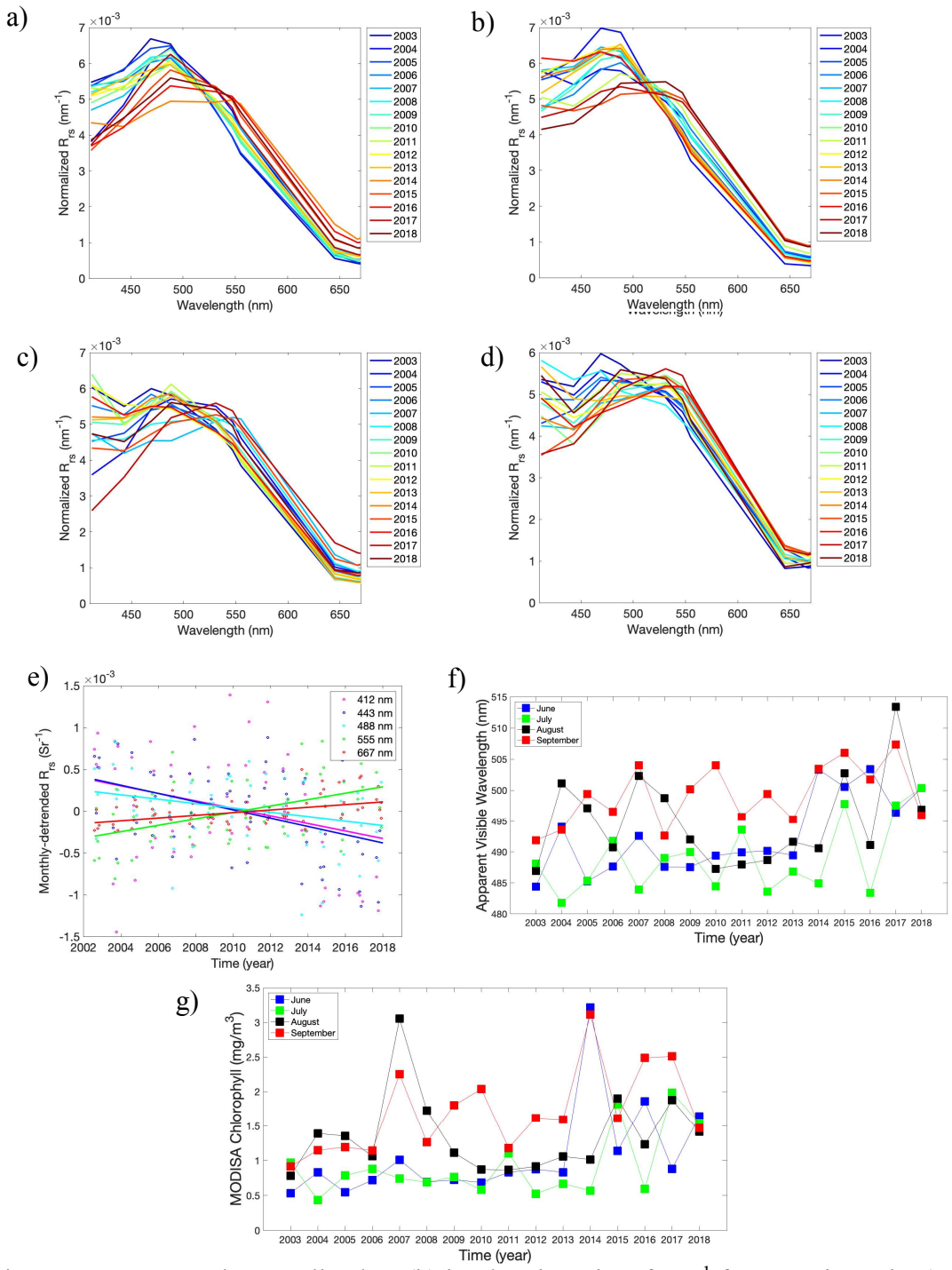

Figure A2.4. Integral-normalized $R_{rs}(\lambda)$ in plots in units of nm^{-1} for Location 5 in a) June b) July c) August and d) September. Line colors represent year of observation. e) Regression analysis plot of select $R_{rs}(\lambda)$ channels showing a significant decrease in $R_{rs}(412)$ and $R_{rs}(443)$ and a significant increase in $R_{rs}(555)$ and $R_{rs}(667)$ over the study period. f) Location 5 monthly AVW values in units of nm. g) Location 5 monthly Chl*a* in units of mg/m^3 for June-September, 2003-2018.

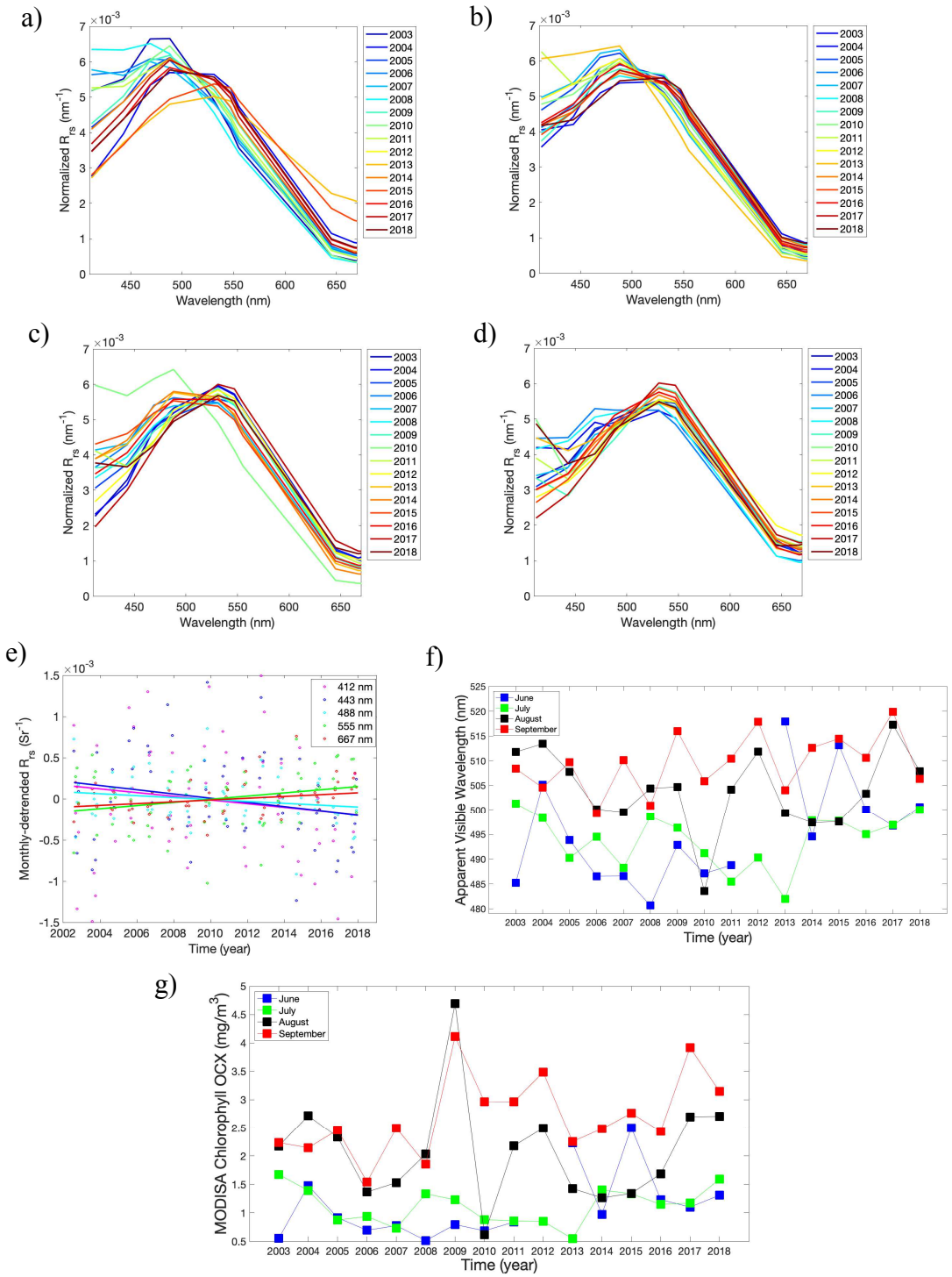

Figure A2.5. Integral-normalized $R_{rs}(\lambda)$ in plots in units of nm^{-1} for Location 6 in a) June b) July c) August and d) September. Line colors represent year of observation. e) Regression analysis plot of select $R_{rs}(\lambda)$ channels showing a significant decrease in $R_{rs}(412)$ and $R_{rs}(443)$ and a significant increase in $R_{rs}(555)$ and $R_{rs}(667)$ over the study period. f) Location 6 monthly AVW values in units of nm.
g) Location 6 monthly Chl*a* in units of mg/m^3 for June-September, 2003-2018.

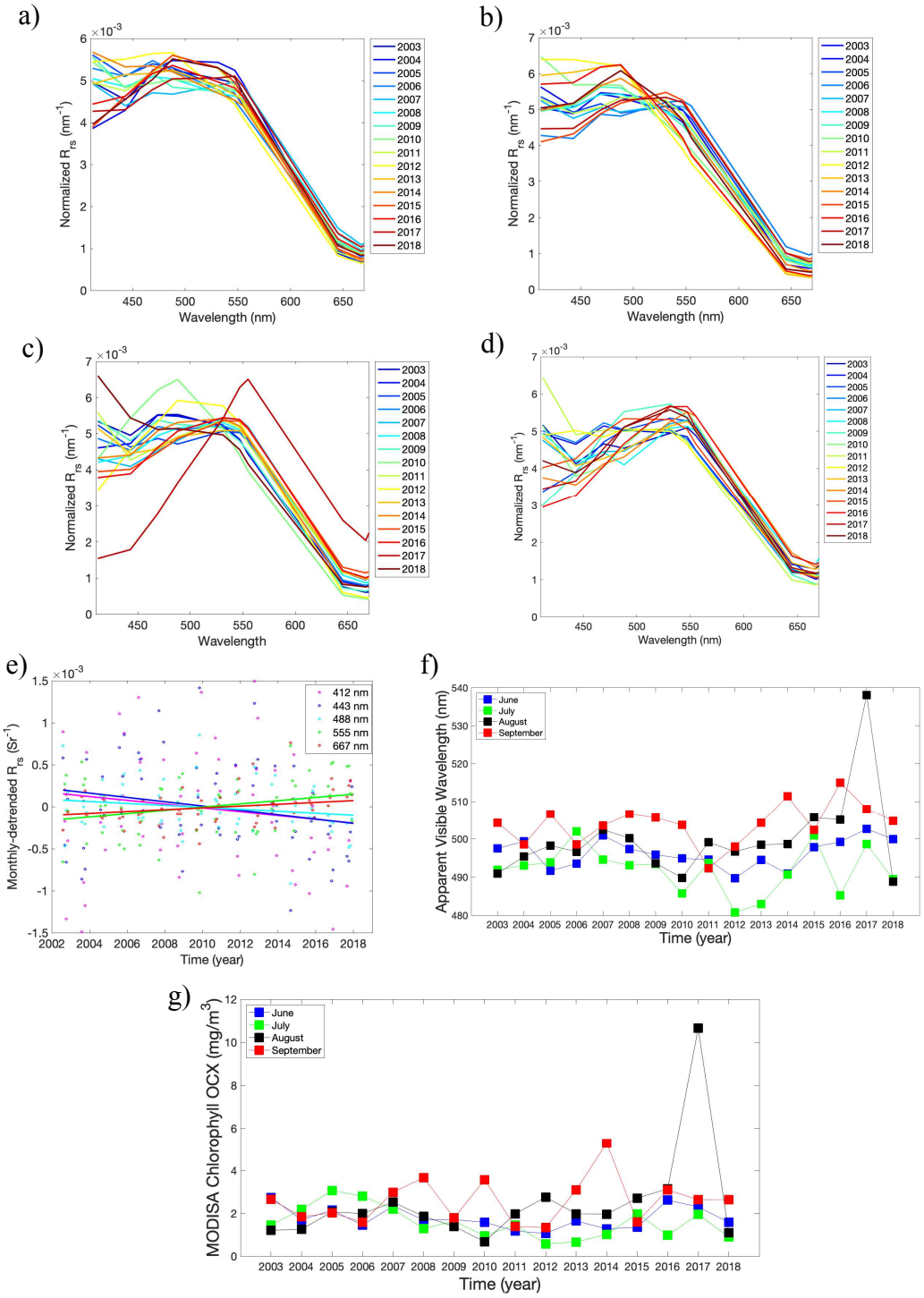

Figure A2.6. Integral-normalized $R_{rs}(\lambda)$ in plots in units of nm^{-1} for Location 7 in a) June b) July c) August and d) September. Line colors represent year of observation. e) Regression analysis plot of select $R_{rs}(\lambda)$ channels showing a significant decrease in $R_{rs}(412)$ and $R_{rs}(443)$ and a significant increase in $R_{rs}(555)$ and $R_{rs}(667)$ over the study period. f) Location 7 monthly AVW values in units of nm.
g) Location 7 monthly Chl*a* in units of mg/m^3 for June-September, 2003-2018.

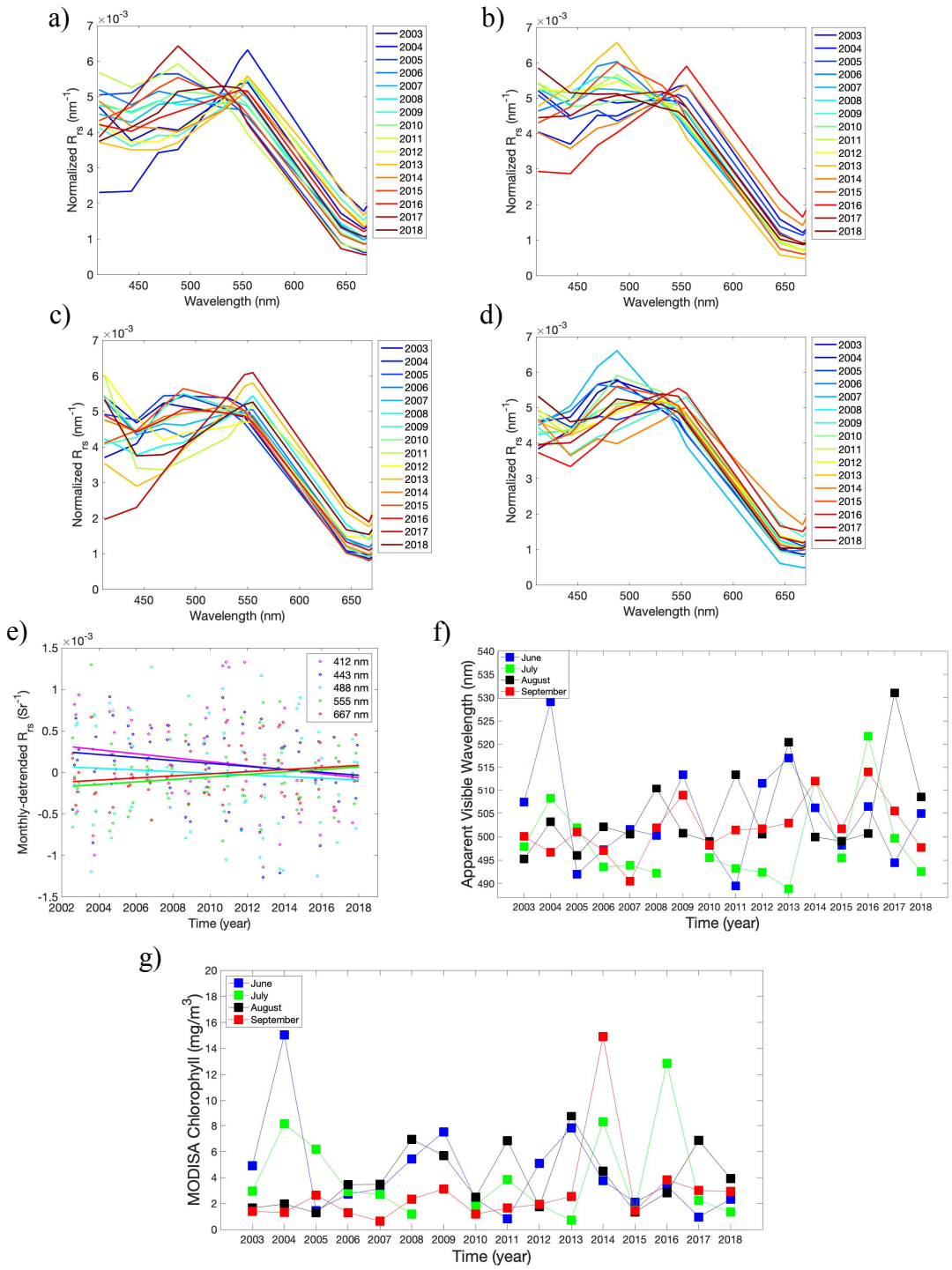

Figure A2.7. Integral-normalized $R_{rs}(\lambda)$ in plots in units of nm^{-1} for Location 9 in a) June b) July c) August and d) September. Line colors represent year of observation. e) Regression analysis plot of select $R_{rs}(\lambda)$ channels showing a significant decrease in $R_{rs}(412)$ and $R_{rs}(443)$ and a significant increase in $R_{rs}(555)$ and $R_{rs}(667)$ over the 16-year study period. f) Location 9 monthly AVW values in units of nm.
g) Location 9 monthly Chl*a* in units of mg/m^3 for June-September, 2003-2018.

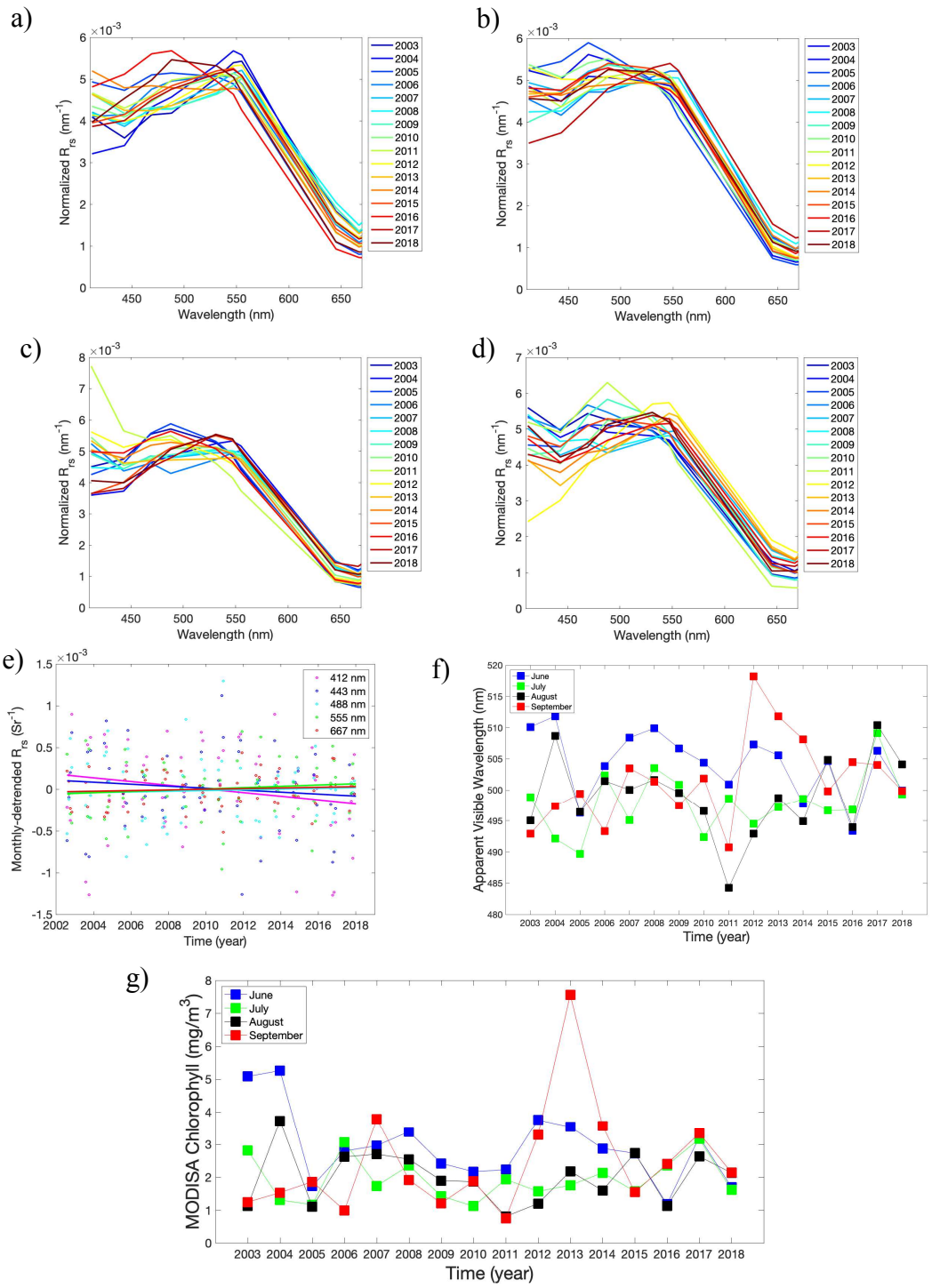

Figure A2.8. Integral-normalized $R_{rs}(\lambda)$ in plots in units of nm^{-1} for Location 10 in a) June b) July c) August and d) September. Line colors represent year of observation. e) Regression analysis plot of select $R_{rs}(\lambda)$ channels showing a significant decrease in $R_{rs}(412)$ and $R_{rs}(443)$ and a significant increase in $R_{rs}(555)$ and $R_{rs}(667)$ over the study period. f) Location 10 monthly AVW values in units of nm.
g) Location 10 monthly Chl*a* in units of mg/m^3 for June-September, 2003-2018.

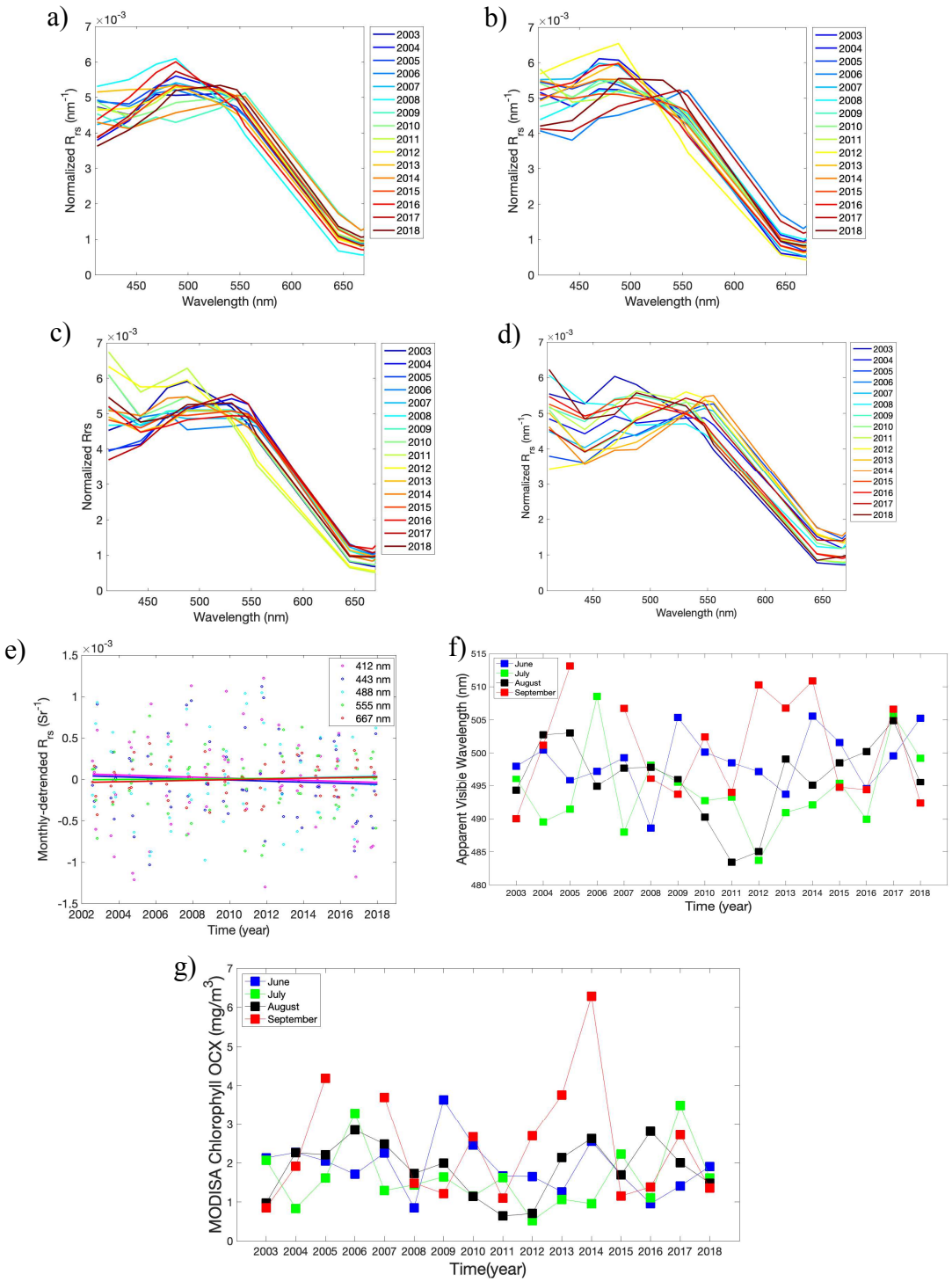

Figure A2.9. Integral-normalized $R_{rs}(\lambda)$ in plots in units of nm^{-1} for Location 11 in a) June b) July c) August and d) September. Line colors represent year of observation. e) Regression analysis plot of select $R_{rs}(\lambda)$ channels showing a significant decrease in $R_{rs}(412)$ and $R_{rs}(443)$ and a significant increase in $R_{rs}(555)$ and $R_{rs}(667)$ over the study period. f) Location 11 monthly AVW values in units of nm.
g) Location 11 monthly Chl*a* in units of mg/m^3 for June-September, 2003-2018.

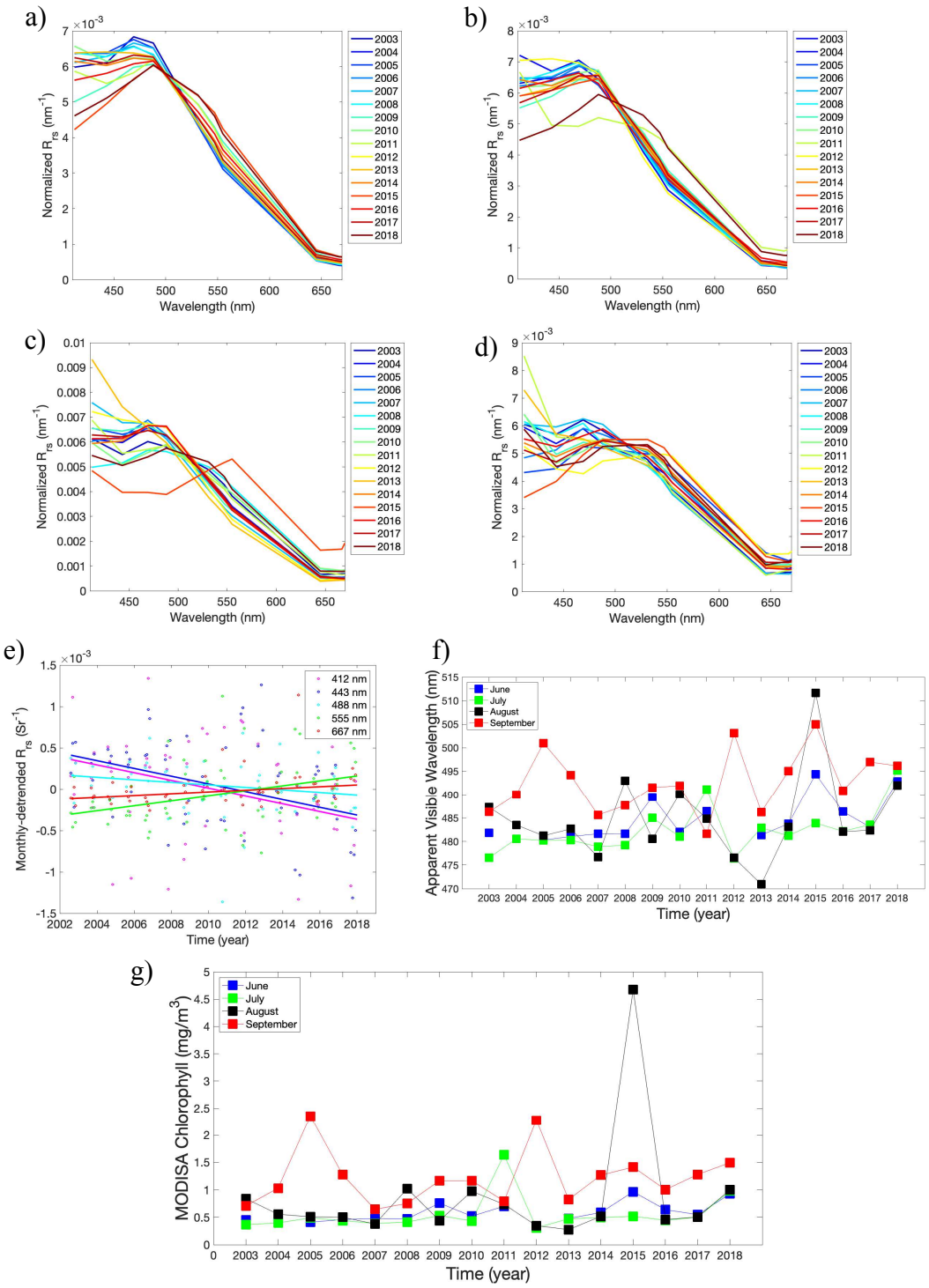

Figure A2.10. Integral-normalized $R_{rs}(\lambda)$ in plots in units of nm^{-1} for Location 13 in a) June b) July c) August and d) September. Line colors represent year of observation. e) Regression analysis plot of select $R_{rs}(\lambda)$ channels showing a significant decrease in $R_{rs}(412)$ and $R_{rs}(443)$ and a significant increase in $R_{rs}(555)$ and $R_{rs}(667)$ over the study period. f) Location 13 monthly AVW values in units of nm.
g) Location 13 monthly Chl*a* in units of mg/m^3 for June-September, 2003-2018.

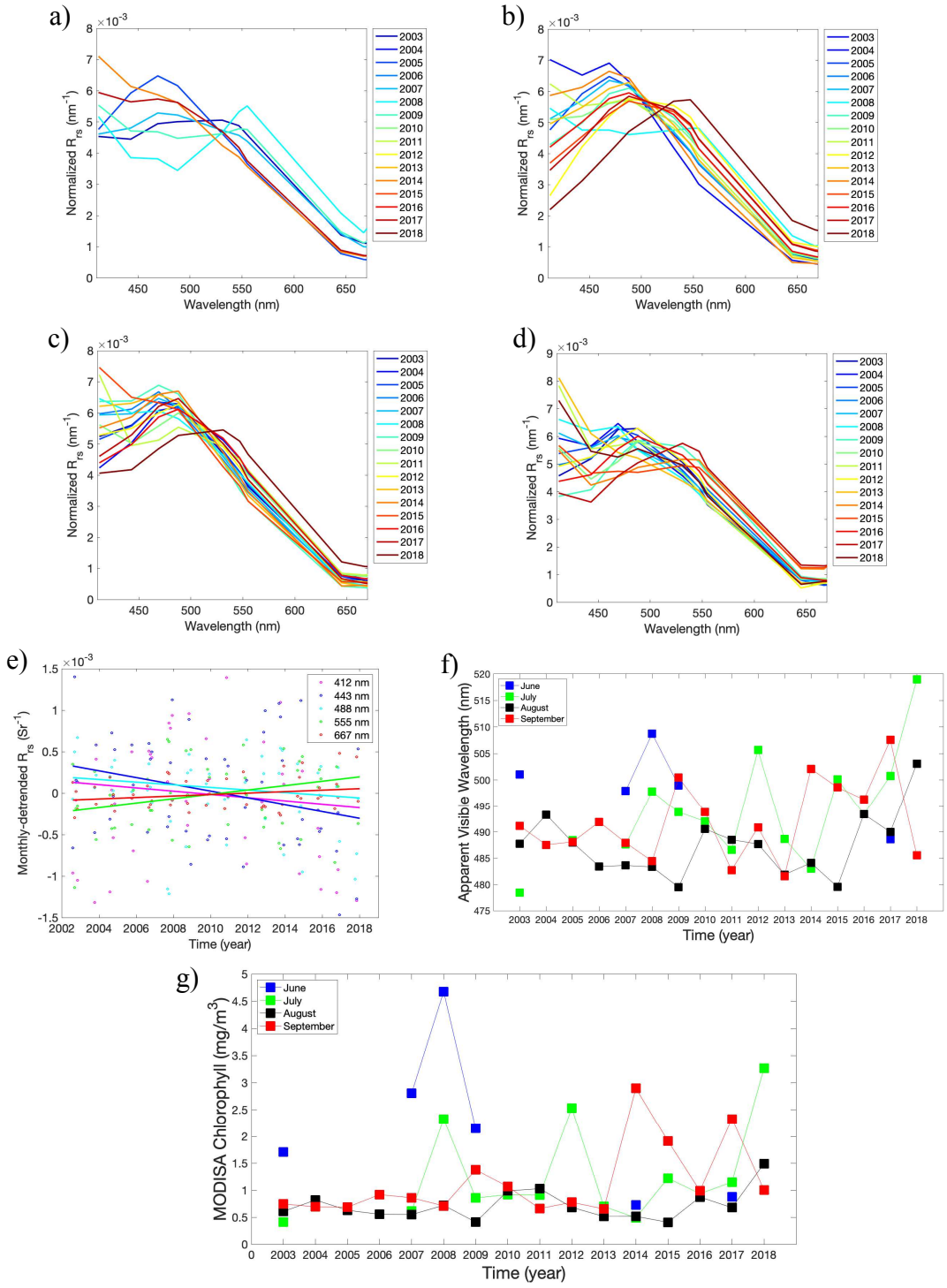

Figure A2.11. Integral-normalized $R_{rs}(\lambda)$ in plots in units of nm^{-1} for Location 14 in a) June b) July c) August and d) September. Line colors represent year of observation. e) Regression analysis plot of select $R_{rs}(\lambda)$ channels showing a significant decrease in $R_{rs}(412)$ and $R_{rs}(443)$ and a significant increase in $R_{rs}(555)$ and $R_{rs}(667)$ over the study period. f) Location 14 monthly AVW values in units of nm.
g) Location 14 monthly Chl*a* in units of mg/m^3 for June-September, 2003-2018.

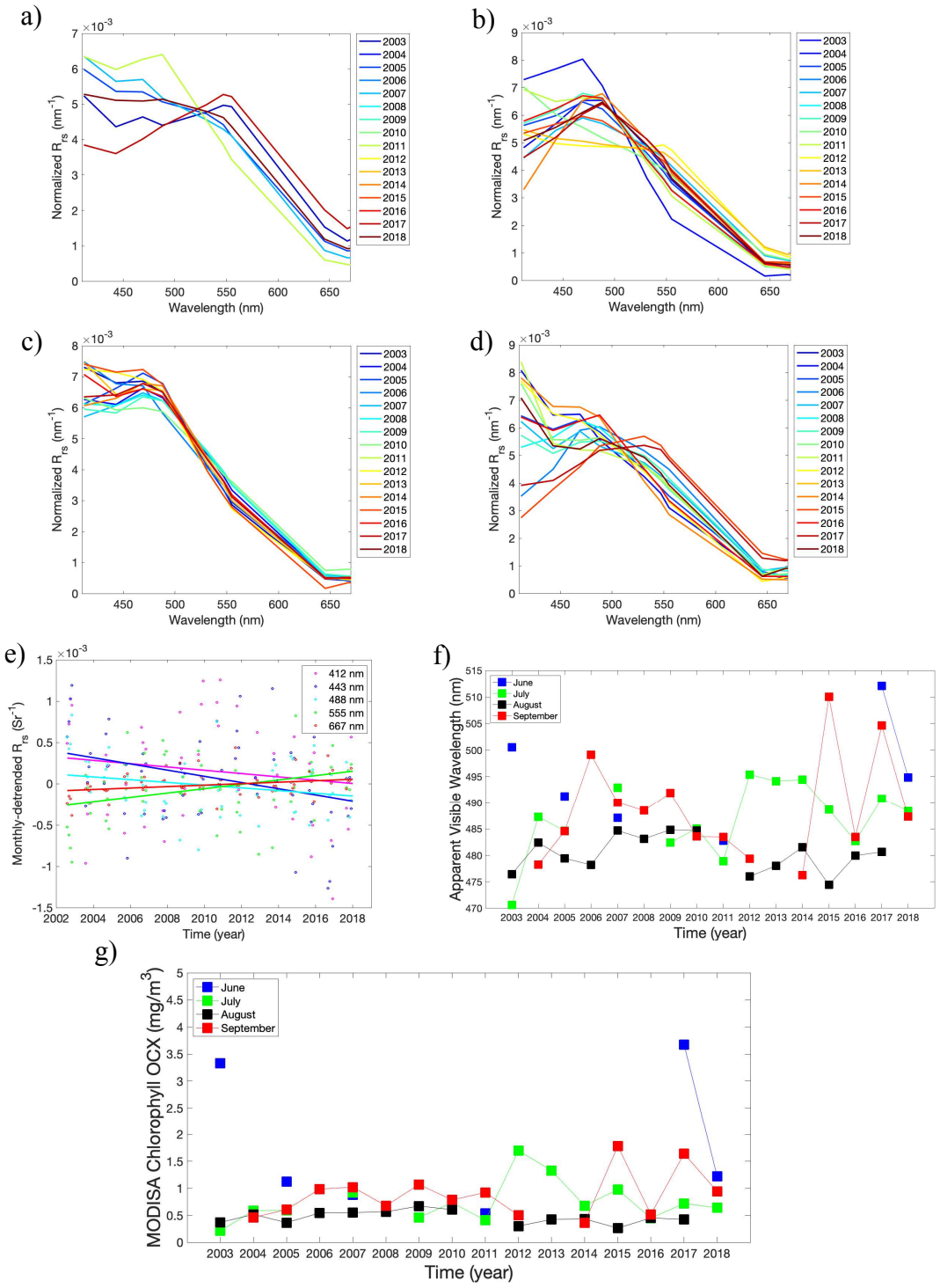

Figure A2.12. Integral-normalized $R_{rs}(\lambda)$ in plots in units of nm^{-1} for Location 15 in a) June b) July c) August and d) September. Line colors represent year of observation. e) Regression analysis plot of select $R_{rs}(\lambda)$ channels showing a significant decrease in $R_{rs}(412)$ and $R_{rs}(443)$ and a significant increase in $R_{rs}(555)$ and $R_{rs}(667)$ over the study period. f) Location 15 monthly AVW values in units of nm. g) Location 15 monthly Chl*a* in units of mg/m^3 for June-September, 2003-2018.

Appendix 3

$R_{rs}(\lambda)$ measured using ocean color instruments provides a valuable tool for monitoring ecological phenomena on a global scale. $R_{rs}(\lambda)$ magnitude and spectral shape are a direct result of the absorption and scattering constituents in the upper water column. Since the inception of ocean color instruments, scientists have developed a wide array of algorithms to derive biologically relevant products, such as chlorophyll a and phytoplankton functional types. However, uncertainties are inherent in these algorithms, as most are empirically derived, and the output of such algorithms may be biased by the samples and data from which the algorithm was developed. Moreover, algorithms developed using data from chlorophyll-driven waters (Case 1) perform poorly when applied to more optically complex (Case 2) waters, where absorption and scattering are driven not only by Chl*a* but also non-living particles and dissolved organic matter. A substantial amount of information regarding the optical signature of the ocean can be obtained directly from the $R_{rs}(\lambda)$, which typically include 5-10 different wavelengths from current satellites, and likely ~110 different wavelengths from future satellite missions such as PACE. Given these insights, how can we as oceanographers practically visualize and interpret large amounts of spectral data?

Spectral classification techniques are useful for categorizing different water types based on the apparent color. The classification techniques assume that similar $R_{rs}(\lambda)$ spectral shapes exhibit comparable absorption and scattering characteristics, thereby providing are more informative solution. The apparent visible wavelength (AVW) algorithm is a spectral classification technique that reduces 5-10 wavelengths

of ocean color data into one number that represents the optical signature or dominant color of the water (Vandermeulen et al. in review). The AVW is defined as the weighted harmonic mean of all $R_{rs}(\lambda)$ wavelengths, using the equation:

$$AVW = \frac{\sum_{i=\lambda_1}^{\lambda_n} R_{rs}(\lambda_i)}{\sum_{i=\lambda_1}^{\lambda_n} \frac{R_{rs}(\lambda_i)}{\lambda_i}} = \left(\frac{\sum_{i=\lambda_1}^{\lambda_n} \lambda_i^{-1} R_{rs}(\lambda_i)}{\sum_{i=\lambda_1}^{\lambda_n} R_{rs}(\lambda_i)} \right)^{-1}$$

Each spectrum is normalized to its trapezoidal integration, which removes the aspect of magnitude and focuses the value in spectral shape. The advantage of this method is that it is simple to compute, and the method is transparent to the user. The algorithm uses the harmonic mean instead of an arithmetic mean because the arithmetic mean would assign more weight to the higher wavelengths, i.e. because the number 650 nm is greater than 450 nm. Instead, the harmonic mean gives equal weight to all values of wavelength and, instead, interprets the intensity of the signal at each wavelength (Figure 1).

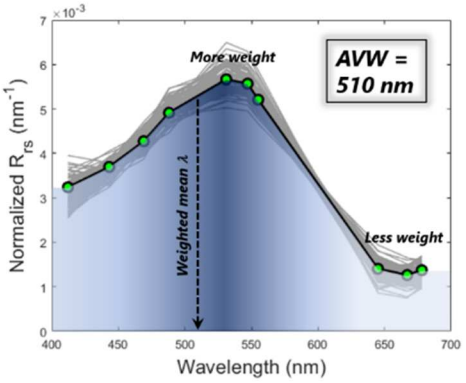

Figure A3.1 100 random spectra defined by $510 \leq AVW \leq 510.99$ nm extracted from a global MODIS-Aqua 32-day global composite (14 Sep – 15 Oct 2018) are plotted as gray lines, while the thicker black line represents the global mean of all spectra within the 510 nm AVW cluster.

The AVW output provides continuous values in units of nm that represent the optical signature of the water column and is representative the type of optically active constituents in the water and, this the spectral shape of $R_{rs}(\lambda)$. Such an indicator can be easily used in trend analyses to visualize optically driven changes that may occur in the global ocean. Vandermuelen et al. (in review) have shown that AVW can be used to explore trends in $R_{rs}(\lambda)$ over space and time. Moreover, using a set of polynomial coefficients, the authors found a method to converge AVW values derived from multiple ocean color instrument platforms.

One question was persistent throughout Chapter 4: is this trend in AVW just a manifestation of Chl*a*? My answer would be that yes, there is some influence of Chla on the AVW signal. However, I believe this is only part of the story and until we gather more field data, we cannot be sure. Chl*a* and AVW can diverge particularly in coastal or Case 2 waters that are strongly influenced by other absorbing and scattering materials, such as sediments and CDOM (Figure A3.2). The Chukchi Sea falls into this category owing to its shallow, turbid nature.

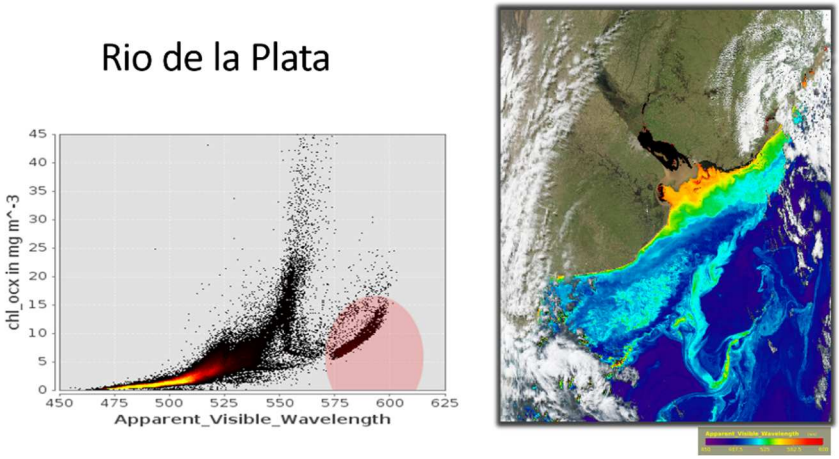

Figure A3.2 Satellite image and corresponding AVW vs. Chl*a* plot for Rio de la Plata. Note the divergence of Chl*a* and AVW within a sediment plume (red circle).

Bibliography

Ardyna, M., M. Babin, M. Gosselin, E. Devred, L. Rainville, and J. É. Tremblay. 2014. Recent Arctic Ocean sea ice loss triggers novel fall phytoplankton blooms. Geophysical Research Letters **41**:6207-6212.

Ardyna, M., M. Gosselin, C. Michel, M. Poulin, and J. Tremblay. 2011. Environmental forcing of phytoplankton community structure and function in the Canadian High Arctic contrasting oligotrophic and eutrophic regions. Marine Ecology Progress Series **442**:37-57.

Armstrong, F., C. Stearns, and J. Strickland. 1967. The measurement of upwelling and subsequent biological process by means of the Technicon Autoanalyzer® and associated equipment. Pages 381-389 *in* Deep Sea Research and Oceanographic Abstracts. Elsevier.

Arrigo, K. R. 2015. Impacts of climate on ecosystems and chemistry of the Arctic Pacific Environment (ICESCAPE). Deep-Sea Research Part II:1-6.

Arrigo, K. R., D. K. Perovich, R. S. Pickart, Z. W. Brown, G. L. van Dijken, K. E. Lowry, M. M. Mills, M. A. Palmer, W. M. Balch, and N. R. Bates. 2014. Phytoplankton blooms beneath the sea ice in the Chukchi Sea. Deep Sea Research Part II: Topical Studies in Oceanography **105**:1-16.

Arrigo, K. R., and G. L. van Dijken. 2015. Continued increases in Arctic Ocean primary production. Progress in Oceanography **136**:60-70.

Babin, M., D. J. L. Stramski, and Oceanography. 2002. Light absorption by aquatic particles in the near-infrared spectral region. **47**:911-915.

Baker, A. C., P. W. Glynn, and B. Riegl. 2008. Climate change and coral reef bleaching: An ecological assessment of long-term impacts, recovery trends and future outlook. Estuarine, coastal and shelf science **80**:435-471.

Behrenfeld, M. J., E. Boss, D. A. Siegel, and D. M. Shea. 2005. Carbon-based ocean productivity and phytoplankton physiology from space. Global Biogeochemical Cycles **19**.

Bélanger, S., M. Babin, and P. Larouche. 2008. An empirical ocean color algorithm for estimating the contribution of chromophoric dissolved organic matter to total light absorption in optically complex waters. Journal of Geophysical Research: Oceans **113**.

Bernhardt, H., and A. Wilhelms. 1967. The continuous determination of low level iron, soluble phosphate and total phosphate with the AutoAnalyzer. Pages 385-389 *in* Technicon Symposia.

Blanchard, A. L., R. H. Day, A. E. Gall, L. A. Aerts, J. Delarue, E. L. Dobbins, R. R. Hopcroft, J. M. Questel, T. J. Weingartner, and S. S. Wisdom. 2017. Ecosystem variability in the offshore northeastern Chukchi Sea. Progress in Oceanography **159**:130-153.

Boss, E., A. M. Waite, J. Uitz, S. G. Acinas, H. M. Sosik, K. Fennel, I. Berman-Frank, M. Cornejo, S. Thomalla, and H. Yamazaki. 2020. Recommendations for plankton measurements on the GO-SHIP program with relevance to other sea-going expeditions. SCOR Working Group 154 GO-SHIP Report.

Bricaud, A. 2013.

Bricaud, A., A. Morel, M. Babin, K. Allali, and H. Claustre. 1998. Variations of light absorption by suspended particles with chlorophyll a concentration in oceanic (case 1) waters: Analysis and implications for bio-optical models. Journal of Geophysical Research: Oceans **103**:31033-31044.

Bricaud, A., and D. Stramski. 1990. Spectral absorption coefficients of living phytoplankton and nonalgal biogenous matter: A comparison between the Peru upwelling areaand the Sargasso Sea. Limnology and oceanography **35**:562-582.
Brown, Z. W., K. E. Lowry, M. A. Palmer, G. L. van Dijken, M. M. Mills, R. S. Pickart, and K. R. Arrigo. 2015. Characterizing the subsurface chlorophyll a maximum in the Chukchi Sea and Canada Basin. Deep Sea Research Part II: Topical Studies in Oceanography **118**:88-104.
Brugler, E. T., R. S. Pickart, G. Moore, S. Roberts, T. J. Weingartner, and H. Statscewich. 2014. Seasonal to interannual variability of the Pacific water boundary current in the Beaufort Sea. Progress in Oceanography **127**:1-20.
Butler, W. L. 1962. Absorption of light by turbid materials. JOSA **52**:292-299.
Cai, W.-J., L. Chen, B. Chen, Z. Gao, S. H. Lee, J. Chen, D. Pierrot, K. Sullivan, Y. Wang, and X. Hu. 2010. Decrease in the CO2 uptake capacity in an ice-free Arctic Ocean basin. Science **329**:556-559.
Carmack, E. C. 2007. The alpha/beta ocean distinction: A perspective on freshwater fluxes, convection, nutrients and productivity in high-latitude seas. Deep Sea Research Part II: Topical Studies in Oceanography **54**:2578-2598.
Cavalieri, D. J., C. L. Parkinson, N. DiGirolamo, and A. Ivanoff. 2011. Intersensor calibration between F13 SSMI and F17 SSMIS for global sea ice data records. IEEE Geoscience Remote Sensing Letters **9**:233-236.
Cetinic, I., C. R. McClain, P. J. Werdell, Z. Ahmad, Z. Ahmad, R. Arnone, M. J. Behrenfeld, B. Cairns, I. Cetini, and R. E. Eplee. 2018. PACE Technical Report Series, Volume 7: Ocean Color Instrument (OCI) Concept Design Studies.
Chase, A., E. Boss, R. Zaneveld, A. Bricaud, H. Claustre, J. Ras, G. Dall'Olmo, and T. K. Westberry. 2013. Decomposition of in situ particulate absorption spectra. Methods in Oceanography **7**:110-124.
Chaves, J. E., P. J. Werdell, C. W. Proctor, A. R. Neeley, S. A. Freeman, C. S. Thomas, and S. B. Hooker. 2015. Assessment of ocean color data records from MODIS-Aqua in the western Arctic Ocean. Deep Sea Research Part II: Topical Studies in Oceanography **118**:32-43.
Chavez, F. P., K. R. Buck, R. R. Bidigare, D. M. Karl, D. Hebel, M. Latasa, L. Campbell, and J. Newton. 1995. On the chlorophyll a retention properties of glass-fiber GF/F filters. Limnology and oceanography **40**:428-433.
Ciotti, A. M., and A. Bricaud. 2006. Retrievals of a size parameter for phytoplankton and spectral light absorption by colored detrital matter from water-leaving radiances at SeaWiFS channels in a continental shelf region off Brazil. Limnology and Oceanography: Methods **4**:237-253.
Ciotti, A. M., M. R. Lewis, and J. J. Cullen. 2002. Assessment of the relationships between dominant cell size in natural phytoplankton communities and the spectral shape of the absorption coefficient. Limnology and oceanography **47**:404-417.
Coachman, L., and K. Aagaard. 1988. Transports through Bering Strait: Annual and interannual variability. Journal of Geophysical Research: Oceans **93**:15535-15539.
Constable, A. J., D. P. Costa, O. Schofield, L. Newman, E. R. Urban Jr, E. A. Fulton, J. Melbourne-Thomas, T. Ballerini, P. W. Boyd, and A. Brandt. 2016. Developing priority variables ("ecosystem Essential Ocean Variables"—eEOVs) for observing dynamics and change in Southern Ocean ecosystems. Journal of Marine Systems **161**:26-41.
Darnis, G., D. Robert, C. Pomerleau, H. Link, P. Archambault, R. J. Nelson, M. Geoffroy, J.-É. Tremblay, C. Lovejoy, and S. H. Ferguson. 2012. Current state and trends in

Canadian Arctic marine ecosystems: II. Heterotrophic food web, pelagic-benthic coupling, and biodiversity. Climatic Change **115**:179-205.
De Robertis, A., N. Lawrence-Slavas, R. Jenkins, I. Wangen, C. W. Mordy, C. Meinig, M. Levine, D. Peacock, and H. Tabisola. 2019. Long-term measurements of fish backscatter from Saildrone unmanned surface vehicles and comparison with observations from a noise-reduced research vessel. ICES Journal of Marine Science **76**:2459-2470.
Del Castillo, C., S. Platnick, and D. Antoine. 2012. Pre-Aerosol, Clouds, and ocean Ecosystem (PACE) Mission science definition team report. Pages 16-19 *in* Proceedings of the Ocean Carbon and Biogeochemistry Workshop, Woods Hole, MA, USA.
Del Castillo, C. E., S. R. Signorini, E. M. Karaköylü, and S. Rivero-Calle. 2019. Is the Southern Ocean getting greener? Geophysical Research Letters **46**:6034-6040.
Devred, E., S. Sathyendranath, V. Stuart, and T. Platt. 2011. A three component classification of phytoplankton absorption spectra: Application to ocean-color data. Remote Sensing of Environment **115**:2255-2266.
Dutkiewicz, S., A. Hickman, O. Jahn, W. Gregg, C. Mouw, and M. Follows. 2015. Capturing optically important constituents and properties in a marine biogeochemical and ecosystem model. Biogeosciences **12**:4447-4481.
Dutkiewicz, S., A. E. Hickman, O. Jahn, S. Henson, C. Beaulieu, and E. Monier. 2019. Ocean colour signature of climate change. Nature Communications **10**:1-13.
Eisner, L. 2019. The Bering Sea: Current status and recent trends. PICES Press **27**:33-35,39.
Frey, K., J. Comiso, L. Cooper, J. Grebmeier, and L. Stock. 2019. Arctic Ocean Primary Productivity: The Response of Marine Algae to Climate Warming and Sea Ice Decline.
Frey, K. E., J. A. Maslanik, J. C. Kinney, and W. Maslowski. 2014. Recent variability in sea ice cover, age, and thickness in the Pacific Arctic region. Pages 31-63 The Pacific Arctic Region. Springer.
Frey, K. E., G. Moore, L. W. Cooper, and J. M. Grebmeier. 2015. Divergent patterns of recent sea ice cover across the Bering, Chukchi, and Beaufort seas of the Pacific Arctic Region. Progress in Oceanography **136**:32-49.
Fripiat, F., D. Cardinal, J. L. Tison, A. Worby, and L. André. 2007. Diatom-induced silicon isotopic fractionation in Antarctic sea ice. Journal of Geophysical Research: Biogeosciences **112**.
Fripiat, F., J.-L. Tison, L. André, D. Notz, and B. Delille. 2014. Biogenic silica recycling in sea ice inferred from Si-isotopes: constraints from Arctic winter first-year sea ice. Biogeochemistry **119**:25-33.
Garaba, S. P., A. Friedrichs, D. Voß, and O. Zielinski. 2015. Classifying natural waters with the Forel-Ule Colour index system: results, applications, correlations and crowdsourcing. International Journal of Environmental Research and Public Health **12**:16096-16109.
Gentemann, G. L., J. P. Scott, P. L. F. Mazzini, C. Pianca, S. Akella, P. J. Minnett, P. Cornillon, B. Fox-Kemper, I. Cetinić, T. M. Chin, J. Gomez-Valdes, J. Vazquez-Cuervo, V. Tsontos, L. Yu, R. Jenkins, S. De Halleux, D. Peacock, and N. Cohen. 2020. Saildrone: adaptively sampling the marine environment. Bulletin of the American Meteorological Society.
Glibert, P. M. 2016. Margalef revisited: A new phytoplankton mandala incorporating twelve dimensions, including nutritional physiology. Harmful Algae **55**:25-30.

Goethel, C. L., J. M. Grebmeier, and L. W. Cooper. 2019. Changes in abundance and biomass of the bivalve Macoma calcarea in the northern Bering Sea and the southeastern Chukchi Sea from 1998 to 2014, tracked through dynamic factor analysis models. Deep Sea Research Part II: Topical Studies in Oceanography **162**:127-136.

Gradinger, R. 2009. Sea-ice algae: Major contributors to primary production and algal biomass in the Chukchi and Beaufort Seas during May/June 2002. Deep Sea Research Part II: Topical Studies in Oceanography **56**:1201-1212.

Grebmeier, J. M. 2012. Shifting patterns of life in the Pacific Arctic and sub-Arctic seas. Annual Review of Marine Science **4**:63-78.

Grebmeier, J. M., B. A. Bluhm, L. W. Cooper, S. L. Danielson, K. R. Arrigo, A. L. Blanchard, J. T. Clarke, R. H. Day, K. E. Frey, and R. R. Gradinger. 2015. Ecosystem characteristics and processes facilitating persistent macrobenthic biomass hotspots and associated benthivory in the Pacific Arctic. Progress in Oceanography **136**:92-114.

Grebmeier, J. M., L. W. Cooper, H. M. Feder, and B. I. Sirenko. 2006a. Ecosystem dynamics of the Pacific-influenced northern Bering and Chukchi Seas in the Amerasian Arctic. Progress in Oceanography **71**:331-361.

Grebmeier, J. M., K. E. Frey, L. W. Cooper, and M. Kędra. 2018. Trends in benthic macrofaunal populations, seasonal sea ice persistence, and bottom water temperatures in the Bering Strait region. Oceanography **31**:136-151.

Grebmeier, J. M., and W. Maslowski. 2014. The Pacific Arctic Region: An Introduction. Pages 1-15 *in* J. M. Grebmeier and W. Maslowski, editors. The Pacific Arctic Region: Ecosystem Status and Trends in a Rapidly Changing Environment. Springer Dordrecht.

Grebmeier, J. M., and C. P. McRoy. 1989. Pelagic-benthic coupling on the shelf of the northern Bering and Chukchi Seas. III. Benthic food supply and carbon cycling. Marine Ecology Progress Series **53**:79-91.

Grebmeier, J. M., S. E. Moore, L. W. Cooper, and K. E. Frey. 2019. The Distributed Biological Observatory: A change detection array in the Pacific Arctic–An introduction. Deep-Sea Research Part II **162**:1-7.

Grebmeier, J. M., J. E. Overland, S. E. Moore, E. V. Farley, E. C. Carmack, L. W. Cooper, K. E. Frey, J. H. Helle, F. A. McLaughlin, and S. L. McNutt. 2006b. A major ecosystem shift in the northern Bering Sea. Science **311**:1461-1464.

Groom, S., S. Sathyendranath, Y. Ban, S. Bernard, R. Brewin, V. Brotas, C. Brockmann, P. Chauhan, J.-k. Choi, A. Chuprin, S. Ciavatta, P. Cipollini, C. Donlon, B. Franz, X. He, T. Hirata, T. Jackson, M. Kampel, H. Krasemann, S. Lavender, S. Pardo-Martinez, F. Mélin, T. Platt, R. Santoleri, J. Skakala, B. Schaeffer, M. Smith, F. Steinmetz, A. Valente, and M. Wang. 2019. Satellite Ocean Colour: Current Status and Future Perspective. **6**.

Hill, V., M. Ardyna, S. H. Lee, and D. E. Varela. 2017. Decadal trends in phytoplankton production in the Pacific Arctic Region from 1950 to 2012. Deep Sea Research Part II: Topical Studies in Oceanography.

Hill, V., M. Ardyna, S. H. Lee, and D. E. Varela. 2018. Decadal trends in phytoplankton production in the Pacific Arctic Region from 1950 to 2012. Deep Sea Research Part II: Topical Studies in Oceanography **152**:82-94.

Hill, V., and G. Cota. 2005. Spatial patterns of primary production on the shelf, slope and basin of the Western Arctic in 2002. Deep Sea Research Part II: Topical Studies in Oceanography **52**:3344-3354.

Hill, V., G. Cota, and D. Stockwell. 2005. Spring and summer phytoplankton communities in the Chukchi and Eastern Beaufort Seas. Deep Sea Research Part II: Topical Studies in Oceanography **52**:3369-3385.

Hoaglin, D. C., F. Mosteller, J. W. J. W. S. i. P. Tukey, N. Y. W. Mathematical Statistics, , edited by Hoaglin, David C., F. Mosteller, and J. W. Tukey. 1983. Understanding robust and exploratory data anlysis.

Hoepffner, N., and S. Sathyendranath. 1992. Bio-optical characteristics of coastal waters: Absorption spectra of phytoplankton and pigment distribution in the western North Atlantic. Limnology and oceanography **37**:1660-1679.

Hooker, S. B., L. Van Heukelem, C. S. Thomas, H. Claustre, J. Ras, R. Barlow, H. Sessions, L. Schlüter, J. Perl, and C. Trees. 2005. The second SeaWiFS HPLC analysis round-robin experiment (SeaHARRE-2). NASA Tech. Memo **212785**:124.

Hunter-Cevera, K. R., M. G. Neubert, R. J. Olson, A. R. Solow, A. Shalapyonok, and H. M. Sosik. 2016. Physiological and ecological drivers of early spring blooms of a coastal phytoplankter. Science **354**:326-329.

Kahru, M., Z. Lee, B. G. Mitchell, and C. D. J. B. l. Nevison. 2016. Effects of sea ice cover on satellite-detected primary production in the Arctic Ocean. **12**:20160223.

Kérouel, R., and A. Aminot. 1997. Fluorometric determination of ammonia in sea and estuarine waters by direct segmented flow analysis. Marine Chemistry **57**:265-275.

Kishino, M., M. Takahashi, N. Okami, and S. J. B. o. m. s. Ichimura. 1985. Estimation of the spectral absorption coefficients of phytoplankton in the sea. **37**:634-642.

Lalli, C., and T. R. Parsons. 1997. Chapter 3: Phytoplankton and primary productivity. Biological oceanography: an introduction. Elsevier.

Laney, S. R., and H. M. Sosik. 2014. Phytoplankton assemblage structure in and around a massive under-ice bloom in the Chukchi Sea. Deep Sea Research Part II: Topical Studies in Oceanography **105**:30-41.

Lee, S. H., T. E. Whitledge, and S.-H. Kang. 2007. Recent carbon and nitrogen uptake rates of phytoplankton in Bering Strait and the Chukchi Sea. Continental shelf research **27**:2231-2249.

Lee, Z., K. L. Carder, and R. A. Arnone. 2002. Deriving inherent optical properties from water color: a multiband quasi-analytical algorithm for optically deep waters. Applied Optics **41**:5755-5772.

Lee, Z., J. Wei, K. Voss, M. Lewis, A. Bricaud, and Y. Huot. 2015. Hyperspectral absorption coefficient of "pure" seawater in the range of 350–550 nm inverted from remote sensing reflectance. Applied Optics **54**:546-558.

Li, W. K., F. A. McLaughlin, C. Lovejoy, and E. C. Carmack. 2009. Smallest algae thrive as the Arctic Ocean freshens. Science **326**:539-539.

Lindstrom, E., J. Gunn, A. Fischer, A. McCurdy, and L. Glover. 2012. A Framework for Ocean Observing. By the Task Team for an Integrated Framework for Sustained Ocean Observing.

Lohrenz, S. E. 2000. A novel theoretical approach to correct for pathlength amplification and variable sampling loading in measurements of particulate spectral absorption by the quantitative filter technique. Journal of Plankton Research **22**:639-657.

Longhurst, A. 1995. Seasonal cycles of pelagic production and consumption. Progress in Oceanography **36**:77-167.

Lowry, K. E., R. S. Pickart, M. M. Mills, Z. W. Brown, G. L. van Dijken, N. R. Bates, and K. R. Arrigo. 2015. The influence of winter water on phytoplankton blooms in the

Chukchi Sea. Deep Sea Research Part II: Topical Studies in Oceanography **118**:53-72.
Margalef, R. 1978. Life-forms of phytoplankton as survival alternatives in an unstable environment. Oceanologica acta **1**:493-509.
Maritorena, S., D. A. Siegel, and A. R. Peterson. 2002. Optimization of a semianalytical ocean color model for global-scale applications. Applied Optics **41**:2705-2714.
Martinez, E., D. Antoine, F. D'Ortenzio, and C. de Boyer Montégut. 2011. Phytoplankton spring and fall blooms in the North Atlantic in the 1980s and 2000s. Journal of Geophysical Research: Oceans **116**.
Maske, H., and H. Haardt. 1987. Quantitative in vivo absorption spectra of phytoplankton: Detrital absorption and comparison with fluorescence excitation spectra 1. Limnology and oceanography **32**:620-633.
Maslanik, J., J. Stroeve, C. Fowler, and W. Emery. 2011. Distribution and trends in Arctic sea ice age through spring 2011. Geophysical Research Letters **38**.
Mathis, J. T., J. M. Grebmeier, D. A. Hansell, R. R. Hopcroft, D. L. Kirchman, S. H. Lee, S. B. Moran, N. R. Bates, S. VanLaningham, and J. N. Cross. 2014. Carbon biogeochemistry of the western Arctic: Primary production, carbon export and the controls on ocean acidification. Pages 223-268 The Pacific Arctic Region. Springer.
Matsuoka, A., E. Ortega-Retuerta, A. Bricaud, K. R. Arrigo, and M. Babin. 2015. Characteristics of colored dissolved organic matter (CDOM) in the Western Arctic Ocean: relationships with microbial activities. Deep Sea Research Part II: Topical Studies in Oceanography **118**:44-52.
Matthews, M. W. 2011. A current review of empirical procedures of remote sensing in inland and near-coastal transitional waters. International Journal of Remote Sensing **32**:6855-6899.
McKee, D., R. Röttgers, G. Neukermans, V. S. Calzado, C. Trees, M. Ampolo-Rella, C. Neil, and A. Cunningham. 2014. Impact of measurement uncertainties on determination of chlorophyll-specific absorption coefficient for marine phytoplankton. Journal of Geophysical Research: Oceans **119**:9013-9025.
Menden-Deuer, S., and E. J. Lessard. 2000. Carbon to volume relationships for dinoflagellates, diatoms, and other protist plankton. Limnology and oceanography **45**:569-579.
Mitchell, B. G. 1990. Algorithms for determining the absorption coefficient for aquatic particulates using the quantitative filter technique. Pages 137-148 *in* Ocean optics X. International Society for Optics and Photonics.
Mitchell, B. G., M. Kahru, J. Wieland, and M. Stramska. 2003. Determination of spectral absorption coefficients of particles, dissolved material and phytoplankton for discrete water samples. Ocean Optics Protocols for Satellite Ocean Color Sensor Validation, Revision **4**:39-64.
Moberg, E. A., and H. M. Sosik. 2012. Distance maps to estimate cell volume from two-dimensional plankton images. Limnology and Oceanography: Methods **10**:278-288.
Moline, M. A., H. Claustre, T. K. Frazer, O. Schofield, and M. Vernet. 2004. Alteration of the food web along the Antarctic Peninsula in response to a regional warming trend. Global change biology **10**:1973-1980.
Montes-Hugo, M., S. C. Doney, H. W. Ducklow, W. Fraser, D. Martinson, S. E. Stammerjohn, and O. Schofield. 2009. Recent changes in phytoplankton communities associated with rapid regional climate change along the western Antarctic Peninsula. Science **323**:1470-1473.

Moore, S. E., and J. M. Grebmeier. 2018. The Distributed Biological Observatory: linking physics to biology in the Pacific Arctic region. Arctic **71**:1-7.
Moore, S. E., J. M. Grebmeier, and N. Giguère. 2018. The Distributed Biological Observatory. Arctic **71**:1-7.
Moore, S. E., E. Logerwell, L. Eisner, E. V. Farley, L. A. Harwood, K. Kuletz, J. Lovvorn, J. R. Murphy, and L. T. Quakenbush. 2014. Marine fishes, birds and mammals as sentinels of ecosystem variability and reorganization in the Pacific Arctic region. Pages 337-392 The Pacific arctic region. Springer.
Morel, A., and L. Prieur. 1977. Analysis of variations in ocean color 1. Limnology and oceanography **22**:709-722.
Mueller, J. L. 2003. Ocean Optics Protocols for Satellite Ocean Color Sensor Validation, Revision 4: Introduction, background, and conventions. Goddard Space Flight Center.
Mueller, J. L., and R. W. J. O. L. R. Austin. 1995. Ocean optics protocols for SeaWiFS validation, revision 1. **9**:805.
Muller-Karger, F. E., P. Miloslavich, N. J. Bax, S. Simmons, M. J. Costello, I. Sousa Pinto, G. Canonico, W. Turner, M. Gill, and E. Montes. 2018. Advancing marine biological observations and data requirements of the complementary essential ocean variables (EOVs) and essential biodiversity variables (EBVs) frameworks. Frontiers in Marine Science **5**:211.
Naik, P., and E. J. J. O. e. D'Sa. 2012. Phytoplankton light absorption of cultures and natural samples: comparisons using two spectrophotometers. **20**:4871-4886.
Natsuike, M., K. Matsuno, T. Hirawake, A. Yamaguchi, S. Nishino, and I. J. H. A. Imai. 2017. Possible spreading of toxic Alexandrium tamarense blooms on the Chukchi Sea shelf with the inflow of Pacific summer water due to climatic warming. **61**:80-86.
Neeley, A., L. Harris, and K. Frey. 2018. Unraveling Phytoplankton Community Dynamics in the Northern Chukchi Sea Under Sea-Ice-Covered and Sea-Ice-Free Conditions. Geophysical Research Letters **45**:7663-7671.
Neeley, A., and A. Mannino. 2018. Inherent Optical Property Measurements and Protocols: Absorption Coefficient. IOCCG.
Neeti, N., and J. R. Eastman. 2011. A contextual mann-kendall approach for the assessment of trend significance in image time series. Transactions in GIS **15**:599-611.
Neukermans, G., R. A. Reynolds, and D. Stramski. 2014. Contrasting inherent optical properties and particle characteristics between an under-ice phytoplankton bloom and open water in the Chukchi Sea. Deep Sea Research Part II: Topical Studies in Oceanography **105**:59-73.
Neukermans, G., R. A. Reynolds, and D. Stramski. 2016. Optical classification and characterization of marine particle assemblages within the western Arctic Ocean. Limnology and oceanography **61**:1472-1494.
Nishino, S., Y. Kawaguchi, J. Inoue, T. Hirawake, A. Fujiwara, R. Futsuki, J. Onodera, and M. Aoyama. 2015. Nutrient supply and biological response to wind-induced mixing, inertial motion, internal waves, and currents in the northern Chukchi Sea. Journal of Geophysical Research: Oceans **120**:1975-1992.
Novoa, S., M. Wernand, and H. Van der Woerd. 2014. The modern Forel-Ule scale: a 'do-it-yourself'colour comparator for water monitoring. Journal of the European Optical Society-Rapid publications **9**.

O'Reilly, J. E., S. Maritorena, B. G. Mitchell, D. A. Siegel, K. L. Carder, S. A. Garver, M. Kahru, and C. McClain. 1998. Ocean color chlorophyll algorithms for SeaWiFS. Journal of Geophysical Research: Oceans **103**:24937-24953.

O'Reilly, J. E., S. Maritorena, D. A. Siegel, M. C. O'Brien, D. Toole, B. G. Mitchell, M. Kahru, F. P. Chavez, P. Strutton, and G. F. Cota. 2000. Ocean color chlorophyll a algorithms for SeaWiFS, OC2, and OC4: Version 4. SeaWiFS Postlaunch Calibration Validation Analyses **3**:9-23.

Olson, R. J., and H. M. Sosik. 2007. A submersible imaging-in-flow instrument to analyze nano-and microplankton: Imaging FlowCytobot. Limnology and Oceanography: Methods **5**:195-203.

Overland, J. E., E. Hanna, I. Hanssen-Bauer, S.-J. Kim, J. E. Walsh, M. Wang, U. S. Bhatt, and R. L. Thoman. 2018. Surface Air Temperature. Arctic Report Card 2018.

Overland, J. E., and M. Wang. 2013. When will the summer Arctic be nearly sea ice free? Geophysical Research Letters **40**:2097-2101.

Overpeck, J. T., M. Sturm, J. A. Francis, D. K. Perovich, M. C. Serreze, R. Benner, E. C. Carmack, F. S. Chapin, S. C. Gerlach, and L. C. Hamilton. 2005. Arctic system on trajectory to new, seasonally ice-free state. Eos, Transactions American Geophysical Union **86**:309-313.

Pereira, H. M., S. Ferrier, M. Walters, G. N. Geller, R. Jongman, R. J. Scholes, M. W. Bruford, N. Brummitt, S. Butchart, and A. Cardoso. 2013. Essential biodiversity variables. Science **339**:277-278.

Pisareva, M. N., R. S. Pickart, M. Spall, C. Nobre, D. Torres, G. Moore, and T. E. Whitledge. 2015. Flow of Pacific water in the western Chukchi Sea: Results from the 2009 RUSALCA expedition. Deep Sea Research Part I: Oceanographic Research Papers **105**:53-73.

Preisendorfer, R. W. 1976. Hydrologic Optics. Volume 1. Introduction. Honolulu: US Dept. of Commerce, National Oceanic and Atmospheric ….

Ralston, D. K., W. R. Geyer, and J. A. Lerczak. 2010. Structure, variability, and salt flux in a strongly forced salt wedge estuary. Journal of Geophysical Research: Oceans **115**.

Reynolds, R. A., and D. Stramski. 2019. Optical characterization of marine phytoplankton assemblages within surface waters of the western Arctic Ocean. Limnology and oceanography **64**:2478-2496.

Richter-Menge, J., J. Overland, J. Mathis, and E. Osborne. 2017. Arctic Report Card 2017 https://arctic. noaa. gov/Report-Card.

Rivero-Calle, S., A. Gnanadesikan, C. E. Del Castillo, W. M. Balch, and S. D. Guikema. 2015. Multidecadal increase in North Atlantic coccolithophores and the potential role of rising CO2. Science **350**:1533-1537.

Roesler, C. S. 1998. Theoretical and experimental approaches to improve the accuracy of particulate absorption coefficients derived from the quantitative filter technique. Limnology and oceanography **43**:1649-1660.

Roesler, C. S. 2014.

Röttgers, R., C. Dupouy, B. B. Taylor, A. Bracher, and S. B. Woźniak. 2014. Mass-specific light absorption coefficients of natural aquatic particles in the near-infrared spectral region. Limnology and oceanography **59**:1449-1460.

Röttgers, R., and S. Gehnke. 2012. Measurement of light absorption by aquatic particles: improvement of the quantitative filter technique by use of an integrating sphere approach. Applied Optics **51**:1336-1351.

Röttgers, R., C. Häse, and R. Doerffer. 2007. Determination of the particulate absorption of microalgae using a point-source integrating-cavity absorption meter:

verification with a photometric technique, improvements for pigment bleaching, and correction for chlorophyll fluorescence. Limnology and Oceanography: Methods **5**:1-12.
Röttgers, R., D. McKee, and S. B. J. M. i. O. Woźniak. 2013. Evaluation of scatter corrections for ac-9 absorption measurements in coastal waters. **7**:21-39.
Sathyendranath, S., J. Aiken, S. Alvain, R. Barlow, H. Bouman, A. Bracher, R. Brewin, A. Bricaud, C. Brown, and A. Ciotti. 2014. Phytoplankton functional types from space. Pages 1-156 Reports of the International Ocean-Colour Coordinating Group (IOCCG). International Ocean-Colour Coordinating Group.
Sathyendranath, S., R. J. Brewin, C. Brockmann, V. Brotas, B. Calton, A. Chuprin, P. Cipollini, A. B. Couto, J. Dingle, and R. Doerffer. 2019. An Ocean-Colour Time Series for Use in Climate Studies: The Experience of the Ocean-Colour Climate Change Initiative (OC-CCI). Sensors **19**:4285.
Sathyendranath, S., and T. Platt. 1997. Analytic model of ocean color. Applied Optics **36**:2620-2629.
Selz, V., S. Laney, A. E. Arnsten, K. M. Lewis, K. E. Lowry, H. L. Joy-Warren, M. M. Mills, G. L. van Dijken, and K. R. Arrigo. 2017. Ice algal communities in the Chukchi and Beaufort Seas in spring and early summer: Composition, distribution, and coupling with phytoplankton assemblages: Ice algal-phytoplankton coupling in Chukchi Sea. Limnology and oceanography **63**.
Signorini, S. R., B. A. Franz, and C. R. McClain. 2015. Chlorophyll variability in the oligotrophic gyres: mechanisms, seasonality and trends. Frontiers in Marine Science **2**:1.
Slade, W. H., E. Boss, G. Dall'Olmo, M. R. Langner, J. Loftin, M. J. Behrenfeld, C. Roesler, and T. K. Westberry. 2010. Underway and moored methods for improving accuracy in measurement of spectral particulate absorption and attenuation. Journal of Atmospheric Oceanic Technology **27**:1733-1746.
Smith, C. R., D. J. DeMaster, C. Thomas, P. Sršen, L. Grange, V. Evrard, and F. DeLeo. 2012. Pelagic-benthic coupling, food banks, and climate change on the West Antarctic Peninsula Shelf. Oceanography **25**:188-201.
Smith, N., W. S. Kessler, S. Cravatte, J. Sprintall, S. Wijffels, M. F. Cronin, A. Sutton, Y. L. Serra, B. Dewitte, and P. G. Strutton. 2019. Tropical pacific observing system. Frontiers in Marine Science **6**:31.
Spreen, G., L. Kaleschke, and G. Heygster. 2008. Sea ice remote sensing using AMSR-E 89-GHz channels. Journal of Geophysical Research: Oceans **113**:C02S03.
Steele, M., W. Ermold, and J. Zhang. 2008. Arctic Ocean surface warming trends over the past 100 years. Geophysical Research Letters **35**.
Steiner, N. S., T. Sou, C. Deal, J. M. Jackson, M. Jin, E. Popova, W. Williams, and A. Yool. 2016. The future of the subsurface chlorophyll-a maximum in the Canada Basin—A model intercomparison. Journal of Geophysical Research: Oceans **121**:387-409.
Stramski, D., R. A. Reynolds, S. Kaczmarek, J. Uitz, and G. Zheng. 2015. Correction of pathlength amplification in the filter-pad technique for measurements of particulate absorption coefficient in the visible spectral region. Applied Optics **54**:6763-6782.
Stroeve, J., T. Markus, L. Boisvert, J. Miller, and A. Barrett. 2014. Changes in Arctic melt season and implications for sea ice loss. Geophysical Research Letters **41**:1216-1225.
Sullivan, J. M., M. S. Twardowski, J. R. V. Zaneveld, C. M. Moore, A. H. Barnard, P. L. Donaghay, and B. Rhoades. 2006. Hyperspectral temperature and salt

dependencies of absorption by water and heavy water in the 400-750 nm spectral range. Applied Optics **45**:5294-5309.
Sverdrup, H. 1953. On conditions for the vernal blooming of phytoplankton. J. Cons. Int. Explor. Mer **18**:287-295.
Tassan, S., and G. M. Ferrari. 1995. An alternative approach to absorption measurements of aquatic particles retained on filters. Limnology and oceanography **40**:1358-1368.
Ter Braak, C. J., and P. F. Verdonschot. 1995. Canonical correspondence analysis and related multivariate methods in aquatic ecology. Aquatic sciences **57**:255-289.
Tremblay, G., C. Belzile, M. Gosselin, M. Poulin, S. Roy, and J.-É. Tremblay. 2009. Late summer phytoplankton distribution along a 3500 km transect in Canadian Arctic waters: strong numerical dominance by picoeukaryotes. Aquat Microb Ecol **54**:55-70.
Tremblay, J.-É., K. Simpson, J. Martin, L. Miller, Y. Gratton, D. Barber, and N. M. Price. 2008. Vertical stability and the annual dynamics of nutrients and chlorophyll fluorescence in the coastal, southeast Beaufort Sea. Journal of Geophysical Research: Oceans **113**.
Trenberth, K., P. Jones, P. Ambenje, R. Bojariu, D. Easterling, A. K. Tank, D. Parker, F. Rahimzadeh, J. Renwick, and M. J. C. c. Rusticucci. 2007. Observations: surface and atmospheric climate change. Chapter 3.235-336.
Ule, W. 1892. Die bestimmung der Wasserfarbe in den Seen. Kleinere Mittheilungen. Dr. A. Petermanns Mittheilungen aus Justus Perthes geographischer Anstalt:70-71.
Van Heukelem, L., and C. S. Thomas. 2001. Computer-assisted high-performance liquid chromatography method development with applications to the isolation and analysis of phytoplankton pigments. Journal of Chromatography A **910**:31-49.
Vandermeulen, R., A. Mannino, S. Craig, and P. Werdell. in Review. 150 Shades of Green: Elucidating color shifts in the ocean using continuum spectral classification. Remote Sensing.
Walsh, J. J., C. P. McRoy, T. H. Blackburn, L. K. Coachman, J. J. Goering, K. Henriksen, P. Andersen, J. J. Nihoul, P. Parker, and A. M. Springer. 1989. The role of Bering Strait in the carbon/nitrogen fluxes of polar marine ecosystems. Pages 90-120 *in* Proceedings of the sixth conference of the Comité Arctique International. EJ Brill, Leiden.
Wassmann, P. 2011. Arctic marine ecosystems in an era of rapid climate change. Progress in Oceanography **90**:1-17.
Werdell, P. J., S. Bailey, G. Fargion, C. Pietras, K. Knobelspiesse, G. Feldman, and C. McClain. 2003. Unique data repository facilitates ocean color satellite validation. Eos, Transactions American Geophysical Union **84**:377-387.
Werdell, P. J., and S. W. Bailey. 2005. An improved in-situ bio-optical data set for ocean color algorithm development and satellite data product validation. Remote Sensing of Environment **98**:122-140.
Werdell, P. J., M. J. Behrenfeld, P. S. Bontempi, E. Boss, B. Cairns, G. T. Davis, B. A. Franz, U. B. Gliese, E. T. Gorman, and O. Hasekamp. 2019. The Plankton, Aerosol, Cloud, ocean Ecosystem mission: status, science, advances. Bulletin of the American Meteorological Society **100**:1775-1794.
Werdell, P. J., B. A. Franz, S. W. Bailey, G. C. Feldman, E. Boss, V. E. Brando, M. Dowell, T. Hirata, S. J. Lavender, and Z. Lee. 2013. Generalized ocean color inversion model for retrieving marine inherent optical properties. Applied Optics **52**:2019-2037.
Wernand, M. R., H. J. van der Woerd, and W. W. Gieskes. 2013. Trends in ocean colour and chlorophyll concentration from 1889 to 2000, worldwide. PLOS One **8**.

Werner, I., J. Ikävalko, and H. Schünemann. 2007. Sea-ice algae in Arctic pack ice during late winter. Polar Biology **30**:1493-1504.
Wheeling, K. 2019. Toxic algal blooms are worseing with climate change. Eos, Transactions American Geophysical Union **100**.
Wilson, C., J. Morales, S. Nayak, I. Asanuma, and G. Feldman. 2008. Ocean-colour radiometry and fisheries. Why ocean colour:47-58.
Woodgate, R. A., K. Aagaard, J. H. Swift, K. K. Falkner, and W. M. Smethie Jr. 2005a. Pacific ventilation of the Arctic Ocean's lower halocline by upwelling and diapycnal mixing over the continental margin. Geophysical Research Letters **32**:L18609.
Woodgate, R. A., K. Aagaard, J. H. Swift, K. K. Falkner, and W. M. Smethie. 2005b. Pacific ventilation of the Arctic Ocean's lower halocline by upwelling and diapycnal mixing over the continental margin. Geophysical Research Letters **32**:n/a-n/a.
Yentsch, C. S. 1962. Measurement of Visible Light Absorption by Particulate Matter in the Ocean. Limnology and oceanography **7**:207-217.
Zaneveld, J. R. V., J. C. Kitchen, and C. C. Moore. 1994. Scattering error correction of reflection-tube absorption meters. Pages 44-55 *in* Ocean Optics XII. International Society for Optics and Photonics.